CFD Analysis of Hydrogen-Diesel Dual-Fuel Combustion in Compression-Ignited Engines using High-Pressure Direct Injection

Master Thesis Aerospace Engineering

Francisco Javier Angulo Aparicio

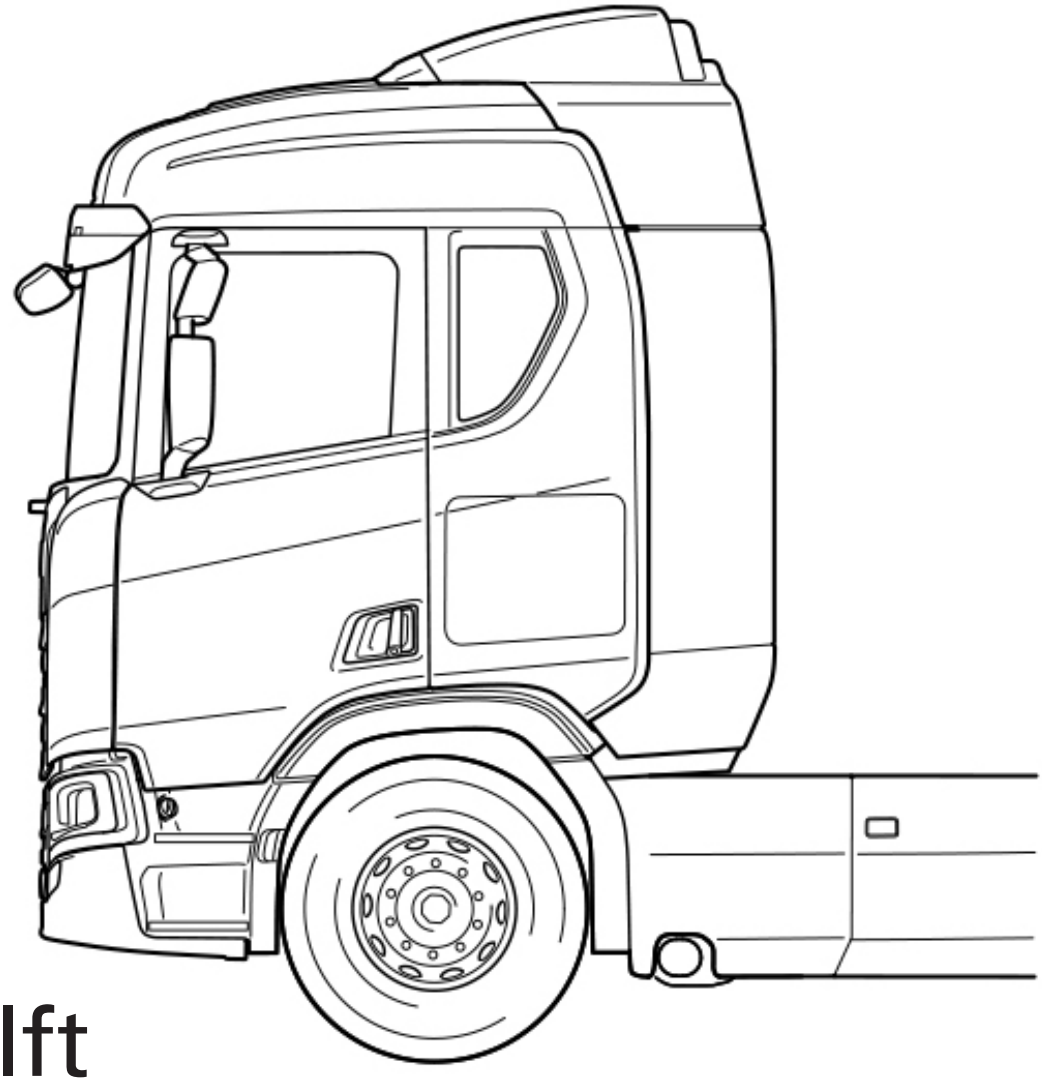

TU Delft

CFD Analysis of Hydrogen-Diesel Dual-Fuel Combustion in Compression-Ignited Engines using High-Pressure Direct Injection

by

Francisco Javier Angulo Aparicio

to obtain the degree of
Master of Science in Aerospace Engineering
at the Delft University of Technology
to be defended publicly on November 26th, 2025 at 10:00

Thesis Committee:

Chair:	Dr. Steven Hulshoff
Supervisor:	Dr. Ivan Langella
Company Supervisor:	Dr. Vivianne Holmén Notander - Scania
Examiner:	Ir. Joris Melkert
Project Duration:	March, 2025 - November, 2025
Faculty:	Faculty of Aerospace Engineering, Delft
Student Number:	6079830

An electronic version of this thesis is available at https://repository.tudelft.nl/.

TU Delft

Abstract

Hydrogen represents a promising pathway for decarbonizing heavy-duty transport; however, accurately modeling its injection and combustion behavior in dual-fuel engines remains challenging. This work addresses two critical aspects of hydrogen high-pressure direct injection (HPDI) systems: the characterization of the injection process and the physical mechanisms governing combustion initiation.

A CFD-based methodology was developed to reconstruct injection profiles from apparent heat release rate (aHRR) data and to apply nozzle flow theory for approximating injector behavior, validated through experimental comparison. The findings indicate that classical convergent-nozzle theory fails to capture the observed injection trends. While convergent nozzle theory predicts variable, pressure-dependent mass flow rates, the reconstructed mass flow profiles exhibit nearly constant injection rates when the needle is open, consistent with convergent–divergent nozzle theory predictions. However, the observed variation in maximum injection rates across different cases suggests these deviations may arise not only from geometric constraints but also from aerodynamic phenomena such as boundary layer separation or recirculation within the injector. Such flow features can induce pressure-dependent effects that limit injector performance beyond what nozzle geometry and convergent-nozzle theory alone would predict.

Regarding combustion, the study reveals that hydrogen ignition, triggered by a small diesel pilot, is dominated by localized high-temperature regions produced by the diesel flame. This accelerated autoignition contrasts with alternative hypotheses involving radical transport or direct flame interaction.

Overall, these results advance the understanding of injection and ignition phenomena in hydrogen HPDI engines, providing valuable insights for refining CFD models and supporting the development of efficient hydrogen-powered heavy-duty engines.

Keywords: Hydrogen combustion, Dual-fuel engines, High-pressure direct injection (HPDI), Diesel pilot, Injection modeling, CFD, Convergent nozzle theory, Convergent–divergent nozzle theory, STAR-CCM+, Heavy-duty transport

Acknowledgements

First and foremost, I would like to express my sincere gratitude to Scania, now TRATON, for giving me the opportunity to carry out this thesis. I am deeply thankful for the trust placed in me, for the chance to come to Stockholm, and for the invaluable support that made this experience possible. In particular, I would like to thank the ENMGD department, now TGRMSTE, with whom I have had the privilege to work over the past eight months. They are outstanding professionals, and I truly appreciate their constant help and guidance. I am also grateful to the colleagues from other departments companies and institutions who contributed in different ways to this work.

Within the department, my special thanks go to Vivianne Holmén Notander for supervising my work, and to Ahmad Hadadpour and Darius Gohari for their constructive feedback and encouragement. Although she is no longer part of the department, I would also like to thank Micaela Labrador, whose friendship has made this experience even more meaningful, and who greatly helped me to integrate both into Scania and into life in Stockholm. The relationships I have built with everyone in this department are something I will always treasure, beyond the professional side of this thesis.

Secondly, I would like to thank TU Delft, and especially Ivan Langella, for agreeing to supervise me despite the challenges of conducting a company-based thesis with a student who had not previously been part of his courses. I am also grateful to TU Delft for enabling me to live such valuable international and industrial experiences during this master's programme.

I would also like to express my heartfelt thanks to my family and friends. To my parents, for giving me the opportunity to pursue this master's degree abroad and for supporting me throughout my studies and life in different countries. To my friends from Delft, for making that first, demanding year in the Netherlands so much better, especially to Pablo Álvarez with whom I share incredible memories living in the same flat. And to my friends in Stockholm for welcoming me when I had just arrived to start my thesis.

Finally, I would like to make a special mention of my grandfather Pedro, who sadly passed away in September. He was the person who first introduced me to the world of automotive engineering when I was a child. He was the first person to ever show me an article about hydrogen engines. During the early stages of this thesis, we had many interesting conversations on the topic. I will miss him deeply, but his influence on my life, and therefore on my presence here today, will always stay with me.

Contents

List of Figures

List of Tables

List of Abbreviations

Abbreviation	Definition
AHRR	Apparent Heat Release Rate
ATDC	After Top Dead Center
BTDC	Before Top Dead Center
CAD	Crank Angle Degree
CC	Complex Chemistry
CD	Convergent–Divergent (Nozzle)
CFD	Computational Fluid Dynamics
CFM	Computational Fluid Mechanics
CHRR	Chemical Heat Release Rate
CI	Compression-Ignited / Compression Ignition
CFL	Courant–Friedrichs–Lewy
Cp	Specific Heat at Constant Pressure
Cv	Specific Heat at Constant Volume
DNS	Direct Numerical Simulation
DOF	Degree of Freedom
EGR	Exhaust Gas Recirculation
EU	European Union
EV	Electric Vehicle
GHG	Greenhouse Gas
HPDI	High-Pressure Direct Injection
ICE	Internal Combustion Engine
ICEV	Internal Combustion Engine Vehicle
IDT	Ignition Delay Time
IVC	Intake Valve Closing
LCA	Life Cycle Assessment
LFC	Laminar Flame Concept
LES	Large Eddy Simulation
LHV	Lower Heating Value
NOx	Nitrogen Oxides
OH	Hydroxyl Radical
PAH	Polycyclic Aromatic Hydrocarbons
PFI	Port Fuel Injection
PM	Particulate Matter
PM2.5	Particulate Matter with Diameter $\leq$ 2.5 µm
PM10	Particulate Matter with Diameter $\leq$ 10 µm
PDF	Probability Density Function
PIV	Particle Image Velocimetry
RANS	Reynolds-Averaged Navier–Stokes
RH	Relative Humidity
RNG	Renormalization Group (k–ϵ turbulence model)
ROI	Region of Interest
Sct	Turbulent Schmidt Number

Abbreviation	Definition
SI	Spark-Ignited / Spark Ignition
SOI	Start of Injection
STAR-CCM+	Simcenter STAR-CCM+ (Siemens CFD Software)
TFSC / TFC	Turbulent Flame Speed Closure
TDC	Top Dead Center
TKE	Turbulent Kinetic Energy
UHC	Unburned Hydrocarbons
WHO	World Health Organization

Chapter 1

Introduction and Literature Review

1.1 Motivation and project context

In 2022, Scania initiated a collaborative project with Lund University, known as HyZERO, focused on the development of a hydrogen internal combustion engine (H2 ICE) for heavy-duty applications [23].

This thesis builds upon the work of previous Master's students, including Hao Liu [41] and Diego Antonacci [12], as well as PhD researcher Mark Treacy [93]. It is also connected to ongoing collaboration with current PhD student Federico Moratto, under the supervision of Professor Hesameddin Fatehi. These previous CFD studies on hydrogen internal combustion engines at Scania were conducted using the CONVERGE CFD platform. However, since Scania recently transitioned to using Simcenter STAR-CCM+ as its primary tool for in-cylinder simulations this thesis will be based entirely on simulations performed in STAR-CCM+.

This introduction begins by explaining the motivations behind the development of hydrogen internal combustion engines, with a focus in particular on heavy-duty applications. It then examines the current state of research across a range of relevant topics. Ultimately, the goal is to, first, identify gaps in the existing literature that this work can help address, and second, to consolidate best practices and methodologies that can be applied to the simulation strategy adopted in this thesis.

The structure follows a logical progression from contextual background to modeling strategies. It covers: (2) health and environmental impacts of energy-related emissions, (3) challenges of electrification in the transport sector, (4) hydrogen as a fuel for internal combustion engines, (5) a comparison between spark-ignited and compression-ignited hydrogen engines, (6) key differences between hydrogen and diesel in CI applications, (7) governing equations for reacting flows, (8) turbulence modeling, (9) turbulent combustion modeling in STAR-CCM+ and (10) chemical reaction mechanisms.

1.2 Health and Environmental Impacts of Energy-Related Emissions

Figure 1.1 displays the world distribution of energy consumption by source since 1965. The graph shows that around 80% of the global energy mix is composed of oil, coal, and gas, which are, in essence, fossil fuels. Despite increased attention to renewable energy and the growing urgency of climate change, fossil fuels remain the dominant source of global energy. Their combustion is a well-known and effective mean of producing energy, largely due to their availability and affordability; however, it also results in the emission of a wide range of pollutants that have significant consequences for both the environment and human health.

The most widely known pollutant is carbon dioxide (CO_2), a greenhouse gas that contributes to global climate change. Climate change has a direct and indirect negative impact on the environment, biodiversity, and human health in the long term [29, 49, 52]. Figure 1.2 displays the annual temperature anomalies with respect to levels found before the industrial revolution. This is one of the most concerning consequences of climate change, since the increase in GHG emissions has been a constant since the beginning of the industrial revolution. Other emissions, however, have more immediate and localized health effects. For instance, Nitrogen oxides (NO_x) contribute to ground-level ozone and acid rain, and are associated with respiratory illnesses and premature mortality [10, 82]. Another example is Carbon monoxide (CO) which is produced by incomplete combustion of fossil fuels. CO reduces the body's capacity to transport oxygen and can be fatal at high concentrations [66]. Unburned hydrocarbons (UHC) are another example, these are related to the formation of smog and can produce eye irritation, asthma, and other chronic respiratory conditions [31]. Among the most harmful pollutants is particulate matter (PM), especially $PM_{2.5}$. These fine particles penetrate deeply into the lungs and bloodstream, increasing the risk of cardiovascular and pulmonary diseases, strokes, and cancer [10, 14].

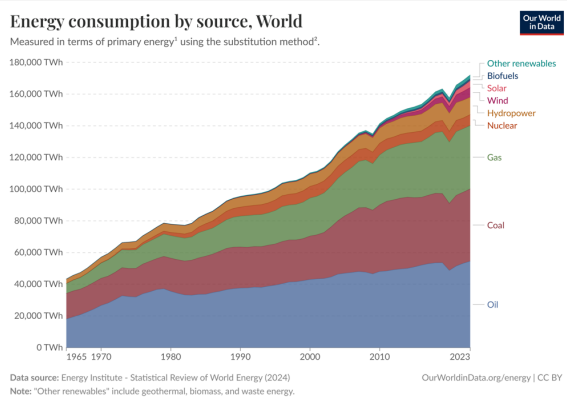

Figure 1.1: World energy consumption by source. [71]

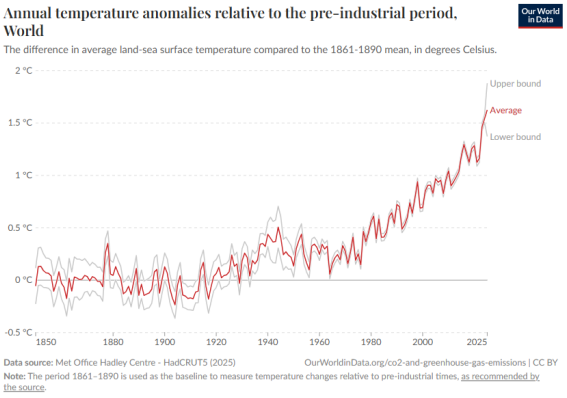

Figure 1.2: Annual temperature anomalies. [74]

The impact of air pollution on health has been studied in several epidemiological studies. These studies have shown significant associations between exposure to common air pollutants and increased hospital admissions, respiratory and cardiovascular diseases, and premature mortality, even at relatively low concentrations [14]. According to the Lancet Commission on Pollution and Health, pollution was responsible for approximately 9 million premature deaths in 2019, one in six deaths globally, out of which 6.7 million could have been related to ambient and household air pollution alone [25]. More than 90% of these deaths occur in low- and middle-income countries, where pollution control measures are often insufficient. The World Health Organization (WHO) highlights that pollutants such as $PM_{2.5}$, PM_{10}, NO_2, SO_2, CO, and ozone can have harmful effects even at low exposure levels, and more importantly, that no safe thresholds have been identified for several of them [98]. To mitigate their impact, WHO issued revised Global Air Quality Guidelines in 2021, lowering the annual $PM_{2.5}$ limit to 5 $\mu g/m^3$, a concentration that is currently exceeded in the vast majority of urban environments worldwide [97].

1.2.1 The Role of Energy and Emissions in Global Economic Growth

As it was previously mentioned there seems to be a close relationship between economic development and polluting emissions. The correlation between economic growth and energy consumption has been widely discussed in literature. Historically, since the beginning of the industrial revolution, GDP growth was closely coupled with increases in energy demand and, consequently, greenhouse gas emissions. This correlation can be attributed to the fact that economic activity, especially that related to the secondary sector, is heavily reliant on energy-intensive sectors such as industry, mining, and manufacturing.

Toward the end of the 20th century, however, many advanced economies began transitioning toward service-oriented structures, and increased their imports of manufacturing and industrial products. This shift allowed these economies to grow without a proportional increase in energy consumption, marking the beginning of a partial decoupling between GDP and energy use. However, despite this positive decoupling, Figure 1.3 shows that GDP per capita and energy use per capita remain strongly correlated.

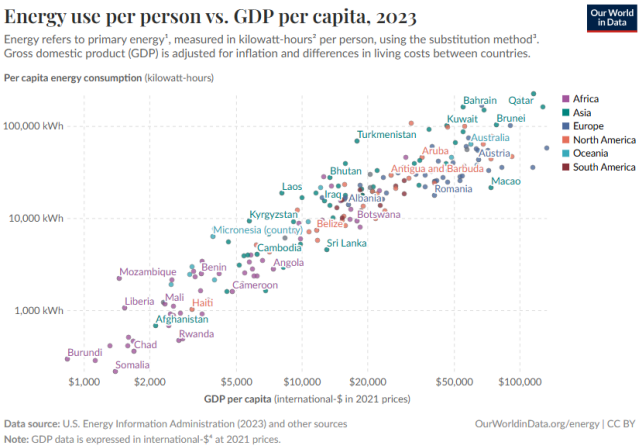

Figure 1.3: Energy use per capita vs. GDP per capita across countries. [70]

Despite the decoupling trend in some countries, Figure 1.3 makes it clear that higher economic prosperity is still associated with higher energy consumption. Therefore, even if economic growth becomes less energy-intensive, it does not imply a decline in total energy demand. Far from decreasing, if global living standards rise, as is both desirable and expected, it seems reasonable to expect that energy consumption will continue to rise. In this context, the development of alternative and affordable low-emission energy sources is essential to ensure that economic growth can continue without worsening climate change.

This relationship between economic growth and emissions can be further illustrated by looking at the trajectories of four key economies: the European Union, the United States, China, and India. These cases highlight the diversity of energy-emissions trajectories and offer insight into the possibilities and challenges of sustainable growth:

- **European Union:** Since 1990, the European Union has achieved moderate economic growth while significantly reducing CO_2 emissions. This decoupling is the result of a deliberate shift toward cleaner energy sources, improved energy efficiency, and strong environmental policies. As shown in Figure 1.4, GDP has continued to rise steadily while emissions have declined markedly. This trend is particularly pronounced in countries like Sweden, where GDP has increased by approximately 60% while emissions have fallen by about 50%. [69] At the EU level, however, fossil fuels still account for more than 50% of the total energy mix, as illustrated in Figure 1.5. This relatively high share is due to the energy profiles of countries such as Germany, which has relied heavily on natural gas following its nuclear phase-out [15], or Poland, where coal remains a dominant energy source. [71]

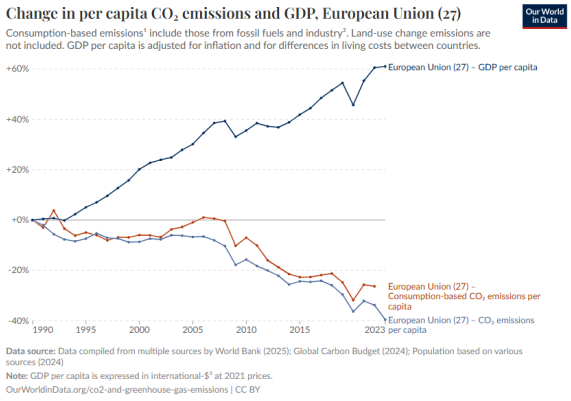

Figure 1.4: CO_2 emissions and GDP in the EU over time. [69]

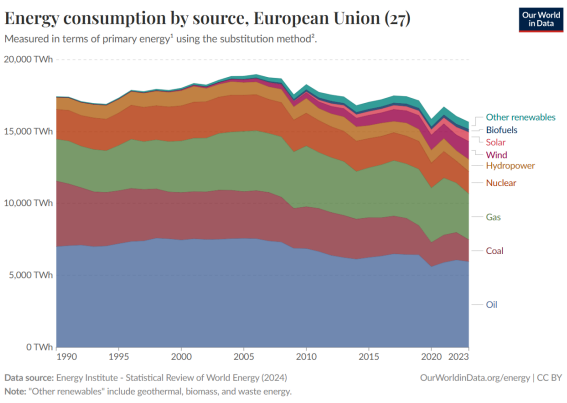

Figure 1.5: Energy consumption in the EU by source.[71]

- **United States:** As another major developed economy, the United States has also achieved economic growth alongside a reduction in CO_2 emissions per capita. The U.S. has experienced higher GDP growth, but only a lower decrease in emissions compared to the EU, as illustrated in Figure 1.6. This limited decoupling reflects a slower rate of transition in the energy mix associated with a comparatively weaker regulatory frameworks. The decline in emissions has been largely driven by the replacement of coal with natural gas, as shown in Figure 1.7, rather than by the implementation of renewable energies, which are still quite recent. Natural gas, while less polluting than coal, remains a fossil fuel and continues to contribute to greenhouse gas emissions.

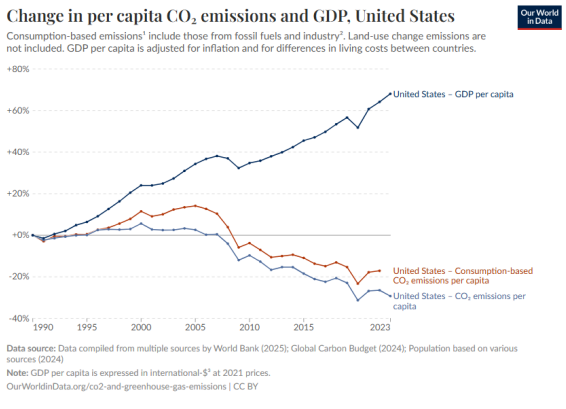

Figure 1.6: CO_2 emissions and GDP in the USA over time. [69]

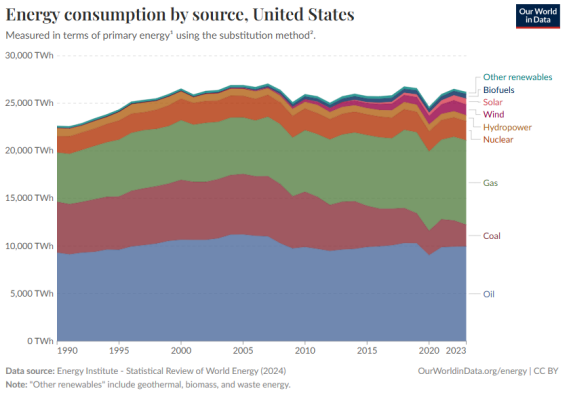

Figure 1.7: Energy consumption in the USA by source. [71]

- **China:** As shown in Figure 1.8, the country has experienced an extraordinary rate of economic growth since 1990, with its GDP increasing by over 1200%. During the same period, CO_2 emissions rose by approximately 300%, indicating a limited degree of relative decoupling. The Chinese economic growth and emissions have both followed an ascendant trajectory, driven largely by rapid industrialization and a coal-dominated energy system. As a result, China has become the world's largest emitter of CO_2 [73]. Despite recent efforts to expand renewable energy and improve energy efficiency, coal remains the primary energy source in the country, as illustrated in Figure 1.9, posing ongoing challenges to climate mitigation efforts.

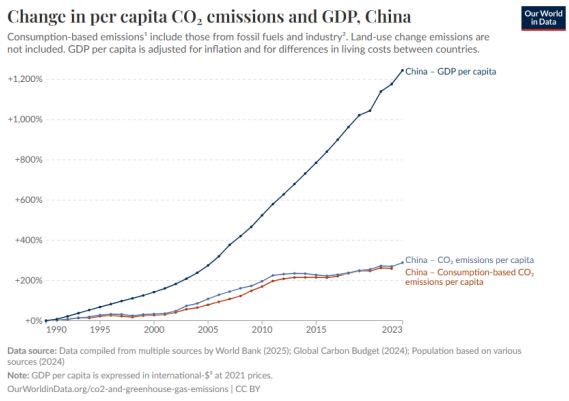

Figure 1.8: CO_2 emissions and GDP in China over time. [69]

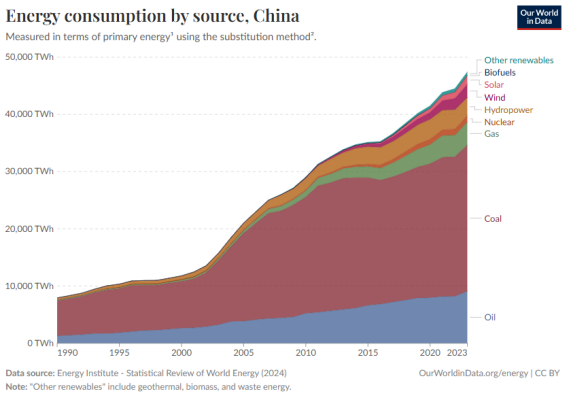

Figure 1.9: Energy consumption in China by source. [71]

- **India:** As the most populous country in the world, India plays a critical role in the global emissions landscape. Since 1990, its GDP has grown by approximately 300%, while CO_2 emissions have increased by around 200%, reflecting a strong correlation between economic development and emissions. As shown in Figure 1.10, both indicators have followed a closely aligned upward trend. This pattern is largely explained by India's continued reliance on the secondary sector and its heavy dependence on coal for power generation and industrial processes. As illustrated in

Figure 1.11, coal remains the backbone of the country's energy mix. Given India's demographic scale, the way it manages its energy transition will have major implications for global climate goals.

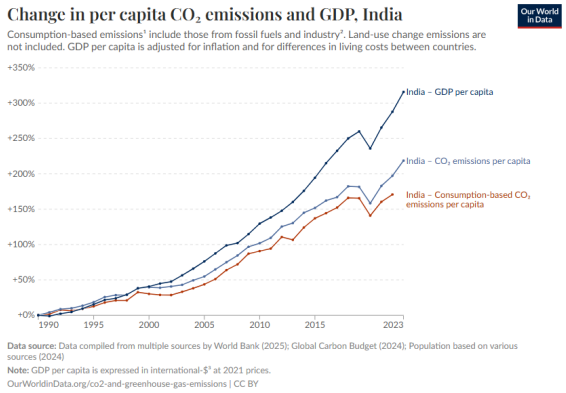

Figure 1.10: CO_2 emissions and GDP in India over time. [69]

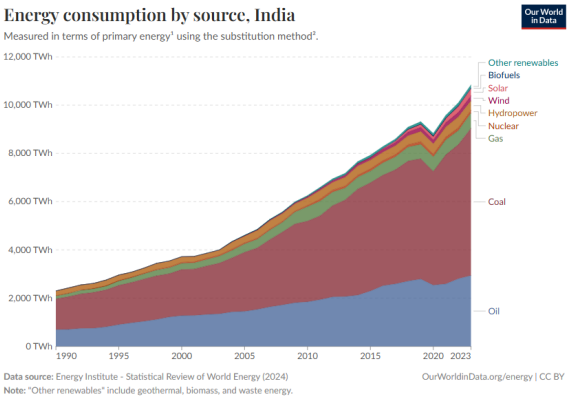

Figure 1.11: Energy consumption in India by source. [71]

In summary, while countries follow different energy and emissions trajectories based on their development stage and policy choices, a common challenge emerges: ensuring access to affordable, low-carbon energy. This is especially relevant for emerging economies, where improving living standards remains a top priority and where cheap fossil fuels still dominate the energy mix. The global success of the energy transition will depend not only on technological advances, but also on making clean energy economically viable across diverse regional contexts.

1.2.2 Where Emissions Come From: Sectoral Differences

Understanding how emissions are distributed across sectors is key to designing effective mitigation strategies. Although electricity generation is a major source of greenhouse gas (GHG) emissions globally (see Figure 1.12), national profiles differ substantially depending on the structure of each economy, energy use patterns, and stage of development.

As shown in Figure 1.13, in the European Union and the United States, the electricity and heat sector has historically been the largest contributor to emissions. However, these emissions have declined in recent decades due to increased energy efficiency, the reduced impact in these economies of the activity of the second economic sector and the integration of renewable energies. [89] In both regions, the transport sector has remained a major emitter and, if current trends continue, it is expected to surpass electricity as the main source of emissions. This shift has led to a strong political and industrial focus on transport decarbonization, particularly in Europe, where automakers and logistics companies are under increasing pressure to reduce their carbon footprint. Regulatory frameworks such as the Euro emission standards have played a key role in this transformation. These standards, currently up to Euro 6 for heavy-duty vehicles and moving toward Euro 7 for all vehicle categories, progressively limit the allowable emissions of pollutants. [54] In the United States, similar efforts are enforced through the Environmental Protection Agency's (EPA) Tier 3 regulations, which establish limits for light- and heavy-duty vehicles [95]. India, meanwhile, follows Bharat Stage VI (BS-VI) standards, largely aligned with Euro 6 norms. While both regions impose strict requirements, European standards are often considered more aggressive, particularly in terms of NO_x and PM thresholds.

In contrast, in Figure 1.14 the emissions in both China and India are displayed. In these countries transport emissions are relatively smaller in percentage terms and currently rank only as the fourth largest source. However, this does not mean they are negligible. In the case of China, for example, absolute emissions from the transport sector are already comparable to those in the EU or the US. The reason they appear less dominant is due to the overwhelming contribution of electricity and heat generation, which overshadows other sectors. Manufacturing and construction also play a major role, particularly

in China. These patterns reflect the structure of their economies, where expanding electricity access and large-scale infrastructure development continue to drive emissions.

A key reason for the dominance of emissions from the energy sector in China and India is their continued reliance on coal, as seen in the previous section. Despite its high carbon intensity, coal remains the most affordable and readily available energy source in both countries. As a consequence, the average cost of electricity in China and India is approximately $0.08/kWh, considerably lower than in the United States ($0.18/kWh), or the European Union (around $0.28/kWh on average) where it varies between countries, for example in Sweden $0.22/kWh or $0.36/kWh in Germany. [68] Reducing the carbon intensity of power generation in coal-dependent systems remains one of the most critical challenges of the global energy transition. While the decarbonization of electricity is essential to align with climate goals, especially in growing economies with high levels of population like China and India, this transition is far from straightforward. Coal continues to provide a reliable and inexpensive energy supply which has played a key role in supporting industrial growth and expanding energy access. Shifting away from such a cheap energy source could increase electricity prices and constrain economic development. As a result, many countries are hesitant to commit fully to phasing out coal without viable and affordable alternatives.

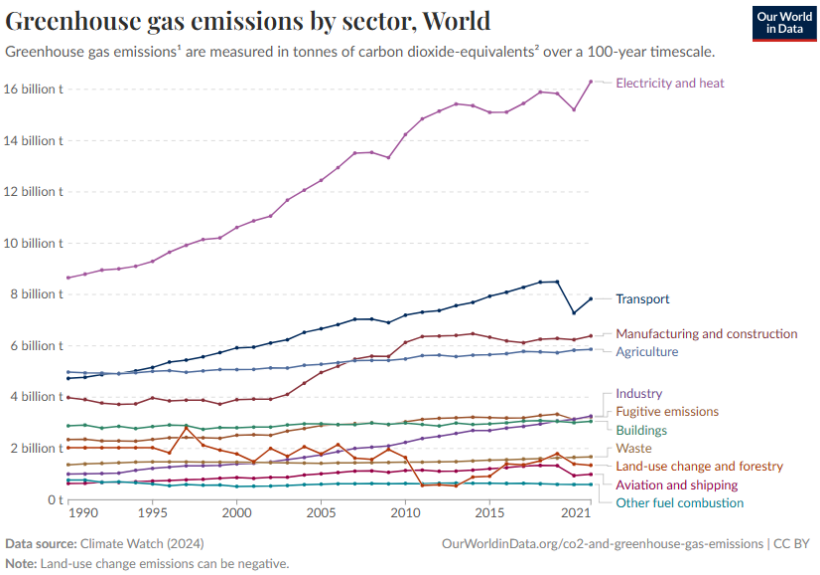

Figure 1.12: World GHG emissions by sector from 1990 to 2021. [72]

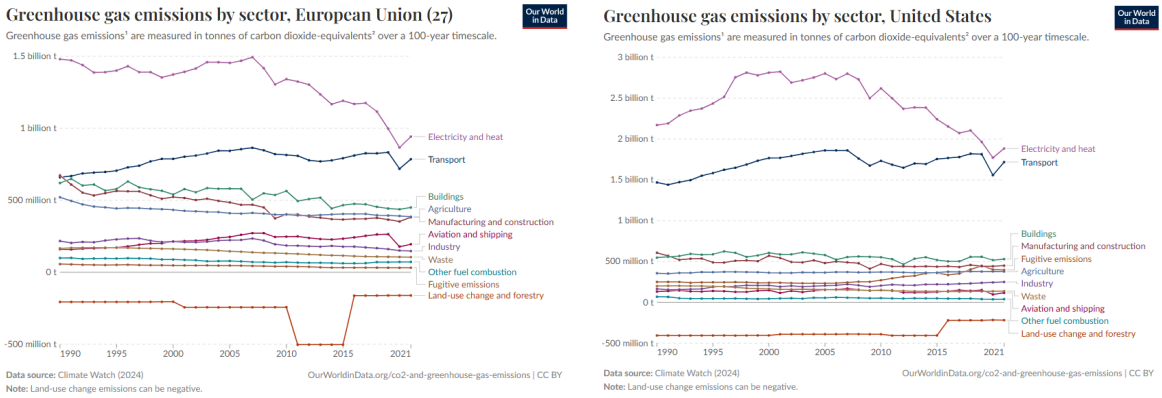

(a) EU **(b)** USA

Figure 1.13: GHG emissions by sector from 1990 to 2021 in the EU and USA. [72]

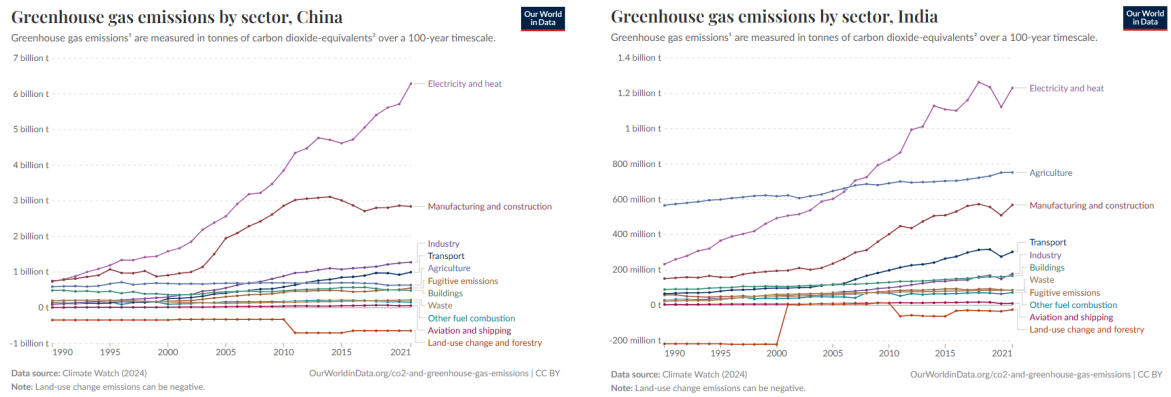

(a) China **(b)** India

Figure 1.14: GHG emissions by sector from 1990 to 2021 in China and India. [72]

1.3 Challenges of Electrification in the Transport Sector

While electrification is a promising path to reduce tailpipe emissions in transport, its global sustainability is deeply entangled with the electricity mix. As seen in Figure 1.15, in 2023 the global electricity production was still largely dependent on fossil fuels: coal (35.51%), gas (22.47%), and oil (2.67%). Clean energy sources such as wind (7.82%), solar (5.53%), and hydropower (14.28%) remain insufficient to meet a potential surge in electricity demand if the entire vehicle fleet were to be electrified. Although regions like the EU are progressively greening their energy systems, major current and future emitters such as China and India are far from decarbonizing at the same pace.

As of 2023, the global electric vehicle (EV) stock still accounts for only a small fraction of the total vehicle fleet, with estimates placing EVs sells at around 18% of all cars sold last year.[75] This raises a critical question: *if all vehicles were electrified, how much additional electricity would be needed? Could it be supplied sustainably?*

Beyond infrastructure and energy availability, the full environmental impact of electric vehicles must be assessed through a Life Cycle Assessment (LCA). Figure 1.16 presents the LCA results of the Polestar 2 (2020), compared with its ICE counterpart, the Volvo XC40. Over a 200,000 km lifespan, the XC40 emits 58 tons of CO_2, while the Polestar 2 ranges from 50 tons (global electricity mix), 42 tons (EU mix), to 27 tons (100% wind power). The break-even point, the distance at which the EV's total emissions become lower than the ICEV, varies significantly depending on the energy source: from as little as 50,000 km (100% renewable) to over 112,000 km with the global average mix. In carbon-intensive countries, this point can exceed 200,000 km.

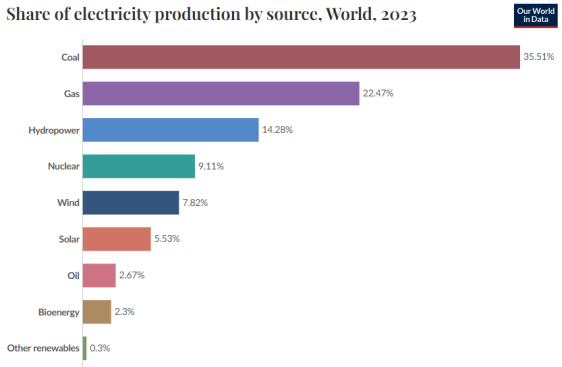

Figure 1.15: Global share of electricity production by source in 2023. [71]

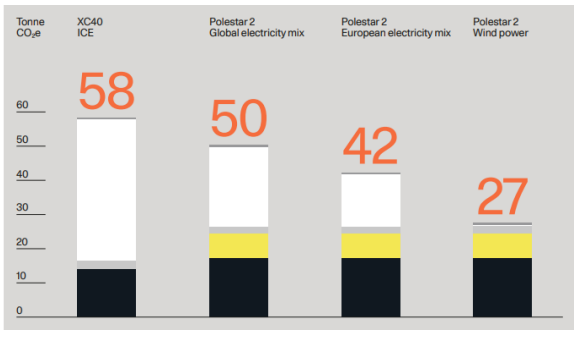

Figure 1.16: Life Cycle Analysis of the Polestar 2 compared to a Volvo XC40 for an expected life of 200,000km. [4]

Other models show similar trends. The BMW i4 M50, compared to the 420i over 200,000 km, achieves a 64% emissions reduction with renewables and 32% with the EU mix. [5] Volkswagen's ID.4 has a break-even point of 66,000 km with green electricity and 97,000 km with the EU mix (versus 78,000 km for the Polestar 2). [7]

However, passenger cars represent only part of the equation. For heavy-duty vehicles, the situation becomes more complex. Figure 1.17 shows the LCA for a Scania battery-electric truck (BEV) with a 300 kWh Northvolt battery, compared to a Euro 6 diesel truck. Over 500,000 km, the diesel truck emits 27.5 tons in production, 2.4 tons in maintenance, 2.1 tons at end-of-life, and a combined 399.2 tons during operation (well-to-tank and tank-to-wheel). The BEV, in contrast, emits 53.6 tons in production and 209.5 tons during operation using the EU 2016 mix, which reduces to 100.2 tons with the EU 2030 forecast and only 4.7 tons with 100% wind. This places the break-even distance between 33,000 km (renewables) and 68,000 km (EU 2016 baseline), still lower than for ICEVs but highly dependent on electricity decarbonization.

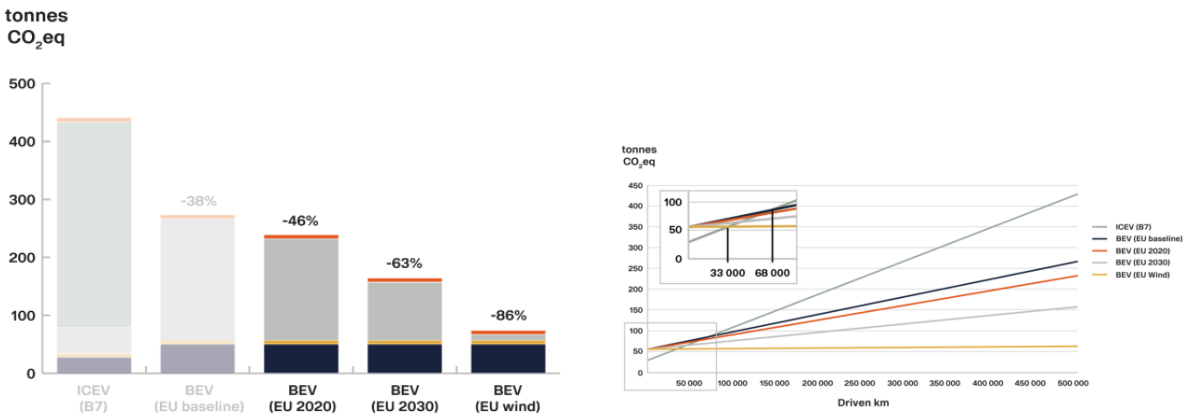

(a) Emissions comparison for an expected life of 500.000km.

(b) Emissions comparison as a function of the distance driven.

Figure 1.17: Life Cycle Analysis made by Scania comparing a BEV (Northvolt batteries) with the equivalent 6 cilinder ICEV. [3]

Despite the potential, limitations remain. The study assumes an average payload of 6.1 tons and a 300KWh battery which are significantly lower than typical heavy-duty applications. According to Scania's catalogue the 728 kWh version achieves a maximum of 375 km at 64 tons GTW and up to 600 km at 29 tons [2]. Recharging such a truck (using CCS2 charger at 375 kW) takes 110 minutes for a full charge, providing about 200 km in the 45-minute mandatory truck driver rest period [1]. Even though a Megawatt Charging System (MCS) is currently being developed to provide 80% charge in under 30 minutes, at the moment, recharging constitutes the main operational limitation on current electric trucks.

In addition, lithium-ion batteries, which power the vast majority of EVs, rely heavily on critical minerals such as lithium, cobalt, nickel, and graphite. The extraction and refining of these materials often carry significant environmental and social burdens. For instance, approximately 40% of the carbon footprint of a lithium-ion battery originates from the mining, conversion, and refining of active materials such as nickel, cobalt, and lithium. Lithium extraction in South America, particularly in the Lithium Triangle region spanning Argentina, Bolivia, and Chile, relies heavily on water-intensive brine extraction methods. This process consumes up to 65% of the limited water resources of the region. [34] Cobalt mining in the Democratic Republic of the Congo (DRC), which has the majority of cobalt in the world, is associated with both hazardous environmental by-products, such as sulfuric acid that contaminates water sources, and serious human rights concerns. [67, 100]

These impacts raise concerns about the scalability and sustainability of battery production. As global EV demand grows, the need for effective battery recycling becomes more pressing, not only to reduce dependency on primary extraction but also to mitigate environmental damage. However, recycling technologies remain under development, and closed-loop systems are still far from being the norm in the automotive industry. [42]

Battery life is another factor that potential clients consider when buying a new vehicle. Performance degradation over time reduces vehicle range and usability. Recognizing this, the Euro 7 regulation introduces durability requirements for EV batteries. Manufacturers must ensure that battery capacity does not fall below 80% of its original value after 5 years or 100,000 km, and not below 72% after 8 years or 160,000 km, effectively setting minimum performance standards across the European market. [53]

In conclusion, while battery-electric vehicles offer clear benefits in reducing tailpipe emissions and can achieve substantial CO_2 reductions when powered by clean electricity, the success of this technology still faces several challenges that are currently being addressed. Their long-term sustainability is constrained by several factors: the environmental and social impacts of critical mineral extraction, the carbon intensity of battery manufacturing, the limited recyclability of components, performance degradation over time, and the ongoing reliance on fossil fuels in the global electricity mix. Moreover, in a future scenario where fully renewable or synthetic fuels become widely available and cost-competitive, the larger carbon footprint associated with the production of heavy batteries may render electric vehicles less favorable compared to alternative propulsion systems. This is particularly relevant in segments such as heavy-duty transport, where operational limitations and high payload requirements challenge current battery technology. In light of these considerations, the exploration of complementary technologies to reduce GHG emissions becomes essential. This thesis is framed within the investigation of one such alternative: the hydrogen internal combustion engine (hydrogen ICE), a promising solution that combines familiar combustion technology with the potential for zero carbon emissions when supplied with green hydrogen.

1.4 Hydrogen as Fuel for Internal Combustion Engines

Hydrogen has been considered a promising alternative fuel for internal combustion engines (ICEs) for a long time, as it produces no carbon emissions when combusted. Despite contemporary discussions concerning hydrogen as a fuel source tend to focus on fuel cell applications, its use in ICEs has a much longer history, dating back to the early 19^{th} century. [101] Although hydrogen ICEs are not yet common in commercial applications, several prototypes have been developed over the years by major automotive manufacturers. For example, BMW has explored hydrogen-fueled combustion engines through multiple concept vehicles. Their last model, powered by a hydrogen ICE, was a modified version of the 7 Series introduced in 2007, featuring a dual-fuel V12 engine capable of running on both gasoline and liquid hydrogen.[6] More recently, Toyota has advanced the concept with high-performance prototypes such as the hydrogen-powered Corolla Sport used in endurance racing or the GR Yaris prototype. [21]

Although hydrogen is abundant in nature, it is not obtained easily, and most of it is produced from other compounds [43]. The method of production has a major influence on the environmental sustainability of hydrogen as a fuel. Depending on the feedstock and process used, hydrogen is commonly classified by color codes that reflect its associated carbon footprint [26].

The most prevalent form today is *grey hydrogen*, produced through steam methane reforming (SMR) or coal gasification, both of which rely on fossil fuels and emit significant amounts of CO_2. These processes are mature and relatively low-cost, but they are also associated with high lifecycle greenhouse gas emissions. *Blue hydrogen* refers to the same fossil-based processes when combined with carbon capture and storage (CCS) technologies, which can significantly reduce emissions. However, CCS remains expensive, energy-intensive, and still does not eliminate all emissions.

In contrast, *green hydrogen* is produced via electrolysis powered by renewable electricity sources such as wind or solar. Although this method is currently more expensive and less mature at industrial scale, it represents the most promising route toward climate-neutral hydrogen production. Worldwide, a growing number of projects are aiming to combine hydrogen production with surplus renewable electricity, especially solar, during peak generation periods, effectively enabling energy storage and grid stabilization. This trend is also driven by the increasing interest in replacing natural gas turbines used for electricity generation with hydrogen-compatible alternatives, further reinforcing the role of green hydrogen in decarbonizing the power sector. Another alternative that has recently drawn attention is *white hydrogen*, a naturally occurring form of hydrogen found in subsurface geological formations. Although

still in early stages of exploration and not yet commercially exploited, it offers the potential for a low-emission source if viable extraction methods are developed. Other classifications include *turquoise hydrogen*, which is generated through methane pyrolysis and yields solid carbon as a byproduct, and *pink hydrogen*, which refers to hydrogen produced via electrolysis using electricity from nuclear power. These emerging alternatives could contribute to a more sustainable hydrogen supply in the transport sector and beyond. However, they remain at different levels of technological maturity and their future role will depend on further innovation, infrastructure development, and political support [8].

Furthermore, although hydrogen combustion does not generate carbon dioxide (CO_2), carbon monoxide (CO), unburned hydrocarbons (HC), or particulate matter (PM) under ideal conditions, the high flame temperature does result in the formation of nitrogen oxides (NO_x). In the absence of appropriate combustion control, NO_x emissions from hydrogen ICEs can reach levels comparable to those of conventional diesel engines and must therefore be addressed through effective aftertreatment methods. Nonetheless, the absence of CO_2 emissions at the tailpipe represents a significant advantage in terms of climate impact.

In addition to the method of production, hydrogen's physical properties present challenges for transport and storage. Due to its low volumetric energy density, it must be compressed to high pressures (typically 350–700 bar) or liquefied at cryogenic temperatures to store sufficient quantities for vehicle use. [112]

Concerning the properties as a fuel, hydrogen is quite a unique element. Hydrogen is the first element of the periodic table, this means that it possesses a unique set of physical and chemical properties that distinguish it from conventional hydrocarbon fuels. It is the lightest element, with a molecular weight of just 2 g/mol, resulting in a low volumetric energy density, which is a disadvantage in terms of storage. However, its gravimetric energy density is the highest of any known fuel with approximately 120 MJ/kg. This is more than twice that of gasoline which is approximately of 44 MJ/kg. This high energy content per unit mass makes it attractive for applications where weight is critical. [78]

Another notable property of hydrogen is its exceptionally wide flammability range, between 4% and 75% by volume in air, which allows for stable operation under very lean conditions. Additionally, hydrogen has an extremely low ignition energy, approximately 0.02 mJ, making it highly susceptible to ignition once a flammable mixture is present. At the same time, it possesses a relatively high autoignition temperature of about 850 K, significantly higher than that of diesel fuel (530 K). Its laminar flame speed is also notably high when compared to hydrocarbon fuels. [37] These characteristics offer several performance benefits, however, they also introduce technical challenges which will be discussed in the next section.

1.5 Spark-Ignited (SI) vs. Compression-Ignited (CI) Hydrogen Engines

Internal combustion engines can be classified into two main categories based on their ignition method: spark-ignited (SI) engines and compression-ignited (CI) engines. In SI engines, typically fueled by gasoline, the air-fuel mixture is ignited using an external spark from a spark plug. Currently SI engines often employ port fuel injection (PFI), where the fuel is injected in the manifold before the air-fuel mix is introduced in the cylinder; or direct injection (DI), where the fuel is injected directly in the combustion chamber, which enables better control over mixture formation and can promote lean, homogeneous combustion. However, due to the installation simplicity, lower cost and mainly lower injection pressure, in Hydrogen SI engines PFI is the most common approach. [106]

SI engines typically operate according to the Otto cycle, which is optimized for fuels with high resistance to auto-ignition. This resistance is quantified using the Research Octane Number (RON), which measures how well a fuel can withstand compression without spontaneously igniting. Gasoline has a high RON (approximately 90 to 100 octanes), in contrast, diesel has a much lower RON (typically less than 25 octanes) because it is designed to ignite easily under compression, making it suitable for CI engines.

CI engines, commonly associated with the diesel cycle, rely on the auto-ignition of fuel injected directly into highly compressed air. These engines require higher compression ratios compared to SI engines to

achieve the needed in-cylinder temperatures and pressures. Due to the risk of premature auto-ignition, the most common injection strategy in CI engines is direct injection near top dead center (TDC), typically implemented through high-pressure direct injection (HPDI). However, while in SI engines combustion is initiated immediately by the spark, in CI engines it does not begin right after the start of injection (SOI). Instead, there is a delay period that combines the time required for the fuel to mix with the surrounding air and the ignition delay time (IDT), which is the period needed for the chemical reactions to progress to the point of ignition. This ignition delay governs the first phase of combustion, where a portion of the fuel burns in a premixed mode, releasing energy rapidly. The remaining combustion proceeds in a diffusion-controlled regime, where the burn rate is limited by the mixing of fuel and air. [41, 92]

The combustion characteristics of hydrogen imply different issues to overcome for both SI and CI engines. In SI engines, hydrogen's low ignition energy can lead to uncontrolled ignition events such as pre-ignition and backfiring in the intake manifold. These phenomena not only compromise performance and efficiency but also pose a risk to engine durability. In contrast, hydrogen's relatively high auto-ignition temperature presents challenges for conventional CI combustion, as the in-cylinder conditions during compression may not be sufficient to initiate ignition without assistance. This inhibits reliable auto-ignition, especially at part load or low ambient conditions.

CI engines have a thermodynamic advantage compared to SI engines as they obtain higher efficiencies due to their ability to operate at significantly higher compression ratios. This means that CI engines can extract more useful work from the same amount of fuel which is a decisive factor for heavy-duty transportation. However, as it was mentioned, to be able to combust fuel in CI engines it is essential to address the limitation imposed by the high auto-ignition temperature of hydrogen.

Previous work at Scania, including detailed simulations using the CONVERGE CFD platform, has explored different strategies to overcome the challenge of hydrogen's high auto-ignition temperature in CI engines. Among the ignition concepts investigated were the use of a diesel pilot fuel to start the ignition and preheated hydrogen multiple injection. The diesel pilot strategy was found to provide the most efficient ignition, with the issue that it would not be completely free of carbon emission. In contrast, the preheated multiple injection approach, which was primarily motivated by the goal of achieving completely CO_2-free operation, showed limited potential in terms of efficiency. [41, 92]

Experimental studies have been carried out by Westport Fuel Systems using a Scania 6-cylinder inline engine equipped with specially developed dual-fuel injectors capable of delivering both liquid diesel and gaseous hydrogen. [19, 20] These tests investigated a range of operating conditions with varying diesel pilot quantities to evaluate ignition performance, combustion stability, and efficiency. Although there is strong interest in eliminating the use of diesel entirely to achieve zero-carbon operation, experimental data for fully diesel-free configurations under relevant engine conditions are still lacking. Based on the findings from this work, the diesel pilot strategy has been selected as the baseline approach. A key objective of this thesis is to develop a simulation model that accurately reflects the available experimental results and to determine how the amount and timing of the pilot injection can be optimized to reduce, or potentially eliminate, the use of diesel, without compromising ignition reliability or overall engine performance.

1.6 Key Differences Between Hydrogen and Diesel for CI Engines

The difference in auto-ignition temperature between Hydrogen and Diesel is not the only challenge that the fuel transition for ICE faces. Hydrogen and diesel exhibit significant differences in their physical properties and combustion behavior, which have direct implications for modeling strategies in CI engine simulations. These differences affect fuel injection, combustion modeling, turbulence treatment, and chemical kinetics, requiring special attention when adapting the traditional, well-known, diesel-based CFD workflows to hydrogen-fueled engines.

1.6.1 Fuel Phase and Injection Pressure

A key difference lies in the physical state of each fuel during injection. Diesel is injected as a liquid, typically at pressures exceeding 1000 bar, significantly higher than the in-cylinder pressure at the time

of injection (usually around 100 bar). This large pressure differential ensures that injection duration and mass flow can be considered uniform for all operating conditions, making boundary condition definition simpler and more predictable.

In contrast, hydrogen is injected as a gas, and even in high-pressure direct injection (HPDI) systems, the market available injectors such as the Westport Fuel Systems injector, have typical pressures between 150 and 300 bar (Fuel Rail pressure of 300 bar for Westport's injector) [45]. This lower pressure ratio between fuel and in-cylinder gas leads to higher sensitivity of the injected mass flow to small variations in cylinder pressure. As a result, modeling real hydrogen injection becomes more complex, particularly when aiming for accurate time-resolved fuel delivery under changing crank-angle-dependent conditions.

In earlier studies by Hao Liu [41] and Mark Treacy [93], hydrogen injection was implemented using the same injection strategy regardless of the in-cylinder conditions, effectively simplifying the injection process and avoiding pressure-dependent variability. Later, Diego Antonacci [12] attempted a more realistic approach by including the hydrogen injector geometry in the CFD domain, enabling pressure-controlled injection through an inlet boundary. While this model provided a more detailed representation of the injection process, it required unrealistically low gas temperatures to reproduce experimental trends. Furthermore, the small dimensions of the injector nozzle demanded a substantial reduction of the local mesh size in that region. Although the rest of the domain remained relatively coarse, the small cells near the injector imposed strict Courant-Friedrichs-Lewy (CFL) limitations on the global time step, resulting in increased computational cost, longer simulation times, and convergence difficulties. Ultimately, the added complexity did not yield meaningful improvements in accuracy compared to the simpler approach used by Liu and Treacy.

For this reason, the present study will attempt a middle-ground strategy: modeling variable mass flow injection profiles as a function of time, in crank angle degrees (CADs), for different rail pressures, without explicitly including the injector geometry. This allows more realistic control over injection dynamics than a constant injection strategy, while avoiding the computational burden associated with geometric resolution of the injector.

1.6.2 Chemical Mechanisms

From a chemical kinetics perspective, diesel and hydrogen differ significantly in terms of the complexity and structure of their respective reaction mechanisms. Diesel combustion is typically modeled using surrogate fuels such as *n*-dodecane or *n*-heptane, which involve large and detailed kinetic mechanisms to accurately describe fuel pyrolysis, intermediate species formation, and soot precursor chemistry [60]. These mechanisms often include hundreds of species and thousands of reactions, making them computationally demanding.

In contrast, hydrogen combustion involves no carbon chemistry and follows a much simpler reaction pathway, which significantly reduces the number of species and reactions required in the mechanism [51]. This simplicity not only decreases computational cost but also facilitates faster simulation times and easier integration into CFD solvers.

In this study, both hydrogen and diesel will be injected into the cylinder, with diesel playing a secondary role as a pilot fuel to initiate combustion. This dual-fuel configuration introduces a modeling challenge: the need to select or construct a reaction mechanism that can accurately represent both fuels under the same computational framework. This choice will be discussed in more detail in section 1.10.

1.6.3 Turbulent Schmidt Number: Theoretical Background

The turbulent Schmidt number (Sc_t) represents the ratio between turbulent momentum diffusivity and turbulent mass diffusivity:

$$Sc_t = \frac{\nu_t}{D_t}, \tag{1.6.1}$$

where ν_t is the turbulent viscosity and D_t the turbulent diffusivity of scalar quantities such as mixture fraction or species concentration.

Physically, Sc_t controls how efficiently turbulence mixes scalar quantities compared to how it transports momentum. A low Sc_t increases turbulent mixing, leading to faster homogenization of the fuel–air mixture and broader, more diffusive flames. Conversely, a high Sc_t suppresses scalar mixing, maintaining sharper gradients and delaying ignition. It is therefore a modeling parameter that regulates the effectiveness of turbulent mixing rather than the molecular diffusion of the fuel itself.

According to Tominaga and Stathopoulos (2007) [91], optimal Sc_t values depend on the flow regime and geometry, typically ranging from 0.3 to 1.0 for most engineering flows. Lower values (around 0.3–0.5) are often used in jets and mixing-dominated configurations, where standard RANS models tend to underestimate turbulent diffusion, while higher values (1.0-1.3) are more suitable for stratified or weakly mixed conditions.

In this work, the standard value of $Sc_t = 0.9$ used by STAR-CCM+ will be compared with a reduced value of $Sc_t = 0.5$ to evaluate the sensitivity of turbulent mixing and combustion behavior under hydrogen direct-injection conditions.

1.7 Governing Equations for Reacting Flows

The behavior of reacting flows, such as those found in internal combustion engines, is governed by a set of coupled, non-linear partial differential equations derived from fundamental conservation laws. These include the conservation of mass, chemical species, momentum, and energy. In this section, the governing equations used are presented and briefly discussed. [58]

Conservation of Momentum

$$\frac{\partial \rho u_j}{\partial t} + \frac{\partial \rho u_i u_j}{\partial x_i} = -\frac{\partial p}{\partial x_j} + \frac{\partial \tau_{ij}}{\partial x_i} + \rho \sum_{k=1}^{N} Y_k f_{k,j} = \frac{\partial \sigma_{ij}}{\partial x_i} + \rho \sum_{k=1}^{N} Y_k f_{k,j} \tag{1.7.1}$$

This equation describes the conservation of linear momentum in a reacting, multicomponent fluid. The left-hand side includes the transient and convective transport of momentum. On the right-hand side, the terms represent the pressure gradient, viscous stress tensor τ_{ij}, and possible external body forces acting on each species (e.g., gravity, electromagnetic effects). In combustion applications, the body force term is typically negligible.

Conservation of Mass

$$\frac{\partial \rho}{\partial t} + \frac{\partial \rho u_i}{\partial x_i} = S_i \tag{1.7.2}$$

This equation expresses the conservation of total mass in the system. The first term represents the change in density with time, the second term accounts for the convective transport of mass due to fluid motion, and the third term S_i denotes a mass source term.

Species transport equation (for species k)

$$\frac{\partial \rho Y_k}{\partial t} + \frac{\partial}{\partial x_i}\left(\rho \left(u_i + V_{k,i}\right) Y_k\right) = \dot{\omega}_k \tag{1.7.3}$$

The species transport equation is obtained by applying the continuity equation to the different species. Each chemical species k is transported by convection and diffusion and is produced or consumed by chemical reactions.

Fick's Law for Diffusive Flux

$$J_{k,i} = \rho V_{k,i} Y_k = -\rho D_k \frac{\partial Y_k}{\partial x_i} \tag{1.7.4}$$

Fick's law assumes that diffusion is driven by mass fraction gradients. In turbulent flows, a turbulent diffusion term is typically added using an effective diffusivity.

Species transport equation with Fick's Law:

$$\frac{\partial \rho Y_k}{\partial t} + \frac{\partial \rho u_i Y_k}{\partial x_i} = \frac{\partial}{\partial x_i}\left(\rho D_k \frac{\partial Y_k}{\partial x_i}\right) + \dot{\omega}_k = -\frac{\partial J_{k,i}}{\partial x_i} + \dot{\omega}_k \tag{1.7.5}$$

Applying Flick's law to the previous species transport equation, Equation 1.7.5 is obtained, which is widely used in reacting flow solvers.

Conservation of Energy (Specific Enthalpy Form)

$$\rho \frac{Dh}{Dt} = \frac{\partial \rho h}{\partial t} + \frac{\partial \rho u_i h}{\partial x_i} = \frac{Dp}{Dt} - \frac{\partial q_i}{\partial x_i} + \tau_{ij}\frac{\partial u_i}{\partial x_j} + \dot{Q} + \rho \sum_{k=1}^{N} Y_k f_{k,i} V_{k,i} \tag{1.7.6}$$

This equation describes the conservation of thermal energy using the specific enthalpy h. The heat flux q_i includes conduction and species diffusion contributions:

$$q_i = -\lambda \frac{\partial T}{\partial x_i} + \rho \sum_{k=1}^{N} h_k Y_k V_{k,i} \tag{1.7.7}$$

Here, λ is the thermal conductivity and h_k the specific enthalpy of species k. The term $\frac{Dp}{Dt}$ accounts for pressure work, and $\dot{Q}$ represents any localized external heat source (e.g., ignition).

However, the specific enthalpy energy equation (Equation 1.7.6) is not always easy to implement in CFD solvers therefore the sensible enthalpy equation is normally used:

Conservation of Energy (Sensible Enthalpy Form)

$$\rho \frac{Dh_s}{Dt} = \dot{\omega}_T + \frac{Dp}{Dt} + \frac{\partial}{\partial x_i}\left(\lambda \frac{\partial T}{\partial x_i}\right) - \frac{\partial}{\partial x_i}\left(\rho \sum_{k=1}^{N} h_{s,k} Y_k V_{k,i}\right) + \tau_{ij}\frac{\partial u_i}{\partial x_j} + \dot{Q} + \rho \sum_{k=1}^{N} Y_k f_{k,i} V_{k,i} \tag{1.7.8}$$

where the term $\frac{\partial}{\partial x_i}\left(\rho \sum_{k=1}^{N} h_{s,k} Y_k V_{k,i}\right)$ is often negligible compared to the heat release due to combustion ($\dot{\omega}_T$) or zero if all the species have the same sensible enthalpy.

$$\dot{\omega}_T = -\sum_{k=1}^{N} \Delta h^0_{f,k} \dot{\omega}_k \tag{1.7.9}$$

1.8 Turbulence Modeling

Historically, early approaches to fluid mechanics attempted to solve the Navier-Stokes equations through simplified analytical resolutions. These often relied on assumptions such as inviscid, irrotational, and incompressible potential flow theory. Although such models were useful for understanding idealized behavior, they failed to capture many phenomena observed in real fluid flows, such as flow separation, wake formation, and unsteadiness. [76]

These discrepancies arise from the assumptions made in potential theory, which inherently restrict the solution to attached laminar flow regimes. In reality, laminar flow occurs when viscous forces dominate

over inertial ones, leading to smooth, orderly motion. However, in many practical situations, flows enter the regime known as the turbulent state, which is responsible for the observed deviations.

Turbulence is a complex and chaotic state of fluid motion characterized by irregular fluctuations in velocity and pressure. Turbulent flows exhibit a strongly non-linear and dissipative nature, resulting in complex interactions between velocity fluctuations across a wide range of spatial and temporal scales.

To better understand this transition and the fundamental differences between laminar and turbulent flow, it is useful to examine the full form of the incompressible Navier–Stokes equations, assuming no mass sources or sinks. These equations govern the conservation of mass and momentum in a Newtonian fluid:

Continuity equation (mass conservation):

$$\nabla \cdot \mathbf{u} = 0 \tag{1.8.1}$$

Momentum equation:

$$\frac{\partial \mathbf{u}}{\partial t} + (\mathbf{u} \cdot \nabla)\mathbf{u} = -\frac{1}{\rho}\nabla p + \nu \nabla^2 \mathbf{u} + \mathbf{f} \tag{1.8.2}$$

Each term in the momentum equation has a physical meaning:

- $\frac{\partial \mathbf{u}}{\partial t}$ is the unsteady term.
- $(\mathbf{u} \cdot \nabla)\mathbf{u}$ is the convective or inertial term.
- $-\frac{1}{\rho}\nabla p$ is the pressure gradient term.
- $\nu \nabla^2 \mathbf{u}$ is the viscous diffusion term.
- $\mathbf{f}$ is a generic body force term (e.g., gravity).

The relative importance of inertial against viscous effects is captured by the dimensionless Reynolds number, defined as:

$$\mathrm{Re} = \frac{UL}{\nu} \tag{1.8.3}$$

where U is a characteristic velocity, L a characteristic length, and $\nu = \mu/\rho$ the kinematic viscosity.

For low Reynolds numbers ($\mathrm{Re} \ll 1$), the viscous term dominates and the flow tends to remain laminar. As the Reynolds number increases ($\mathrm{Re} \gg 1$), the inertial term becomes dominant and the turbulence increases. Therefore, the higher the Reynolds number is the more it diverges from potential flow theory.

These turbulent interactions are governed by a hierarchy of swirling flow structures known as eddies. Eddies vary in size from large, energy-containing structures associated with the geometry and boundary conditions, down to the smallest scales where viscosity becomes dominant. Energy cascades from large to small eddies, ultimately being dissipated into heat at the smallest scales, where the turbulence becomes locally isotropic and kinetic energy is converted into thermal energy.

Since analytical solutions to the Navier-Stokes equations are generally intractable for turbulent flows, they must instead be approximated numerically. This is the role of Computational Fluid Dynamics (CFD), a framework that enables researchers and engineers to simulate complex fluid behavior by discretizing the flow domain and solving the governing equations using numerical methods.

One of the main challenges in simulating turbulence lies in its multi-scale nature. Energy is transferred from large, energy-containing eddies to smaller scales through a cascade mechanism, until it is finally dissipated as heat at the smallest scales. Resolving all these scales directly requires extremely fine spatial and temporal resolution, making full-resolution simulations prohibitively expensive for most practical applications.

To overcome this, turbulence models are introduced to represent the statistical effects of the unresolved flow structures. The choice of model depends on the level of fidelity and computational cost desired. The three primary modeling strategies used in CFD are:

- **Direct Numerical Simulation (DNS):** Solves the Navier–Stokes equations directly without any turbulence modeling, resolving all spatial and temporal scales of turbulence. While DNS provides the most accurate results, it is computationally prohibitive for practical applications, particularly in complex geometries or high Reynolds number flows.
- **Large Eddy Simulation (LES):** Resolves the large energy-carrying eddies directly, while modeling the effects of smaller scales using subgrid-scale (SGS) models. LES offers a good compromise between accuracy and cost but remains too expensive for routine use in full-engine simulations, especially over many cycles.
- **Reynolds-Averaged Navier–Stokes (RANS):** Instead of resolving all turbulent fluctuations, RANS equations govern the time-averaged flow, with turbulence effects accounted for through modeling. This approach offers a substantial reduction in computational cost and is widely used in industrial applications where multiple design iterations are required.

Given the scale and complexity of internal combustion engine simulations and the need for iterative design processes, the RANS approach is adopted in this work a it allows the modeling of key in-cylinder flow features while maintaining feasible computational requirements.

1.8.1 RANS

The Reynolds-Averaged Navier–Stokes (RANS) approach can be explained using the dimensionless form of the incompressible Navier–Stokes equations, assuming constant density and viscosity. [30, 59] Under these assumptions, the governing equations reduce to the following:

Momentum equation:

$$\frac{\partial \mathbf{u}}{\partial t} + \nabla \cdot (\mathbf{u}\mathbf{u}) + \frac{1}{\rho}\nabla p - \frac{1}{\mathsf{Re}}\nabla \cdot \nabla \mathbf{u} = 0 \tag{1.8.4}$$

Continuity equation:

$$\nabla \cdot \mathbf{u} = 0 \tag{1.8.5}$$

Here, $\mathbf{u}$ is the velocity vector, p the pressure, ρ the density (assumed constant), and Re the Reynolds number.

To derive the RANS equations, we decompose the instantaneous velocity field into its mean and fluctuating components using the Reynolds decomposition:

$$\mathbf{u} = \langle \mathbf{u} \rangle + \mathbf{u}' \tag{1.8.6}$$

where $\langle \mathbf{u} \rangle$ is the ensemble-averaged velocity and $\mathbf{u}'$ the fluctuating part. This decomposition can also be applied to pressure and other quantities if needed. Substituting the decomposition into the Navier–Stokes equations and applying the averaging operator yields the incompressible RANS equations:

RANS momentum equation:

$$\frac{\partial \langle \mathbf{u} \rangle}{\partial t} + \nabla \cdot (\langle \mathbf{u} \rangle \langle \mathbf{u} \rangle) + \frac{1}{\rho}\nabla \langle p \rangle - \frac{1}{\mathsf{Re}}\nabla \cdot \nabla \langle \mathbf{u} \rangle = -\nabla \cdot \langle \mathbf{u}'\mathbf{u}' \rangle \tag{1.8.7}$$

RANS continuity equation:

$$\nabla \cdot \langle \mathbf{u} \rangle = 0 \tag{1.8.8}$$

The new term $\langle \mathbf{u}'\mathbf{u}' \rangle$ that appears on the right-hand side of the momentum equation is known as the Reynolds stress tensor:

$$\tau_{ij} = -\langle u_i' u_j' \rangle \tag{1.8.9}$$

This tensor represents the additional apparent stresses introduced by turbulent fluctuations and must be modeled to close the system of equations, as it introduces more unknowns than equations.

To better understand its behavior, one can derive a conservation law for each component of the Reynolds stress tensor. This leads to theReynolds Stress Transport (RST) equation, which in general form reads:

$$\begin{aligned}\frac{d\langle u_i' u_j'\rangle}{dt} + \langle u_k\rangle \frac{\partial \langle u_i' u_j'\rangle}{\partial x_k} = &- \left(\langle u_i' u_k'\rangle \frac{\partial \langle u_j\rangle}{\partial x_k} + \langle u_j' u_k'\rangle \frac{\partial \langle u_i\rangle}{\partial x_k} \right) + \frac{\partial \langle u_i' u_j' u_k'\rangle}{\partial x_k} \\ &+ \frac{1}{\mathsf{Re}} \frac{\partial^2 \langle u_i' u_j'\rangle}{\partial x_k \partial x_k} + \frac{1}{\rho} \left(\frac{\partial \langle u_i' p'\rangle}{\partial x_j} + \frac{\partial \langle u_j' p'\rangle}{\partial x_i} \right) \\ &+ \left\langle \frac{p'}{\rho} \left(\frac{\partial u_i'}{\partial x_j} + \frac{\partial u_j'}{\partial x_i} \right) \right\rangle - \frac{2}{\mathsf{Re}} \left\langle \frac{\partial u_i'}{\partial x_k} \frac{\partial u_j'}{\partial x_k} \right\rangle \end{aligned} \tag{1.8.10}$$

$$\frac{d\langle u_i' u_j'\rangle}{dt} + K_{ij} = P_{ij} + T_{ij} + D_{ij}^{\nu} + D_{ij}^{p} + \Phi_{ij} - \varepsilon_{ij} \tag{1.8.11}$$

Each term in the equation has a physical interpretation:

- K_{ij}: Advection
- P_{ij}: Production of turbulent kinetic energy
- T_{ij}: Turbulent transport
- D_{ij}^{ν}: Viscous diffusion
- D_{ij}^{p}: Pressure diffusion
- Φ_{ij}: Pressure–strain correlation
- ε_{ij}: Dissipation

However, this equations also introduces new unknowns. This means that to continue this resolution, it would be needed to derive new conservation laws for every unknown, which would generate even higher-order unknowns [30]. Therefore, it is not feasible to directly solve the transport equations for the Reynolds stress tensor. Instead, this issue is addressed by the development of turbulence models. These can be broadly categorized into two main approaches: Eddy Viscosity Models (EVM) and Reynolds Stress Models (RSM) .

1. Eddy Viscosity Models (EVM): These models assume that the fluctuations introduced in the Reynolds stresses are proportional to the mean rate of strain by a factor called turbulent viscosity ν_t. They are based on the Boussinesq hypothesis:

$$\tau_{ij} = 2\nu_t S_{ij} - \frac{2}{3}\delta_{ij} k \tag{1.8.12}$$

where S_{ij} is the mean strain rate tensor, k is the turbulent kinetic energy, and δ_{ij} is the Kronecker delta. EVMs include:

- 0-equation models (algebraic models, e.g. Prandtl mixing length model)
- 1-equation models (e.g. Prandtl one-equation model, Spalart-Allmaras)
- 2-equation models (e.g. k–ϵ, k–ω)
- Nonlinear EVMs that try to capture some anisotropy without solving full stress transport equations

2. Reynolds Stress Models (RSM): These models do not introduce the assumption of isotropy, instead they attempt to solve the RST. To achieve this, they solve transport equations for each component of the Reynolds stress tensor. RSMs are in theory a better representation of the RST. However, in practice they do not necessarily behave better than EVM models. Usually, they provide better predictions in complex flows involving anisotropy, curvature, rotation, or strong swirl due to their anisotropic nature. Still, they have certain drawbacks, such as being computationally expensive and sensitive to numerical stability.

Due to the need for computational efficiency in this work, especially when simulating engine cycles and testing multiple configurations, a two-equation eddy viscosity model is selected. These models provide a good balance between accuracy and cost.

1.8.2 Two-equations RANS Eddy Viscosity Models

Two-equation eddy viscosity models (EVM) are among the most commonly used approaches in RANS turbulence modeling. They are based on the Boussinesq approximation, which assumes that the Reynolds stress tensor can be related to the mean strain rate through a scalar turbulent viscosity ν_t. In two-equation models, ν_t is computed from the solution of two additional transport equations.

The two most popular formulations are the k–ϵ and k–ω models. Both involve solving for the turbulent kinetic energy k, which represents the intensity of turbulence (i.e., the energy per unit mass contained in velocity fluctuations), and a second variable that determines the scale or rate of dissipation of that energy.

Turbulent kinetic energy k is defined as:

$$k = \frac{1}{2}\langle u_i' u_i' \rangle \tag{1.8.13}$$

It satisfies the general transport equation:

$$\frac{\partial k}{\partial t} + \mathbf{u} \cdot \nabla k = P_k - \epsilon + \nabla \cdot \left[\left(\nu + \frac{\nu_t}{\sigma_k} \right) \nabla k \right] \tag{1.8.14}$$

where P_k is the production of turbulent kinetic energy.

k–ϵ model

In the standard k–ϵ model [35], the second equation solves for ϵ, the dissipation rate of k:

$$\frac{\partial \epsilon}{\partial t} + \mathbf{u} \cdot \nabla \epsilon = C_{\epsilon 1} \frac{\epsilon}{k} P_k - C_{\epsilon 2} \frac{\epsilon^2}{k} + \nabla \cdot \left[\left(\nu + \frac{\nu_t}{\sigma_\epsilon} \right) \nabla \epsilon \right] \tag{1.8.15}$$

The eddy viscosity is then modeled as:

$$\nu_t = C_\mu \frac{k^2}{\epsilon} \tag{1.8.16}$$

In the **RNG k–ϵ model** [104], derived from Renormalization Group theory, the transport equations retain the same general structure, but introduce two key differences:

- C_μ is derived from the RNG theory, rather than treating it as a constant.
- A modified term in the ϵ equation to account for high strain rates:

$$\frac{\partial \epsilon}{\partial t} + \mathbf{u} \cdot \nabla \epsilon = C_{\epsilon 1} \frac{\epsilon}{k} P_k - C_{\epsilon 2} \frac{\epsilon^2}{k + \beta \epsilon / P_k} + \nabla \cdot \left[\left(\nu + \frac{\nu_t}{\sigma_\epsilon} \right) \nabla \epsilon \right] \tag{1.8.17}$$

These modifications improve accuracy in rapidly strained and swirling flows, making the RNG model particularly well suited for engine-like environments.

The realizable k–ϵ model [83] also retains the general structure of the transport equations, but introduces:

- An alternative formulation of the eddy viscosity coefficient C_μ that ensures mathematical consistency (i.e., realizability) with known turbulence constraints.

$$C_\mu = \frac{1}{A_0 + A_s \frac{k U^*}{\epsilon}} \tag{1.8.18}$$

  where $U^* = \sqrt{S_{ij} S_{ij} + \tilde{\Omega}_{ij} \tilde{\Omega}_{ij}}$

- A modified dissipation equation derived from the mean-square vorticity equation, leading to better predictions in flows with rotation, boundary layer separation, and high curvature.

$$\frac{\partial \epsilon}{\partial t} + \mathbf{u} \cdot \nabla \epsilon = \rho C_1 S \epsilon - \rho C_2 \frac{\epsilon^2}{k + \sqrt{\nu \epsilon}} + \nabla \cdot \left[\left(\nu + \frac{\nu_t}{\sigma_\epsilon} \right) \nabla \epsilon \right] \tag{1.8.19}$$

where:

- $S = \sqrt{2 S_{ij} S_{ij}}$ is the magnitude of the mean strain rate tensor,
- $C_1 = \max\left(0.43, \frac{\eta}{\eta+5}\right)$, with $\eta = \frac{Sk}{\epsilon}$.

k–ω model

Alternatively, the k–ω model [99] uses the specific dissipation rate ω, defined as:

$$\omega = \frac{\epsilon}{\beta^* k} \tag{1.8.20}$$

Its transport equations are typically written as:

$$\frac{\partial k}{\partial t} + \mathbf{u} \cdot \nabla k = P_k - \beta^* k \omega + \nabla \cdot \left[\left(\nu + \sigma_k \nu_t \right) \nabla k \right] \tag{1.8.21}$$

$$\frac{\partial \omega}{\partial t} + \mathbf{u} \cdot \nabla \omega = \alpha \frac{\omega}{k} P_k - \beta \omega^2 + \nabla \cdot \left[\left(\nu + \sigma_\omega \nu_t \right) \nabla \omega \right] \tag{1.8.22}$$

The eddy viscosity in this case is computed as:

$$\nu_t = \frac{k}{\omega} \tag{1.8.23}$$

The k–ω model performs better in the near-wall region and does not require wall functions, but can be sensitive to freestream conditions.

Model selection

For the purposes of this study, turbulence modeling within the k–ϵ and k–ω families has been reviewed in order to identify the most suitable approach for in-cylinder simulations. Both formulations have distinct advantages depending on the dominant flow characteristics and boundary treatment strategies.

Although both k–ϵ and k–ω models have been considered based on literature, the k–ϵ family appears to be the most promising for in-cylinder flows, which are typically dominated by swirling bulk motion, injection and high pressure variations rather than near-wall effects. This choice is further supported by the historical prevalence of the k–ϵ model in internal combustion engine (ICE) simulations, both in academia and industry (including Scania) [11, 56].

It is worth noting that the choice of turbulence model may need to be revisited if the computational domain is extended to include the fuel injectors or other features located in the upper part of the cylinder head. In such cases, flow near complex geometries and walls becomes more dominant, and accurate resolution of the boundary layer is critical. Under these conditions, the k–ω model could become more advantageous due to its superior near-wall behavior and ability to integrate wall-bounded effects without relying on empirical wall functions [24].

As previously mentioned, within the k–ϵ family, two enhanced versions are commonly used: the RNG and the Realizable models. A study from the University of Modena [11], which analyzed non-combusting hydrogen-fueled engines using Particle Image Velocimetry (PIV) and Planar Laser-Induced Fluorescence (PLIF), compared both models in STAR-CCM+ and concluded that the RNG variant provided better robustness and agreement with experimental results. Based on this literature review, the RNG k–ϵ model is selected as the baseline approach for this study. However, if future work include modeling the hydrogen injector geometry explicitly, the k–ω model may become the preferred option, as indicated in the literature, due to its improved performance in near-wall flow resolution. [24]

1.9 Turbulent Combustion Modeling in STAR-CCM+

The selection of an appropriate turbulent combustion model for simulating hydrogen-diesel dual fuel engines in STAR-CCM+ requires an evaluation of the modeling strategies provided within the software. Figure 1.18 presents a comprehensive overview of the typical RANS configurations available. The main differences between the models is weather they are suitable for premixed or non-premixed combustion as well as weather they are based on flamelet models or reaction species transport models.

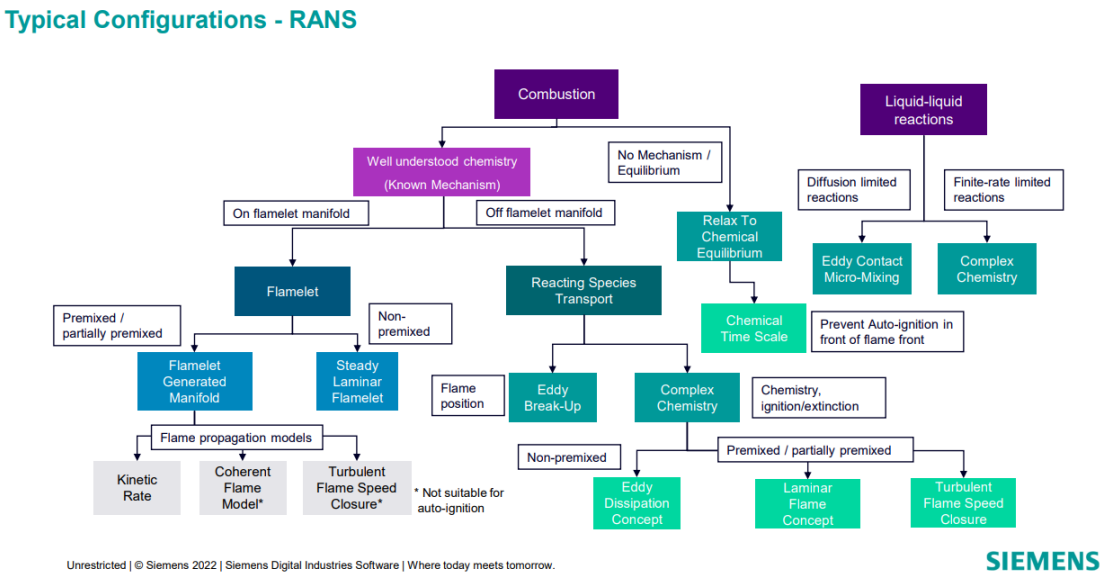

Figure 1.18: Typical combustion model configurations available in STAR-CCM+ [61].

Typically, in ICEs, there is a need to use detailed or reduced chemical mechanisms to accurately represent the chemical kinetics of fuel combustion. Therefore, a chemical time scale model is not a suitable option for this study. The reason why chemical mechanisms are needed to simulate ICEs is to predict ignition delays and capture effects like the local temperature, pressure, and mixture composition on autoignition as well as flame propagation. This is especially critical for fuels like hydrogen or diesel, where ignition behavior, intermediate species formation, and pollutant generation are highly sensitive to local thermochemical conditions. As a result, to model combustion accurately, it is necessary to use either a Reacting Species Transport Model, which solves for species concentrations and temperature with the chemical source terms from a reaction mechanism, or a flamelet model, which accounts for detailed chemistry effects while reducing computational cost through tabulation techniques.

1.9.1 Flamelet Models

Flamelet models reduce computational cost by decoupling the chemistry from the flow field. In this approach, the turbulent flame is approximated as an ensemble of laminar flamelets, which are precomputed one-dimensional solutions of canonical flames. These are stored in combustion tables and queried during the simulation. These models are valid when the system operates in the flamelet regime, where chemical reactions are much faster than turbulent mixing. They are particularly efficient for steady, diffusion-dominated flames and two-stream mixing systems. [86]

One of the main advantages of flamelet models is their computational efficiency, as they avoid solving the detailed kinetics during runtime. Simcenter STAR-CCM+ supports fully integrated, parallelized combustion table generation using the robust CVODE solver, eliminating the need for external chemistry solvers. The software also includes adaptive tabulation, which reduces table size without compromising accuracy by refining only where needed, according to user-defined tolerances. Furthermore, the framework can exploit GPU acceleration and captures turbulence-chemistry interactions using as-

sumed shape PDFs for fluctuations. This makes flamelet models particularly attractive for large parametric studies or real-time simulation contexts where computational resources are limited.

However, flamelet models rely on the assumption of fast chemistry and are limited in their ability to capture phenomena such as ignition and extinction, transient combustion, or the formation of slowly evolving pollutants (e.g., NO_x, CO, soot). They also face limitations in handling systems with complex or multiple fuel injection strategies. [61]

1.9.2 Reacting Species Transport Models

This modeling strategy solves the full transport equations for all chemical species, accounting for convection, diffusion, and detailed reaction kinetics directly in each computational cell. Reacting Species Transport models are applicable to a wide range of combustion conditions, particularly when chemical and mixing timescales are comparable or when the system lies outside the flamelet regime. [87]

The main advantage of this approach lies in its general applicability and high fidelity. It enables detailed tracking of species transport and reaction progress in complex, kinetically controlled regimes, and is particularly accurate for multi-stream injection, transient ignition and extinction phenomena, and the formation of slowly evolving pollutant species such as NO_x, CO, and soot. However, these benefits come at the expense of computational efficiency. The model can be CPU-intensive, especially when large reaction mechanisms and fine meshes are involved. Additionally, unlike flamelet models, it does not inherently include turbulence-chemistry interaction through assumed shape PDFs, which may limit the representation of subgrid-scale fluctuations in scalar quantities.

1.9.3 Model Selection Based on In-Cylinder Conditions

To accurately capture the formation of slowly evolving pollutants such as CO_2 and NO_x, a detailed representation of chemical kinetics is required. This necessitates the use of models capable of resolving ignition and extinction phenomena, particularly relevant during hydrogen injection, as well as the effects of multi-stream combustion with sequential injection of diesel and hydrogen. Since these processes involve a precise chemical representation as well as a reliable ignition behaviour, Reacting Species Transport models are better suited to accurately capture the relevant physical and chemical behavior.

1.9.4 Available Models within Reacting Species Transport

Simcenter STAR-CCM+ offers two main approaches under the Reacting Species Transport framework: Complex Chemistry (CC) and Eddy Break-Up (EBU). These models differ significantly in both their treatment of combustion and their applicability, depending on the dominant physical and chemical phenomena of interest.

Complex Chemistry (CC) focuses on resolving the detailed chemical kinetics by solving transport equations for all species and evaluating reaction source terms through stiff ODE integration. This model is designed for simulations where chemical accuracy is crucial, such as those involving ignition and extinction, slow pollutant formation, and multi-fuel or multi-stream combustion. [84]

Eddy Break-Up (EBU) is a combustion model designed for reacting flows with fast chemistry, where the reaction rate is primarily governed by turbulent mixing of reactants and heat. In its standard form, EBU assumes that species are instantaneously burned once mixed, with the reaction rate determined by the turbulent mixing time scale. This model does not resolve detailed chemical kinetics, which significantly reduces computational cost, making it particularly suitable when the main objective is to predict the flame position rather than intermediate species or pollutant formation. It is well-suited for configurations such as gas turbines or industrial furnaces, where combustion can be represented by one or two global reactions and chemical kinetics are not rate-limiting. However, it is not appropriate for systems exhibiting ignition/extinction behavior or involving slow-forming pollutants, where finite-rate kinetics are essential. [85]

Since our study focuses on an internal combustion engine operating under conditions where autoignition is critical and the formation of slow-forming pollutants, such as NOx, must be accurately captured, we opt for the Complex Chemistry approach. This model resolves finite-rate chemical kinetics, allowing us to simulate both ignition phenomena and pollutant formation with the necessary level of detail.

1.9.5 Complex Chemistry Model

The Complex Chemistry (CC) model in Simcenter STAR-CCM+ resolves chemical reactions through the integration of stiff ordinary differential equations using the CVODE solver. The model is based on the species transport equation (see Equation 1.7.5), and it takes advantage of the separation between the chemical and physical time scales [84]. In the notation used in Siemens documentation:

$$\frac{\partial}{\partial t}(\rho Y_i) + \frac{\partial}{\partial x_j}(\rho u_j Y_i + F_{k,j}) = \omega_i \tag{1.9.1}$$

At the beginning of each physical time step, the chemical state is advanced independently by integrating the chemical source terms over the chemical time scale τ. The evolution of the species mass fractions is expressed as:

$$Y_i^* = Y_i + \int_0^\tau r_k(Y, T, p)\, dt \tag{1.9.2}$$

where Y_i represents the mass fraction of species i, τ is the chemical integration time, T is the temperature and r_k is the net reaction rate for species which is calculated as:

$$r_k = k_f [A]^{\nu'_A} [B]^{\nu'_B} \ldots - k_b [C]^{\nu''_C} [D]^{\nu''_D} \ldots \tag{1.9.3}$$

where:

- r_k is the net reaction rate of reaction k [mol·m^{-3}·s^{-1}],
- k_f, k_b are the forward and backward rate constants,
- $[A]$, $[B]$, $[C]$, $[D]$ are the molar concentrations of the reacting species,
- ν'_i, ν''_i are the stoichiometric coefficients of species i for reactants and products, respectively.

Subsequently, the species transport equation is solved using an explicit reaction source term based on the updated chemical state:

$$\omega_i = \rho f \left(\frac{Y_i^* - Y_i}{\tau} \right) \tag{1.9.4}$$

where ω_i is the source term for species i, ρ is the local density, and f is the mean reaction rate multiplier. The values of τ and f depend on the specific submodel used within the Complex Chemistry framework and will be discussed in the following section.

The integration of the chemical state is carried out using a constant pressure reactor formulation, where the equations for species and temperature evolution are:

$$\frac{dY_k}{dt} = \frac{\dot{\omega}_k}{\rho} \tag{1.9.5}$$

$$\frac{dT}{dt} = \frac{-\sum_{k=1}^{n} \omega_k h_k}{\rho C_p} \tag{1.9.6}$$

These equations are solved numerically using Jacobian-based methods within the CVODE solver. As Jacobian evaluation is computationally expensive, acceleration strategies such as In-Situ Adaptive Tabulation (ISAT), Clustering, and Dynamic Mechanism Reduction are available to reduce computational cost.

Turbulence–chemistry interaction is handled within the Complex Chemistry framework, which incorporates turbulent diffusivity via the turbulence model. Additional closures can be added to better capture the coupling between turbulence and reaction rates, including the Eddy Dissipation Concept (EDC), the Laminar Flame Concept (LFC), and the Turbulent Flame Speed Closure (TFSC).

Selection of the Complex Chemistry Model

To determine the most suitable combustion model, the expected in-cylinder thermochemical conditions must be considered. Previous studies by Liu [41] and Treacy [92] have shown that diesel fuel is injected first, initiating combustion and generating a high-temperature region into which hydrogen is subsequently introduced. The injection strategies from these investigations are shown in Figure 1.19, where the left panel illustrates the energy injection profile reported by Liu, and the right panel displays the mass flow rate profile presented by Treacy.

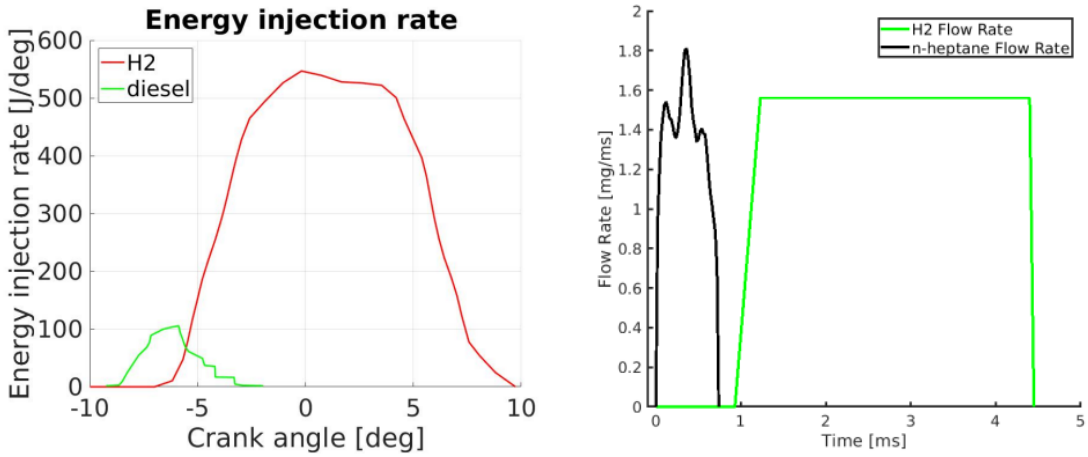

Figure 1.19: Left: Energy injection profile (Liu) [41]. Right: Mass flow profile (Treacy)[92].

According to Liu [41], at -7 CAD ATDC, the diesel pilot creates a region with temperatures exceeding 1200 K, favorable for hydrogen ignition. At -5 CAD ATDC, cold hydrogen is injected into this high-temperature zone. The hydrogen jet ignites around -3.6 CAD ATDC. The resulting flame interacts with the cold wall, which decelerates the reaction kinetics; however, upstream, the reactive hydrogen jet continues to release heat. These observations suggest that the combustion process transitions from premixed or partially premixed conditions towards non-premixed regimes. Therefore, models capable of capturing multi-stream, transient, and partially premixed combustion, along with pollutant formation, are required.

Within the Complex Chemistry framework in Star-CCM+, turbulence–chemistry interaction can be handled using different closures. Among the available options, the Eddy Dissipation Concept (EDC) is best suited for diffusion-dominated, non-premixed combustion and is therefore not appropriate for the present case. Between the two remaining alternatives, the Turbulent Flame Speed Closure (TFSC) and the Laminar Flame Concept (LFC), both models will be considered, as each offers a different approach to describing flame propagation under turbulent and (partially) premixed conditions. While TFSC relies on a precomputed table for the local flame speed (LFS), LFC dynamically computes the LFS at each iteration based on local flow and mixture properties. These differences in formulation and computational behavior will be discussed in more detail in a later section.

1.9.6 Laminar Flame Concept (LFC)

The Laminar Flame Concept (LFC) is a combustion model available in STAR-CCM+ that builds directly on the Complex Chemistry framework, but with a simplified treatment of turbulence-chemistry interactions. In contrast to the Turbulent Flame Speed Closure (TFSC) model, which explicitly modifies the source term using turbulent flame speed correlations, LFC assumes that the mean reaction rate is directly given by the detailed chemistry without additional scaling [88].

The reaction source term is directly obtained from the detailed mechanism:

$$\omega_i = \rho\dot{\omega}_i = \rho\left(\frac{Y_i^* - Y_i}{\tau}\right), \tag{1.9.7}$$

corresponding to a mean reaction-rate multiplier $f = 1$. The characteristic time scale τ equals the local residence time:

$$\tau = \tau_{\mathsf{res}}. \tag{1.9.8}$$

which is computed from local flow conditions. Thus, the mean species source term is obtained directly from the detailed chemical mechanism without additional turbulence correction.

Turbulence effects are still present in LFC but only implicitly, through the enhanced turbulent diffusivity provided by the turbulence model. This leads to an effective flame thickness larger than the laminar one, and to a propagation speed faster than the purely laminar flame, both controlled by the chosen turbulent Schmidt and Prandtl numbers. However, unlike TFSC or EDC, there is no explicit dependence on turbulent flame speed correlations or sub-grid mixing models.

The main advantage of LFC is that it provides a direct and physics-based representation of the chemical kinetics, as no empirical flame speed correlations are required. This makes it attractive for cases where detailed mechanisms are available and accurate representation of hydrogen chemistry is needed. At the same time, its simplicity means that turbulence–chemistry interactions are not explicitly resolved, which can limit its predictive accuracy in highly turbulent regimes compared to TFSC.

1.9.7 Turbulent Flame Speed Closure (TFSC)

The Turbulent Flame Speed Closure (TFSC) model is an extension of the Complex Chemistry framework that enhances the modeling of premixed and partially premixed combustion by incorporating the effect of turbulent flame propagation into the reaction rate [88]. The core idea is that in regions where premixed combustion is identified (using the Takeno index), the molecular diffusion term is suppressed and the reaction source term from chemistry is scaled with a factor F_{TFC} that depends on the ratio between turbulent and laminar flame speeds:

$$\frac{\partial \rho Y_k}{\partial t} + \nabla \cdot (\rho \vec{V} Y_k) - \nabla \cdot (\rho D \nabla Y_k) = F_{\mathsf{TFC}} \rho \dot{\omega}_k, \tag{1.9.9}$$

where Y_k is the mass fraction of species k, D is the diffusion coefficient, and $\dot{\omega}_k$ is the reaction source term from Complex Chemistry. The multiplier F_{TFC} is defined as:

$$F_{\mathsf{TFC}} = \frac{\dot{\omega}_c^{tfc}}{\dot{\omega}_c^{cc}}, \tag{1.9.10}$$

where $\dot{\omega}_T^c$ is the target turbulent reaction rate.

Several formulations, or closures, have been proposed in the literature to describe how the mean turbulent reaction rate couples with flame propagation. The work of Zimont and Lipatnikov [111] introduced a physically consistent closure for premixed turbulent combustion, in which the mean reaction rate is linked to the turbulent burning velocity and the gradient of the progress variable. Their model assumes

that turbulence increases the flame surface area while the local laminar structure of the flame remains unchanged. This approach has since become the theoretical foundation for many turbulent flame speed models.

In the formulation in Star-CCM+, the turbulent reaction rate includes contributions from both the flame propagation and stratification effects in the residual and equilibrium gases, and is expressed as:

$$\dot{\omega}_T^c = -\rho_u S_t \cdot \nabla c + (1-c)\,\rho_u S_t \cdot \nabla Y_c + c\,\rho_u S_t \cdot \nabla Y_{\mathsf{eq}}, \tag{1.9.11}$$

where ρ_u is the density of unburnt gases, c is the progress variable, Y_c is the unburnt conditional mass fraction of the tracking species, and Y_{eq} is its equilibrium value. A wall-quenching correction is also applied near solid boundaries, based on a Peclet-number formulation [63].

TFSC requires two main inputs:

1. A definition of the laminar flame speed S_L, which reflects the chemical and thermodynamic properties of the mixture.
2. A correlation to compute the turbulent flame speed S_t, which incorporates the influence of turbulence on flame propagation.

The laminar flame speed S_L can be implemented in STAR-CCM+ using:

- The correlations of Metghalchi–Keck [44] or Gülder [28]. Both originally developed for hydrocarbon fuels, which express S_L as a function of equivalence ratio, pressure, and temperature. These correlations perform well under stoichiometric conditions but diverge significantly at lean conditions, limiting their applicability for hydrogen.
- Precomputed laminar flame speed tables provided by Siemens, which have been designed for hydrogen–air mixtures.

Once S_L is defined, the turbulent flame speed S_t is obtained using additional models. STAR-CCM+ provides two main correlations:

- The Zimont model [109], which relates S_t to turbulence intensity, laminar flame speed, laminar flame thickness, and integral length scale. It includes a stretch factor representing the probability of unquenched flamelets, making it sensitive to turbulence intensity and diffusivity.

  $$S_t = 0.5\,G(w)^{3/4} S_L^{1/2} \alpha_u^{-1/4} I_t^{1/4}, \tag{1.9.12}$$

  where w is the turbulent velocity fluctuation, α_u the unburnt thermal diffusivity, and I_t the integral turbulence length scale. The stretch factor $G(w)$ accounts for the probability of unquenched flamelets based on the log-normal distribution of the turbulent dissipation rate.
- The Peters model [57], which defines S_t as a function of S_L, turbulence length scales, and thermal diffusivity, providing a more stable but less nonlinear response.

  $$S_t = S_L(1+\sigma_t), \tag{1.9.13}$$

  where σ_t depends on turbulence intensity and integral scale, providing a smoother transition between laminar and turbulent regimes.

This modular structure means that TFSC couples a laminar flame speed model (Metghalchi, Gülder, or precomputed tables) with a turbulent flame speed model (Zimont or Peters) to calculate the effective turbulent flame speed.

Choice of Turbulent Flame Speed Closure Model for Hydrogen Combustion

Several studies have assessed the performance of these models for hydrogen. Zhao et al. [108] compared Zimont and Peters using turbulent expanding flames in hydrogen-air and methane-hydrogen blends. Their results showed that the Zimont correlation most accurately captured the nonlinear increase in flame speed due to hydrogen enrichment and turbulence intensity, while Peters underestimated this effect.

Other works confirm these trends. Tidswell et al. [90] and Muppala et al. [46] reported that the Zimont model performs well up to about 60% hydrogen enrichment but diverges beyond that. Zhao et al. [107] further observed that while Zimont is accurate in wrinkled and corrugated flamelet regimes, Peters may be preferable near the laminar flamelet regime due to its stability in weak flame conditions.

Based on these findings, the TFSC model used in this work combines the Siemens precomputed laminar flame speed table with the Zimont turbulent flame speed correlation. This configuration should ensure that hydrogen laminar flame properties are captured accurately while applying a turbulent flame speed formulation validated for hydrogen–air mixtures. It is therefore expected to provide a robust description of turbulent flame propagation in the present dual-fuel hydrogen–diesel engine conditions, while acknowledging the known limitations of the Zimont model at very high hydrogen fractions.

1.10 Chemical Reaction Mechanisms

In order to model combustion phenomena accurately in CFD simulations, it is essential to couple fluid dynamics with chemical kinetics. This is done through reaction mechanisms, which describe the series of elementary chemical reactions that occur during the combustion of a given fuel. These mechanisms go beyond the global reaction equations and aim to capture the detailed pathways through which fuel is converted into products, a simple example is the combustion of hydrogen:

$$2H_2 + O_2 \rightarrow 2H_2O \tag{1.10.1}$$

While this overall reaction is useful for conceptual understanding, it does not occur directly. Instead, combustion proceeds through a network of elementary reactions involving intermediate species such as H, O, OH, HO_2, and H_2O_2. A simplified version of the hydrogen reaction mechanism includes the following key reactions [94]:

$$H_2 + O_2 \rightarrow HO_2 + H \tag{1.10.2}$$
$$H + O_2 \rightarrow OH + O \tag{1.10.3}$$
$$OH + H_2 \rightarrow H_2O + H \tag{1.10.4}$$
$$H + O_2 + M \rightarrow H_2O + M \tag{1.10.5}$$
$$\tag{1.10.6}$$

There are many validated mechanisms available in the literature and open databases. These mechanisms can range from very detailed (thousands of species and reactions) to simplified versions optimized for computational efficiency. In the automotive industry, where diesel combustion has been extensively studied, several well-established mechanisms are used, especially for surrogate fuels like n-heptane and n-dodecane. Notable examples include the ARAMCO mechanism, the C3 mechanism or the LLNL mechanisms among others.

These detailed mechanisms are capable of reproducing autoignition behavior, flame structure, and emissions of real diesel fuels. However, due to their computational cost, they are often simplified using mechanism reduction techniques. Examples of smaller mechanisms include those developed by Yao et al. [105], Ranzi et al. [64] or Gustavsson et al. [50]. In contrast, mechanisms for pure hydrogen combustion are typically smaller in size, involving fewer than 20 species and 50 reactions, some examples are Burke et al. [17] or Conaire et al. [113]

The case studied in this work, however, involves the injection of both hydrogen and diesel fuel in a compression-ignition engine. This raises the question of how to model dual fuel combustion. While diesel mechanisms do include hydrogen chemistry, the equations concerning hydrogen are often simplified or reduced, especially in smaller diesel mechanisms, as hydrogen-related pathways are not dominant in typical diesel applications.

In an ideal scenario, a combined reaction mechanism would capture the combustion characteristics of both diesel and hydrogen accurately. In practice, however, most studies rely on diesel mechanisms even when hydrogen is present, since they already incorporate a basic hydrogen sub-mechanism through the radicals involved in hydrocarbon oxidation [12, 41, 60, 92].

Diesel combustion mechanisms have undergone decades of development and validation, resulting in reduced models that are both computationally feasible and widely adopted in engine simulations. This reduction is necessary because the full chemical description of diesel fuels involves thousands of reactions, making direct application impractical. In contrast, hydrogen combustion mechanisms are intrinsically much simpler and therefore easier to represent, although their development and validation are still less extensive. Despite this progress, only a limited number of mechanisms have been developed specifically for dual-fuel diesel–hydrogen combustion. Some studies suggest that combining a reduced diesel mechanism with a detailed hydrogen mechanism can provide advantages in dual-fuel configurations, particularly when hydrogen serves as the dominant energy carrier. This would allow improved prediction accuracy without a significant increase in computational cost. For instance, Karimi et al. [36] combines the Patel diesel mechanism [55] with a detailed hydrogen mechanism by Kéromnès et al. [38] which is also recommended by Olm et al.[51]. Similarly, von Helldorff et al. [96] uses a modified version of the n-heptane mechanism by Ra et al. [62], excluding the iso-octane part, and coupled it with a hydrogen mechanism by Saxena et al. [79].

In the case of von Helldorff, the study provides a direct comparison between using only the diesel mechanism and the combined version that includes hydrogen reactions. The results show a slight improvement in pressure prediction when the hydrogen mechanism is included, although the comparison is limited to only pressure curves. A more thorough evaluation would require additional performance metrics to determine what are all the advantages of including the hydrogen mechanism.

Based on the previous considerations, two configurations stand as the most attractive alternatives to be evaluated in this study: one using a conventional diesel mechanism, specifically the Gustavsson n-heptane mechanisms [27], which has been employed in previous Converge simulations by Liu [41], and another using both a diesel mechanism and a modified version that incorporates a detailed hydrogen mechanism, likely following the approach proposed by von Helldorff et al. [96]. In addition, other mechanisms that have given a promising result could be implemented. [51, 65]

1.11 Modelling Strategy and Research Questions

In this paper, the main challenges involved in modeling hydrogen–diesel dual-fuel combustion in compression ignition (CI) engines are outlined, together with the rationale behind the simulation strategy adopted in this thesis. Particular attention is given to the physical modelling decisions required in STAR-CCM+, including turbulence and combustion modelling, injection strategy, chemical kinetics, and the unique properties of hydrogen that demand specialised approaches.

Although modelling of conventional diesel engines is well established, and extensive research exists on hydrogen combustion, relatively few studies focus on configurations in which hydrogen is the main fuel and diesel acts only as a pilot. This limited availability of validated datasets and modelling benchmarks makes it difficult to directly apply existing methodologies with confidence in such operating regimes.

The overarching goal of this thesis is to develop a simulation framework capable of accurately reproducing the combustion behaviour of hydrogen ignited by a diesel pilot injection. This enables the evaluation of how different injection strategies, pilot quantities, and modelling assumptions influence performance, efficiency, and emissions.

Hydrogen's strong diffusivity, fast flame speeds, and high auto-ignition temperature make the combustion process highly sensitive to the local equivalence ratio distribution created by both the hydrogen and diesel injections. For this reason, injector modelling becomes a prerequisite for developing a physically reliable combustion model.

Modelling Strategy

The modelling strategy adopted in this thesis is summarised below, reflecting conclusions drawn from the literature review and the physical requirements of dual-fuel combustion modelling:

- The high autoignition temperature and strong diffusivity of hydrogen, combined with the need to resolve NO_x emissions, justify the use of a detailed chemistry model. Two combustion models will be tested: the Turbulent Flame Speed Closure (TFSC) and the Laminar Flame Concept (LFC). TFSC relies on precomputed tables for the local flame speed (LFS) and modeling of the turbulent flame speed, making it more computationally efficient, while LFC calculates the flame dynamically at each iteration, potentially offering greater physical accuracy, especially in highly unsteady or stratified conditions.
- The RNG k–ε turbulence model is selected as a starting point, building on its successful application in similar engine simulations and agreement with experimental velocity fields. Nonetheless, if the model is changed and features like the injector or valve are included in the geometry, alternatives such as the k–ω model may be evaluated.
- The dual-fuel injection system, comprising a small diesel pilot and a high-pressure hydrogen pulse, introduces significant complexity. Instead of modeling the full injector geometry, a variable mass flow rate profile as a function of crank angle will be used to better capture the real injection dynamics. Should this approach yield insufficient accuracy, full injector modelling will be considered as a backup strategy, following prior work by Antonacci, albeit at higher computational cost.
- Mesh resolution and time-step sensitivity will be critical, especially to capture the steep gradients introduced by hydrogen's high diffusivity and fast flame speeds. A dedicated phase will be allocated to mesh development and sensitivity testing to ensure physical fidelity in the simulations.
- Regarding the chemical reaction mechanism, the Gustavsson n-heptane model [27] will be used initially for diesel combustion, as it has been consistently employed in previous dual-fuel studies and offers reliable performance. Although preliminary analyses suggest that adding a full hydrogen mechanism does not drastically change global results, it is acknowledged that a dedicated hydrogen–diesel combined mechanism could improve prediction accuracy. At present, no fully validated mechanism is available for direct implementation in STAR-CCM+, but such an enhancement remains an open possibility for future work or sensitivity testing.

Scope and Research Questions

The scope of this work is the development of a CFD model capable of accurately describing both the combustion in a hydrogen–diesel dual-fuel compression ignition engine.

Based on the literature review, the following research questions have been formulated:

1. How can a CFD model be developed and validated against experimental data to accurately describe both the combustion and injection processes in a hydrogen–diesel dual-fuel CI engine?
2. Which combinations of turbulence models, combustion models, and chemical kinetic mechanisms yield the most physically accurate and computationally robust representation of combustion under these conditions?
3. What is the most appropriate and reliable method for modelling hydrogen injection?
4. What is the minimum quantity of diesel pilot required to successfully initiate combustion, with the objective of reducing diesel usage to minimize carbon emissions?

Chapter 2

Methodology

2.1 Experimental Setup

The experimental campaign was carried out in 2023 on a heavy-duty compression ignition engine operating with dual-fuel combustion, using hydrogen as the main fuel and a small diesel pilot for ignition. Engine tests were performed under different load conditions, defined based on a desired torque and horsepower target, at various engine speeds, and across a range of start of injection (SOI) timings and injection durations. Although the main purpose of the tests was to explore the engine's performance under different conditions, the recorded data can also be used to support the validation of CFD models. Special attention is given to the comparison of injection rate curves, injected quantities, in-cylinder pressure evolution, apparent heat release rates, and overall combustion behavior, with the aim of improving the predictive capabilities of the simulation framework for this engine concept.

2.1.1 Test Engine and Facility Description

The experiments were conducted on a six-cylinder Scania heavy-duty compression ignition engine operating at 1200 RPM. The main geometric specifications of the engine are summarized in Table 2.1.

Table 2.1: Engine Specifications

Parameter	Value
Number of cylinders	6
Bore	130 mm
Stroke	160 mm
Connecting rod length	260 mm
Compression ratio	23:1
Engine speed	1200 RPM

The engine is equipped with a high-pressure dual-fuel injector developed by Westport Fuel Systems, capable of injecting both hydrogen and diesel through two independent needle systems. The injector features nine orifices, with radius of 0.05 mm and 0.338 mm, specifically designed to accommodate the drastically different physical properties of gaseous and liquid fuels.

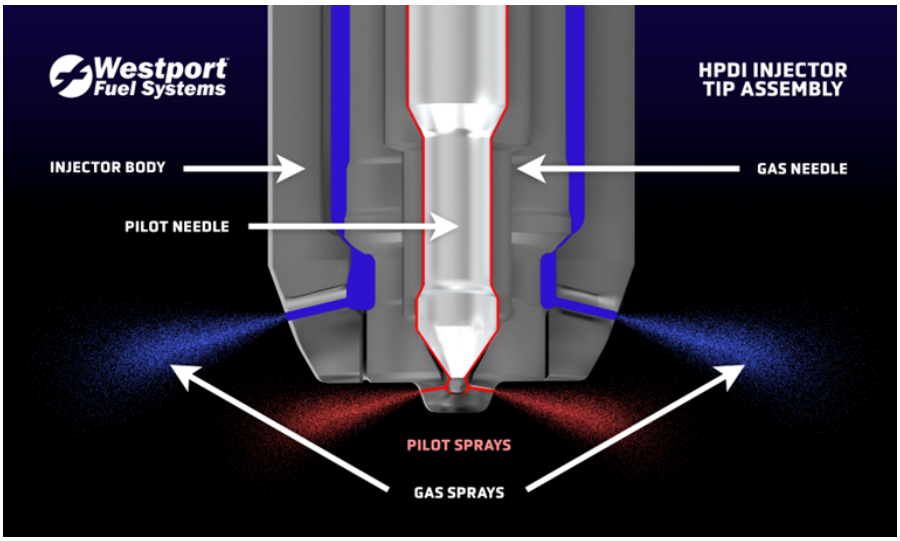

Figure 2.1: Westport Fuel Systems (Cespira) HPDI dual fuel injector

For the validation of the CFD model, the experimental results obtained in two different test cases performed at 1200 RPM and 75% load have been used. The reason why these cases were selected will be discussed in coming sections. These cases corresponds to a stable condition with reliable measurement data, including in-cylinder pressure traces and some injection parameters. The engine was operated using hydrogen as the main fuel and a small diesel pilot for ignition. The corresponding operating conditions are detailed in Table 2.2.

Table 2.2: Injection and Operating Conditions

Parameter	Unit	Case 1 A75	Case 5 560HP
Start of Injection (H_2, electric)	CAD BTDC	6.3	2.62
Start of Injection (diesel, electric)	CAD BTDC	11.33	8.63
H_2 mass per injection	mg	71.08	72.43
Diesel mass per injection	mg	5.88	6.16
Diesel injection on-time	µs	860	696
Hydrogen injection on-time	µs	1490	1337
Intake air mass per cylinder	mg	6560.2	4891.3
Hydrogen rail pressure	bar	302.5	299.2

It is important to note that a delay of approximately 3 crank angle degrees (CAD) exists between the electrical activation signal and the actual start of injection for both hydrogen and diesel fuels, due to injector response time.

2.1.2 Experimental Pressure Measurements

In-cylinder pressure is measured using piezoelectric sensors, these sensors only capture relative pressure changes, not absolute values. Therefore, a pegging procedure is required to shift the pressure trace to an absolute reference. This process involves determining an appropriate offset that aligns the pressure curve with known thermodynamic behavior during a part of the compression stroke where no combustion occurs.

In this study, an adiabatic compression is assumed in the interval between 620 CAD and 655 CAD. The specific heat ratio γ and the cylinder volume evolution $V(\theta)$ are obtained from CFD simulations. Assuming adiabatic compression:

$$\left(\frac{p_1'}{p_2'}\right) = \left(\frac{V_2}{V_1}\right)^{\gamma} \tag{2.1.1}$$

Given that the pressure sensor measures a shifted pressure $p_i' = p_i + p'$:

$$p_2 + p' = \left(\frac{V_1}{V_2}\right)^{\gamma} (p_1 + p') \tag{2.1.2}$$

Solving for the offset p', we obtain:

$$p' = \frac{p_1 \left(\frac{V_1}{V_2}\right)^{\gamma} - p_2}{1 - \left(\frac{V_1}{V_2}\right)^{\gamma}} \tag{2.1.3}$$

Where p_1, p_2 are the pressures at 620 CAD and 655 CAD, and V_1, V_2 are the corresponding cylinder volumes.

Once the offset is computed, it is added to the entire pressure trace for each cylinder, Figures 2.2 and 2.3 show the pressure curves derived from the experiment for Case 1 of the A75 dataset and Case 5 of the 560HP experiment respectively.

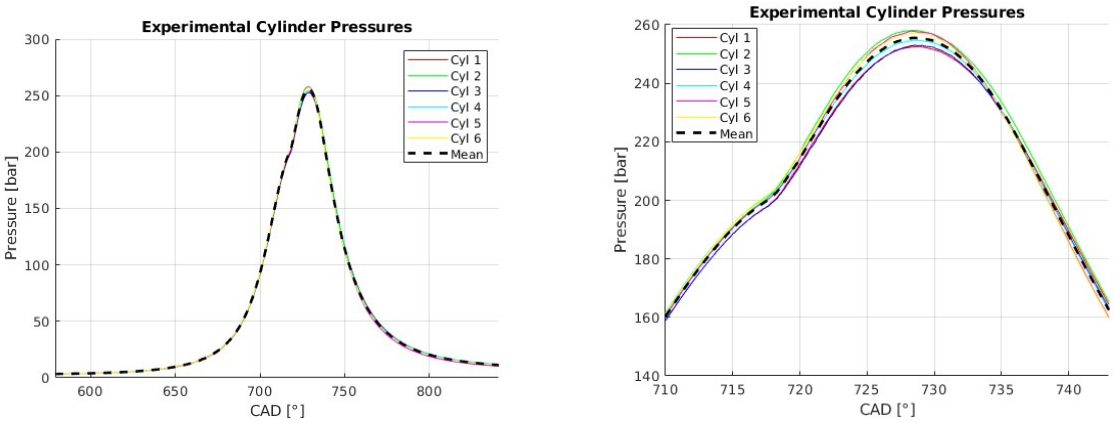

(a) 579 to 841 CAD. **(b)** 710 to 740 CAD.

Figure 2.2: Experimental pressure curves for all six cylinders and their average (Case 1 A75).

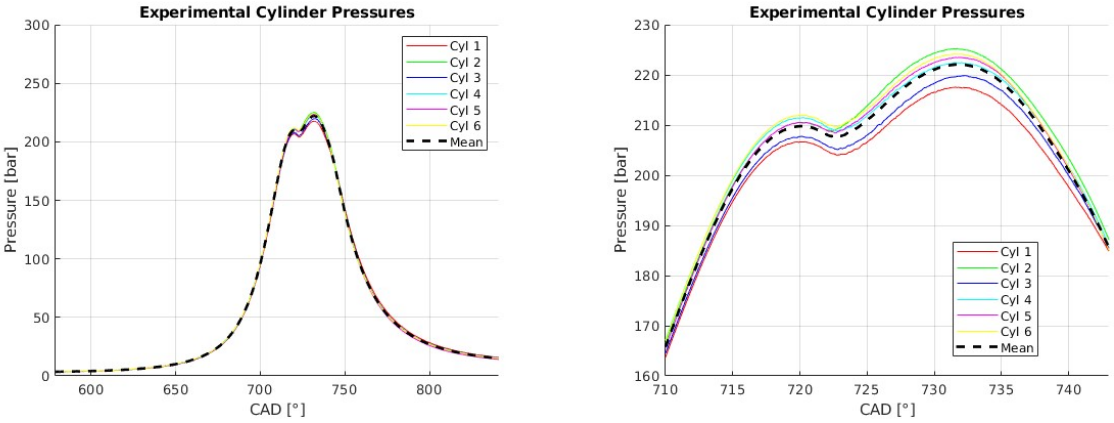

(a) 579 to 841 CAD. **(b)** 710 to 740 CAD.

Figure 2.3: Experimental pressure curves for all six cylinders and their average (Case 5 560HP).

2.1.3 Apparent Heat Release Rate Calculation

In this work, the heat release rate is always presented as the apparent heat release rate (aHRR), unless otherwise stated. It is important to distinguish this from the chemical heat release rate (cHRR). The cHRR is obtained in simulations directly from the combustion process, where the total heat release is directly calculated from the enthalpy changes associated with all ongoing chemical reactions. In contrast, the aHRR is obtained experimentally from in-cylinder pressure traces and provides a practical estimate of the rate of energy release during combustion. It is derived from the first law of thermodynamics for a closed system, under the common assumptions of negligible heat transfer and mass exchange:

$$\frac{dQ_{comb}}{d\theta} = \frac{\gamma}{\gamma - 1} p \frac{dV}{d\theta} + \frac{1}{\gamma - 1} V \frac{dp}{d\theta} \tag{2.1.4}$$

Where:

- θ is the crank angle,
- p is the pegged in-cylinder pressure,
- V is the instantaneous cylinder volume,
- γ is the specific heat ratio,

- The term $\frac{\gamma}{\gamma-1} p \frac{dV}{d\theta}$ represents compression work,
- The term $\frac{1}{\gamma-1} V \frac{dp}{d\theta}$ represents heat release.

Figures 2.4 and 2.5 represent the experimental apparent heat release rate of cases 1 and 2 respectively, derived from the previous pressure curves. Figure 2.6 shows the same results as the previous figure but after applying them a low pass filter (LPF) to reduce the noise of the signal.

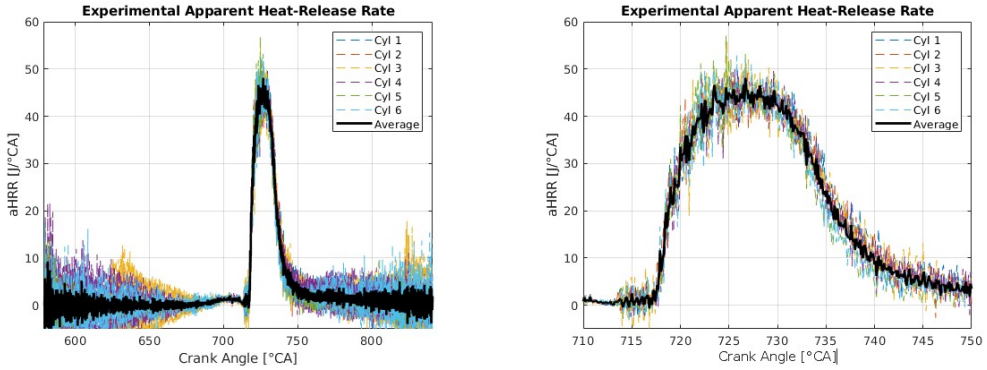

(a) 579 to 841 CAD. **(b)** 710 to 750 CAD.

Figure 2.4: Experimental Apparent Heat Release Rate curves (Case 1 A75).

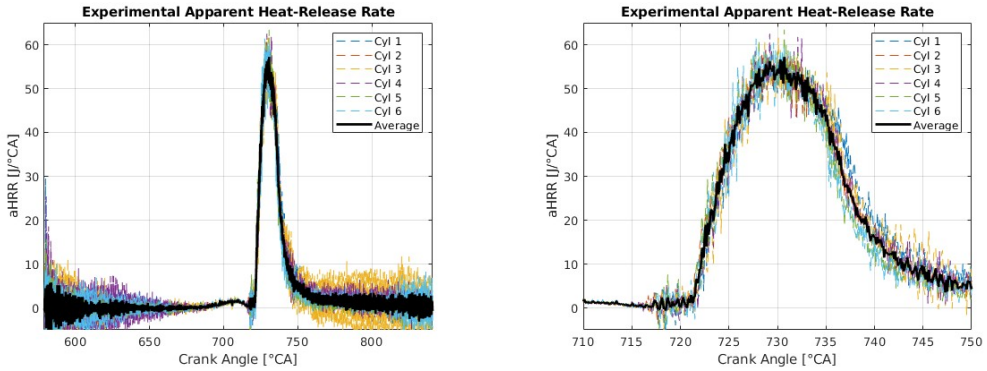

(a) 579 to 841 CAD. **(b)** 710 to 750 CAD.

Figure 2.5: Experimental Apparent Heat Release Rate curves (Case 5 560HP).

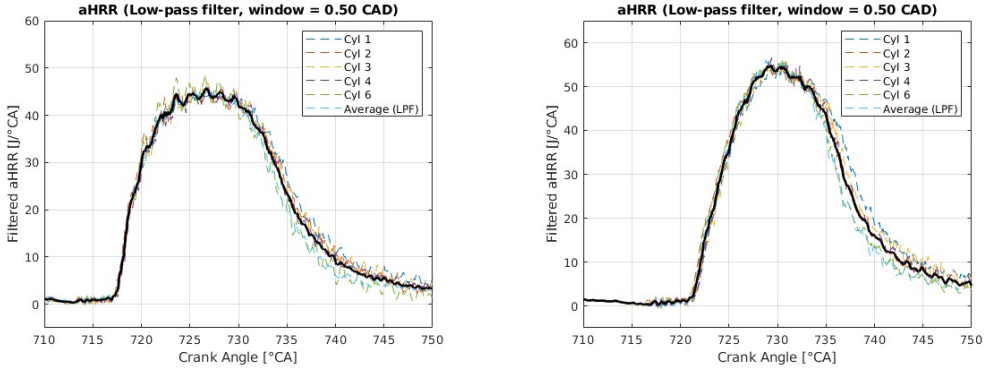

(a) Case 1 A75 **(b)** Case 5 560HP

Figure 2.6: Filtered apparent Cumulative Apparent Heat Release Rate curves.

Figures 2.7 and 2.8 represent the experimental cumulative heat release rate of both cases. It can be seen from these plots that there is considerable cylinder-to-cylinder variation. In particular, cylinder 5 appears to exhibit the largest deviation, which is especially evident in Case 1 (A75). It appears to have a lower Cumulative Heat Release Rate which could indicate that there is less fuel being injected in that cylinder. Despite these differences, the analysis will proceed using the average of all cylinders. However, it must be noted that this approach may introduce some level of error, since the cylinder-to-cylinder variability is not fully captured in the averaged representation.

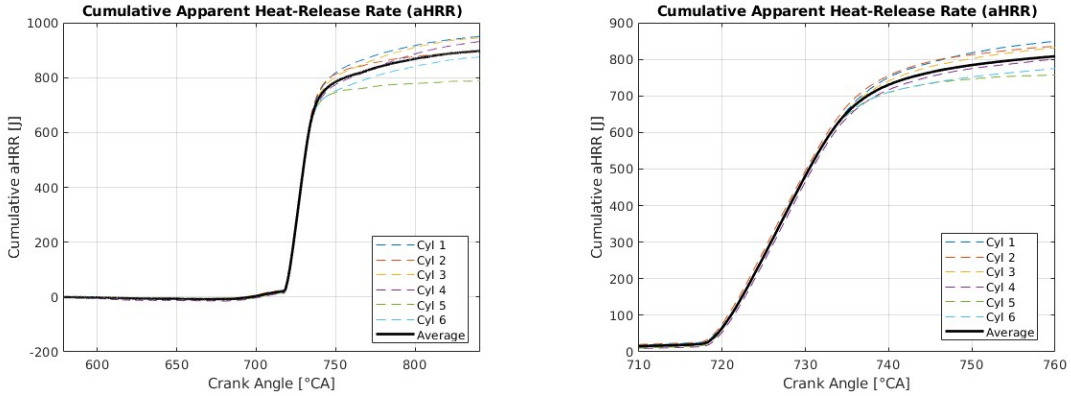

(a) 579 to 841 CAD. **(b)** 710 to 760 CAD.

Figure 2.7: Experimental Cumulative Apparent Heat Release Rate curves (Case 1 A75).

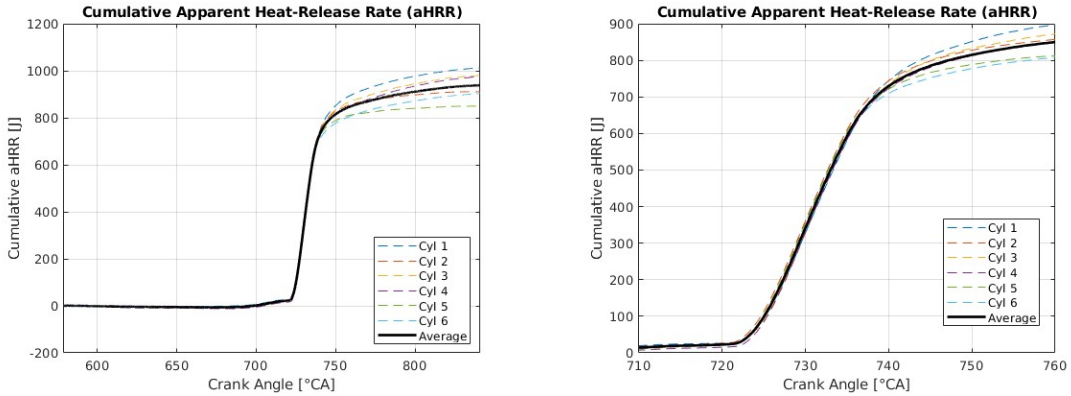

(a) 579 to 841 CAD. **(b)** 710 to 760 CAD.

Figure 2.8: Experimental Cumulative Apparent Heat Release Rate curves (Case 5 560HP).

2.1.4 Rationale for Case Selection

The experimental campaign at 75% load included a total of eight operating points within the A75 dataset. These cases exhibited very similar injection timings and combustion behavior, resulting in comparable in-cylinder pressure and apparent heat release rate (aHRR) curves. For this reason, only one representative case was retained for detailed analysis. Case 1 from the A75 dataset was selected as representative, since it was also employed in previous CFD studies with CONVERGE, which facilitates direct comparison with earlier work.

In contrast, the 560HP dataset only contains one case at at 75% of load at 1200 RPM (Case 5) which and displays a markedly different combustion behavior, mainly due to different injection timings. This difference is clearly visible when comparing the complete set of 75% load cases. Figures 2.9 and 2.10 show the in-cylinder pressure and aHRR traces for all nine cases (eight from A75 and one from 560HP). It can be observed that the A75 cases form a consistent cluster with only minor variations, while the

560HP case deviates significantly both in pressure evolution and in the shape and timing of the heat release rate.

Based on this observation, Case 5 from the 560HP dataset was selected in addition to Case 1 from A75. The inclusion of these two cases ensures that the CFD validation addresses not only a representative operating point, but also one that diverges from the typical trend, thereby providing a broader and more robust evaluation framework.

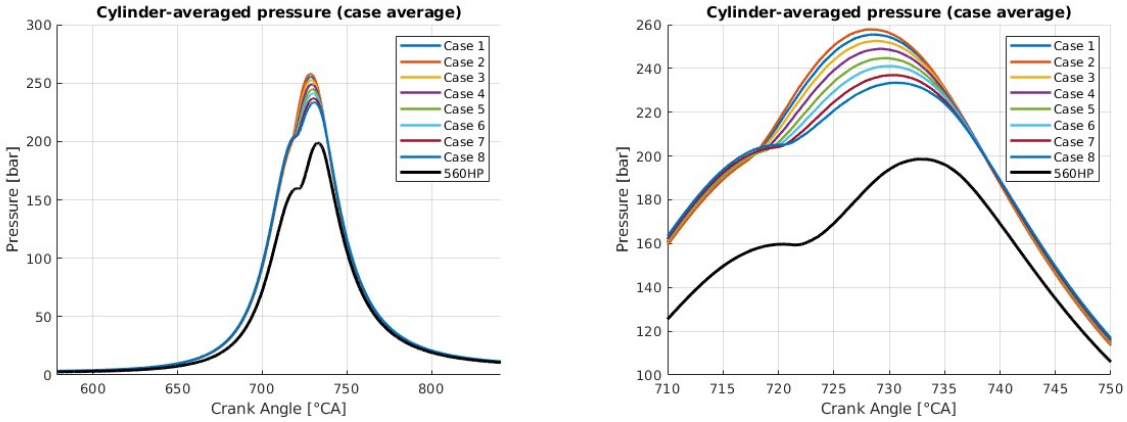

(a) 579 CAD to 841 CAD.

(b) 710 CAD to 750 CAD.

Figure 2.9: Comparison of in-cylinder pressure between the two 75% load cases.

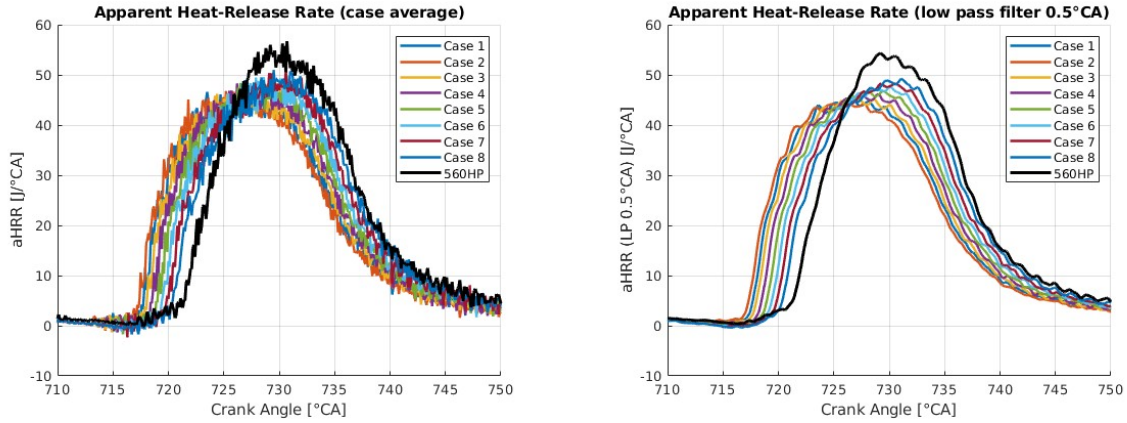

(a) Unfiltered signal.

(b) Filtered signal.

Figure 2.10: Comparison of aHRR between the two 75% load cases.

2.2 CFD Model Set Up

The CFD simulations were performed using the in-cylinder module of STAR-CCM+, focusing on a representative sector of the engine. A sector model was selected due to the periodic symmetry of the combustion chamber and injector configuration, allowing for reduced computational cost. The computational domain spans from 579 CAD to 841 CAD, corresponding to the period between intake valve closing (IVC) and exhaust valve opening (EVO). This interval ensures that the simulated sector remains physically accurate, as any valve overlap would invalidate the assumption of symmetry and the sector approach would not be representative of reality.

The chosen sector covers 40 degrees of the full 360-degree cylinder geometry, reflecting the periodicity imposed by the nine-hole injector design. Within the sector, both the hydrogen and diesel injectors are included, each featuring an angular offset of 10 degrees from the sector mid-plane. This results in a

total relative angular offset of 20 degrees between the two injectors, consistent with the actual engine layout.

Figures 2.11 and 2.12 illustrate the geometry of the simulation domain. The isometric view shows the full volume of the sector, while the top and side views provide a clearer depiction of the injector positions and orientation within the combustion chamber.

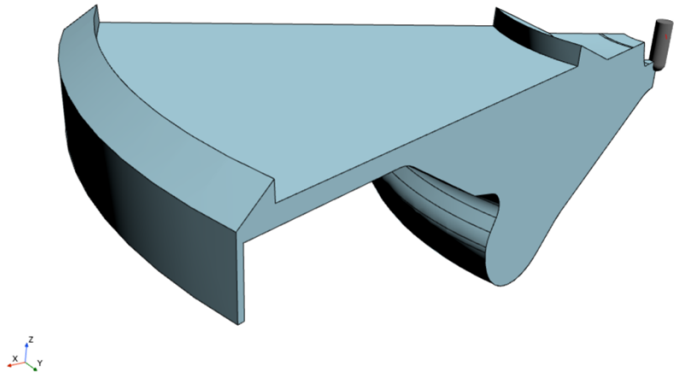

Figure 2.11: Isometric view of the CFD sector volume used in the simulations.

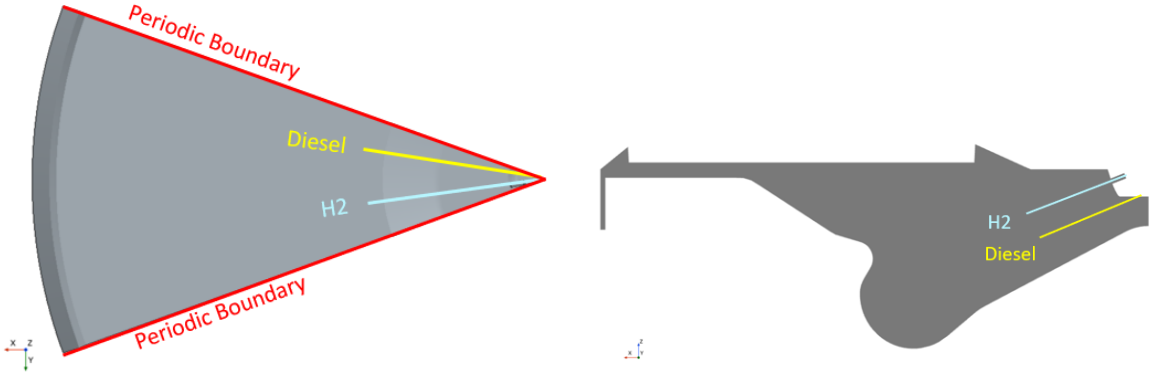

(a) Top view. **(b)** Side view.

Figure 2.12: Sector views with hydrogen and diesel injection directions.

2.2.1 Baseline CFD Model Configuration

In this section, the baseline simulation setup for Case 1 is presented. The objective of this baseline case is not to produce final or directly relevant results, but rather to provide an initial reference framework for subsequent analyses, including the mesh sensitivity study and the assessment of connecting rod stiffness effects. At this early stage of the project, the baseline simulation serves as a practical starting point to evaluate modeling strategies and establish consistent boundary conditions.

Injection Mass Flow Profiles

The injection mass flow rate curves for hydrogen and diesel used in the baseline simulation were generated from the operating conditions summarized in Table 2.2. Knowing the start of injection and injection duration (converted into crank angle degrees), a simplified profile was constructed by assuming an idealized symmetric opening and closing of the injector. No nozzle flow theory, needle dynamics, or internal injector effects were considered at this stage. The only constraint applied was that the total injected mass equals the target values of 71.08 mg for H_2 and 5.88 mg for diesel.

The resulting curves, shown in Figure 2.13, therefore represent a rough estimation of how the injection event might look under the given timings. While not physically accurate, these profiles provide a convenient approximation for early analyses such as the mesh sensitivity study and the evaluation of connecting rod stiffness, without requiring detailed injector modeling.

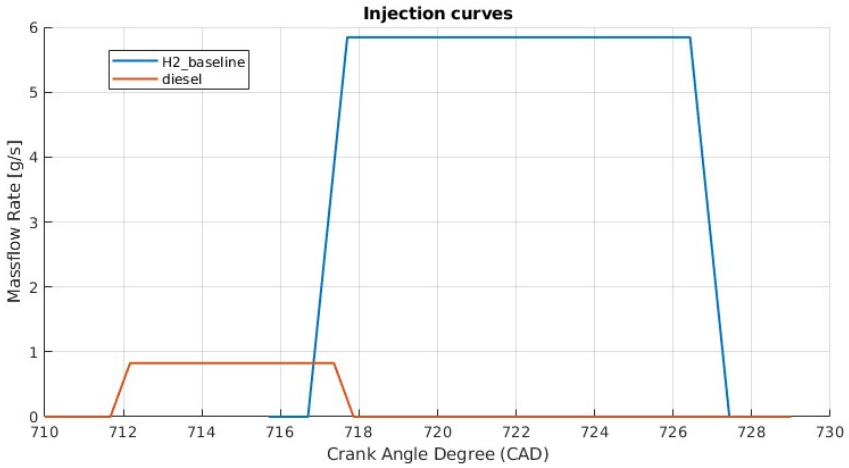

Figure 2.13: Simplified injection mass flow profiles used in the baseline simulations for diesel and hydrogen.

This simplified representation provides the initial baseline for the CFD analysis. Given its idealized nature, deviations from experimental behavior are expected, particularly during the combustion phases. In later stages of the project, more realistic injection profiles will be implemented, incorporating nozzle flow theory and gradual needle dynamics, in order to more accurately reproduce the actual injection and combustion processes.

Physical Models and Baseline CFD Setup

Following the definition of the simplified injection profiles, the next step is to establish the physical submodels required for the baseline simulations. The purpose of this setup is not to deliver final predictive results, but to provide a consistent framework for evaluating mesh sensitivity and structural effects, while ensuring that the main physical processes of dual-fuel hydrogen–diesel combustion are represented in a reasonable manner.

The simulation incorporates a set of physical submodels selected based on the conclusions drawn from the literature review. These choices align both with Scania's internal modeling practices and with the approaches considered most appropriate for capturing dual-fuel hydrogen–diesel combustion in internal combustion engines. A summary of the models included in this baseline setup is provided in Table 2.3.

Table 2.3: Summary of physical models used in the baseline CFD simulations.

Model Type	Model or Setting
Turbulence Model	RNG k–ε
Combustion Model	Complex Chemistry
Flame Speed Model	Turbulent Flame Speed Closure (TFSC)
Laminar Flame Speed	Siemens H2 Laminar Flame Speed Table
Turbulent Flame Speed	Zimont model
Reaction Mechanism	Gustavsson n-heptane mechanism
Diesel Atomization Model	Huh Atomization
Diesel Spray Breakup Model	Reitz-Diwakar model
Equation of State	Redlich-Kwong real gas model
Molecular Diffusivity	Kinetic Theory
Thermal Conductivity	Mathur-Saxena
Turbulent Schmidt Number (Sc_t)	0.9 (default)
Turbulent Prandtl Number (Pr_t)	0.9 (default)
Exhaust Gas Recirculation (EGR)	0.0%
Swirl	1.67 (2000 rpm)

The turbulence field is resolved using the RNG k–ε model, which has previously shown reliable results for both diesel and hydrogen applications. Combustion is modeled using the Complex Chemistry framework, with flame propagation captured through the Turbulent Flame Speed Closure (TFSC) model based on a precomputed table made by Siemens to represent the H2 laminar flame speed and the Zimont correlation for turbulent flame speed.

Regarding the reaction mechanism, the present simulations employ the n-heptane mechanism developed by Gustavsson et al. [27], a validated surrogate for diesel combustion that is widely used at Scania. This mechanism also includes a simplified hydrogen sub-mechanism, which allows its application in dual-fuel contexts. Further developments aimed at improving the coupling between diesel and hydrogen reaction chemistry are ongoing research at Lund University of Technology and University of Sydney, but these refinements lie beyond the scope of this thesis.

Fuel injection strategies differ between the two fuels. Diesel is modeled as a Lagrangian spray, with Huh atomization and Reitz-Diwakar breakup models to capture droplet evolution. In contrast, hydrogen is injected as a gaseous jet using the mass flow rate profiles derived earlier, without explicitly modeling the injector geometry.

The thermophysical properties of the gas mixture are modeled using the Redlich-Kwong real gas equation of state, while kinetic theory and the Mathur-Saxena correlation are used for molecular diffusivity and thermal conductivity, respectively. Both the Schmidt number and the turbulent Prandtl number are kept at its default value of 0.9.

With these physical models and boundary conditions defined, the baseline simulation setup is complete. The following subsection presents and discusses the results obtained from this initial configuration.

Baseline Model Results

The initial simulations were performed using the baseline configuration introduced in the previous section. Figure 2.14 presents a comparison between the simulated in-cylinder pressure trace and the corresponding experimental measurement. A clear mismatch can be observed across the entire crank angle range, with the largest deviations occurring in the vicinity of top dead center (TDC), where hydrogen combustion takes place.

To verify whether the mismatch originates from inaccurate initial conditions, a closer comparison is shown in Figure 2.14b, which displays the pressure evolution during the early compression phase. At the beginning of the interval, from 579 CAD to 609 CAD, the simulated pressure matches the experimental value almost exactly. However, as the piston continues to compress the mixture, a small

but growing deviation becomes evident. This suggests that the initial pressure conditions are correct, however, the mismatch arises during the compression stroke, before the start of combustion.

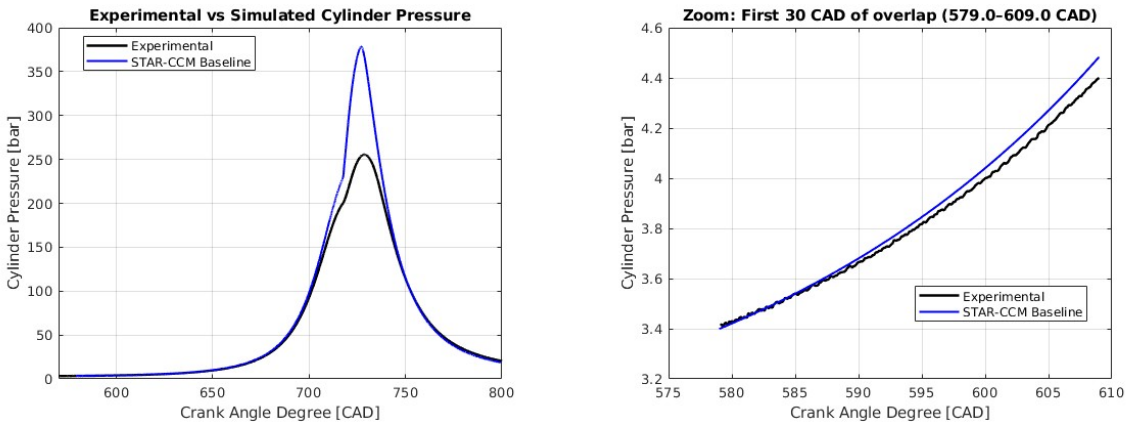

(a) 570 CAD to 800 CAD.

(b) 579 CAD to 609 CAD.

Figure 2.14: Comparison between simulated and experimental in-cylinder pressure in the baseline configuration.

These results will be used as a reference in the following sections where the mesh generation strategy and the effect of connecting rod stiffness on the in-cylinder pressure trace is examined, as this structural aspect has been identified as a potential cause for the mismatch prior to combustion.

2.2.2 Meshing

The computational mesh for the CFD simulations was generated using the Internal Combustion Engine (ICE) module of STAR-CCM+, which is specifically designed for modeling transient processes in four-stroke engines. This strategy is essential to capture the moving boundaries and steep gradients in pressure, temperature, and species concentrations that characterize internal combustion phenomena.

The ICE module first constructs a 2D base mesh, which is then splined in the azimuthal direction to generate the full 3D computational domain. The resulting mesh is composed primarily of structured hexahedral cells. To accommodate piston motion, the software automatically performs remeshing during the compression and expansion strokes, thereby preventing excessive cell distortion and preserving numerical accuracy. Figures 2.15, 2.16, and 2.17 illustrate the mesh at 579 CAD, 720 CAD, and a top view of the computational sector.

In addition to this automatic remeshing, two manual refinements were implemented:

- **Conical refinement (710-760 CAD):** applied during the main combustion phases to improve resolution where sharp gradients in temperature and pressure occur.
- **Cylindrical refinement (715-745 CAD):** focused on the hydrogen injection window to better capture transient jet development and mixing.

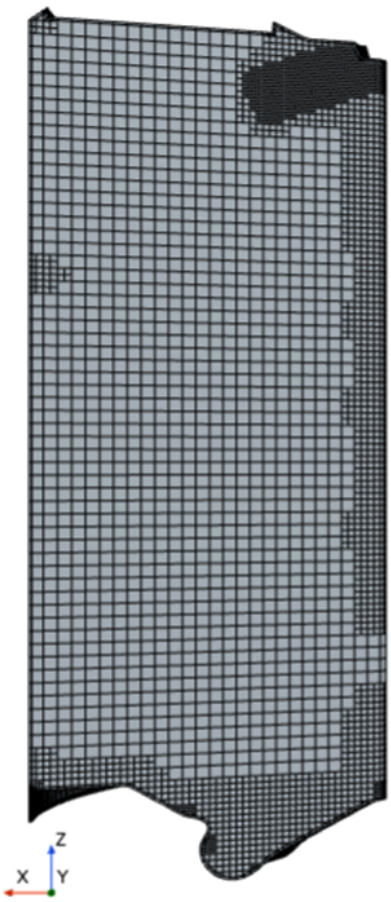

Figure 2.15: Mesh at 579 CAD.

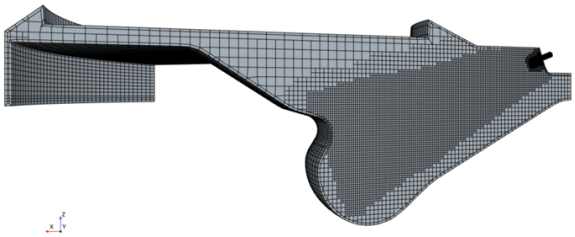

Figure 2.16: Mesh at 720 CAD.

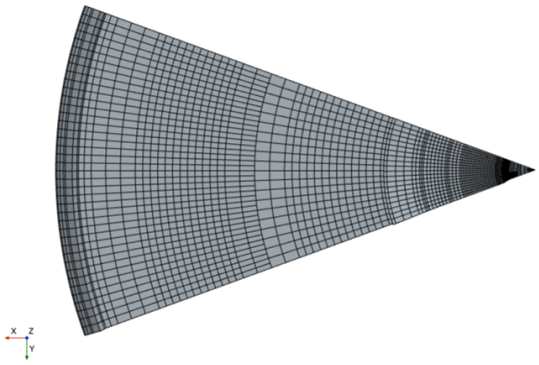

Figure 2.17: Top view of the mesh.

The main regions of interest can be described as follows:

- **Cylinder Region:** The cylinder sector forms the core of the computational domain, where the mesh continuously adapts to piston displacement. Automatic remeshing ensures stable cell quality throughout compression and expansion, while refinements in this region improve the resolution of combustion and injection events.
- **Diesel Injector:** The diesel injector simulation is already included in the definition of STAR-CCM + ICE sector, and therefore it has a mesh refinement which is automatically integrated into the mesh. However, as previously mentioned, two user-defined localized refinements have been included around the diesel and hydrogen injectors regions to control the mesh in the area where injections and combustion will take place.
- **Gas Injector (Hydrogen):** Unlike the diesel injector, the hydrogen injector is not part of the default ICE sector. It was therefore modeled as a separate region with a dedicated mesh. As shown in Figure 2.18, a directed mesh technique was applied to achieve high resolution near the injector holes, enabling a more accurate representation of jet penetration and hydrogen–air mixing.

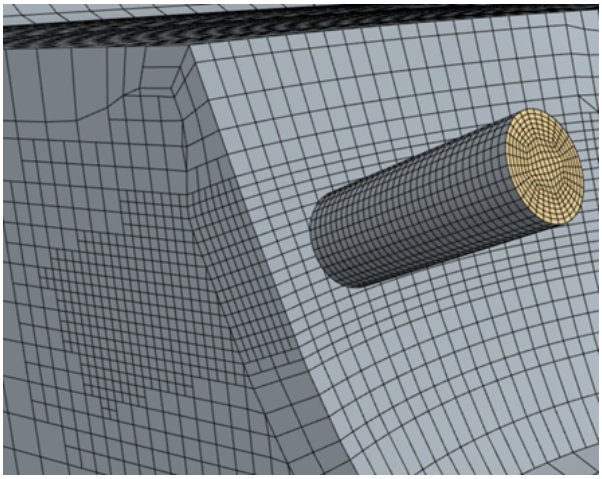

Figure 2.18: Mesh in the hydrogen injector.

Figure 2.18 alos displays some limitations of the meshing strategy that must also be acknowledged:

- **Prism layer around the cylinder walls:** The ICE template automatically generates a prism layer adjacent to the cylinder walls to resolve near-wall flow. While appropriate for wall-bounded flows, this layer cannot be locally deactivated in regions where additional geometries (e.g., the hydrogen injector) are introduced. This requires carefully adjusting the prism layer thickness to ensure a smooth transition between injector and cylinder meshes. If not handled properly, excessive numerical diffusion may occur, potentially distorting the hydrogen jet and affecting mixing predictions.
- **Global prism layer settings:** Since the prism layer cannot be tuned locally, the adjustments made for the injector region must also be applied throughout the cylinder. This constrains the overall mesh design, as the injector requirements dominate the prism layer setup.
- **Two-dimensional refinements only:** Refinements in STAR-CCM+ are restricted to 2D definitions extruded across the entire azimuthal sector. As a result, refinements intended for the hydrogen injector extend across the full 40 degree sector, rather than being localized. This leads to unnecessary over-refinement in some areas and an increased computational cost.

Mesh sensitivity analysis

A mesh sensitivity study was conducted to evaluate the impact of mesh resolution on solution accuracy and computational cost using 200 cores in the Scania cluster. Four mesh configurations were tested, as summarized in Tables 2.4 and 2.5. The base cell size for the cylinder mesh was varied from 5 mm to 0.5 mm, with corresponding adjustments to the number of azimuthal layers, the prism layer thickness and local refinement levels. As expected, finer meshes resulted in significantly larger cell counts and longer runtimes. For instance, the 0.5 mm mesh contained over 2 million cells at top dead center (TDC) and experienced divergence problems when running under the same conditions as the other simulations.

The numerical stability of the simulations can be evaluated using the convective Courant number CFL, defined as:

$$CFL = \frac{u\,\Delta t}{\Delta x} \tag{2.2.1}$$

where u is the local flow velocity, Δt is the time step, and Δx is the local cell size. Values of CFL significantly greater than unity typically indicate a risk of numerical instability.

Figure 2.19 illustrates the convective Courant number for the baseline 0.5 mm mesh, at one time step before the simulation diverged. The values reached are considerably high, confirming that the

divergence was driven by an excessive Courant number. In principle, this issue could be mitigated by reducing the simulation time step. However, as already reflected in Table 2.4, the computational cost is substantial, and further reduction of the time step would make the simulation impractically slow. Therefore, it was considered that additional attempts to stabilize this mesh would not provide sufficient benefit to justify the increased cost.

Table 2.4: General mesh parameters and computational cost.

Base Cell Size	Azimuthal Layers	Initial Cells	TDC Cells	Simulation Time
5 mm	20	38,623	22,235	11:03:28
2.5 mm	40	104,817	122,784	11:21:28
1 mm	80	902,335	501,292	18:49:04
0.5 mm	80	3,678,844	2,082,175	–

Table 2.5: Cell layer and refinement resolution per mesh configuration.

Base Cell Size	Prism Layer Size	Minimum Refinement Cell Size
5 mm	1 mm	0.2 mm
2.5 mm	0.5 mm	0.1 mm
1 mm	0.25 mm	0.05 mm
0.5 mm	0.125 mm	0.025 mm

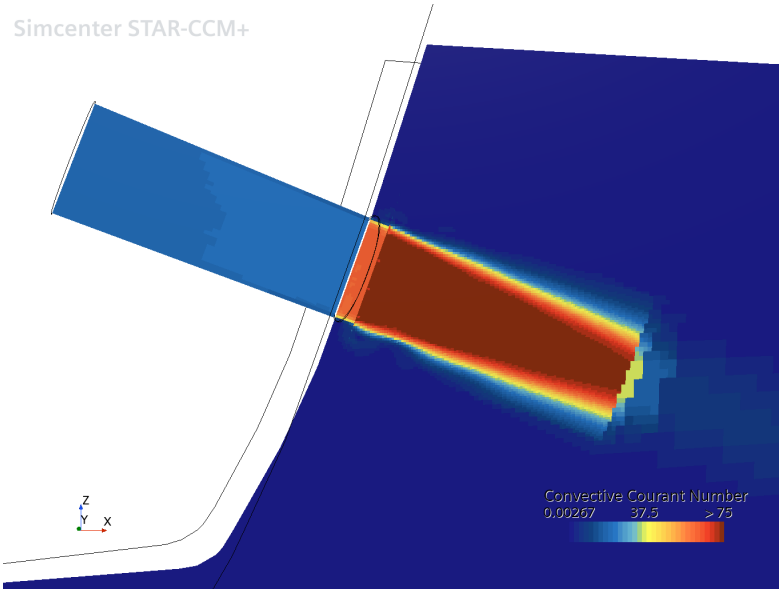

Figure 2.19: Convective Courant number distribution for the baseline 0.5 mm mesh, one time step before divergence.

Figure 2.20 shows the pressure traces for each mesh configuration. Despite the variation in mesh resolution, the predicted pressure curves converge toward a common solution, which indicates that the solution is approaching mesh independence. Although the 1 mm mesh exhibits slightly improved resolution of pressure rise and peak, the differences compared to the 2.5 mm mesh are approximately 1% at peak pressure. For the highly detailed analyses the finer mesh may be used selectively. However, for most parametric studies, the 2.5 mm mesh provides sufficient fidelity. Therefore, the 2.5 mm base mesh was selected for further simulations. This configuration strikes a good balance between resolution and computational time, with a TDC cell count of approximately 123,000 and a runtime of around 11 hours per cycle. Notably, this mesh is fine enough to capture the key features of the in-cylinder flow and injection dynamics, while remaining within practical limits for iterative case studies.

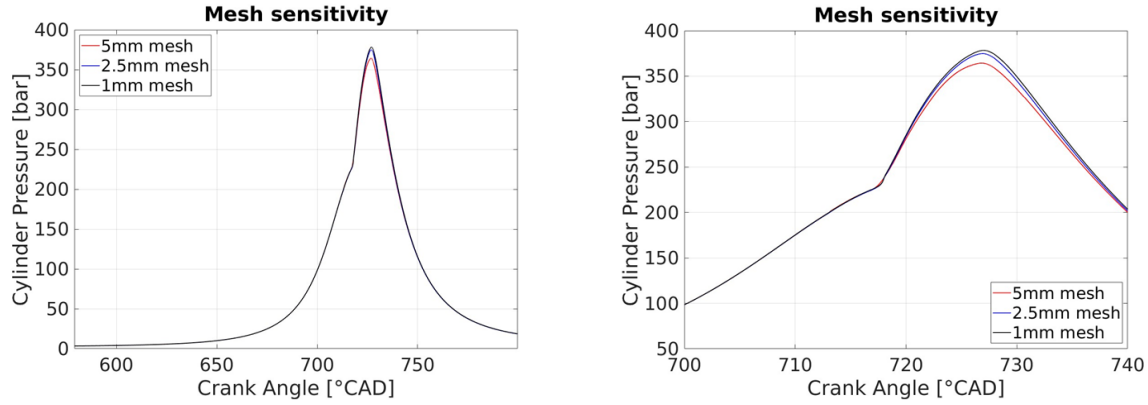

(a) 579 CAD to 780 CAD.

(b) 710 CAD to 740 CAD.

Figure 2.20: Pressure curves for different mesh values.

2.2.3 Connecting Rod Stiffness Corrections

To investigate the pressure overprediction observed during compression stroke in the baseline case, a simulation was performed introducing a field function to account for the deformation of the connecting rod. This approach modifies the trajectory of the piston to better reflect the mechanical behavior of the engine under load, thus adjusting the effective compression ratio and the evolution of the in-cylinder pressure. The piston displacement in the Z direction was redefined using the following expression:

$$Z_{\text{piston}} = Z_0 + R \cdot \cos(\theta) + L \cdot \sqrt{1 - \left(\frac{R \cdot \sin(\theta) + \varepsilon}{L}\right)^2} - \sqrt{(L+R)^2 - \varepsilon^2} - \delta \tag{2.2.2}$$

where:

- Z_0: piston position offset,
- R: crank radius,
- θ: crank angle,
- L: connecting rod length,
- ε: pin offset,
- δ: piston deflection due to rod deformation.

The final term δ introduces an elastic correction to the piston motion caused by the axial force on the connecting rod. It is estimated based on the pressure difference across the piston crown and the axial stiffness of the rod, using:

$$\delta = \frac{F}{k} \tag{2.2.3}$$

where F is the net pressure force acting on the piston, and k is the axial stiffness of the connecting rod. The pressure force is defined as:

$$F = (p_{\text{cylinder}} - p_{\text{crankcase}}) \cdot A_{\text{piston}} \tag{2.2.4}$$

Substituting into the previous equation, the deflection becomes:

$$\delta = \frac{(p_{\text{cylinder}} - p_{\text{crankcase}}) \cdot A_{\text{piston}}}{k} \tag{2.2.5}$$

Figure 2.21 shows the effect of this modification, comparing the original baseline simulation, the corrected version, and the experimental pressure data. As shown in Figure 2.21a, the corrected simulation now matches the experimental pressure evolution very closely during the entire compression phase, even throughout the diesel injection event as it can be seen on Figure 2.21b. This confirms that the deviation observed in the original baseline configuration was indeed caused by the overestimation of effective compression due to the rigid connecting rod assumption.

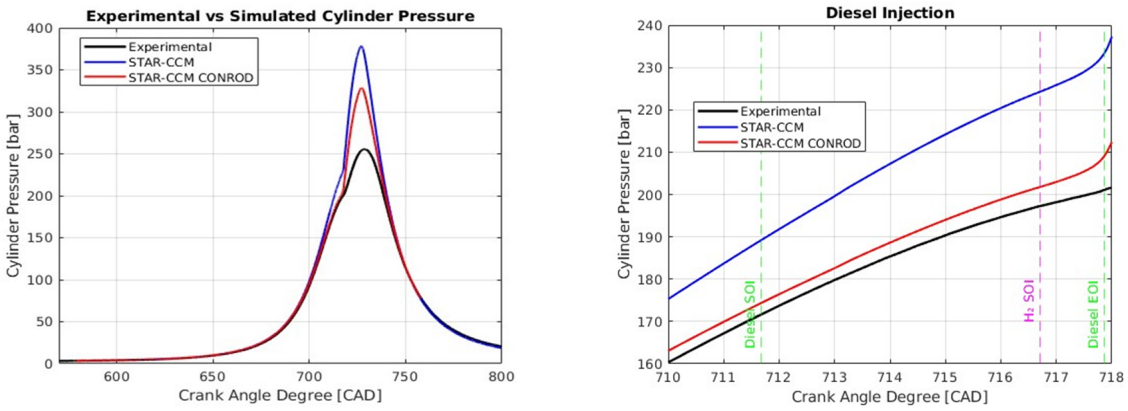

(a) 570 CAD to 800 CAD.

(b) 710 CAD to 718 CAD.

Figure 2.21: Comparison between simulated pressure curves with and without connecting rod stiffness.

The pressure traces of the original and corrected simulations remain virtually identical up to the onset of hydrogen ignition at 717–718 CAD. Throughout the compression stroke, including the diesel injection and pilot combustion phases, the corrected case shows excellent agreement with the experimental data, with deviations remaining below 2%. This indicates that the pilot injection and combustion are well captured with the current setup, and that the dominant source of error in the baseline model arose from the rigid connecting rod assumption. After correcting for rod deformation, the remaining discrepancies are confined to the hydrogen combustion phase, confirming that the pressure mismatch is now primarily linked to the modeling of hydrogen injection and ignition.

2.3 Nozzle modeling

As discussed in the introduction, High-Pressure Direct Injection (HPDI) offers efficiency advantages, making it an attractive option for heavy-duty and industrial engine applications. However, implementing HPDI with hydrogen introduces significant challenges because of the physical properties of the fuel. Unlike conventional carbon-based fuels, such as diesel, which are injected in liquid form, hydrogen at ambient temperature is injected as a gas. This fundamental difference has a profound impact on the behavior of the injection process and its modeling.

In traditional diesel injection, the flow through the injector orifices is often assumed to be constant during the injection event. This assumption is valid because diesel is injected at very high pressures (typically around 1000 bar), which are approximately an order of magnitude higher than the in-cylinder pressures during injection (usually from 100 to 300 bar). Additionally, since diesel is injected as a liquid, it can be approximated as an incompressible flow. As a result, the mass flow rate is primarily governed by the pressure drop and the geometry of the orifice, and it can reasonably be approximated as constant throughout the injection event, especially considering the short duration of injection.

In contrast, hydrogen injection in HPDI systems cannot rely on the same simplifications. Hydrogen is injected gaseously at a rail pressure of approximately 300 bar, and being a low density compressible gas, its behavior is fundamentally different. The mass flow rate is no longer solely governed by the pressure differential and nozzle geometry, but also by the compressibility of the gas and the flow regime at the nozzle exit.

Since the injector is not explicitly included in the CFD domain, its behavior must be represented through simplified theoretical models. For this purpose, the following section introduces the nozzle flow theory, considering both the convergent and the convergent–divergent nozzle theory formulations as possible approaches to describe the mass flow rate through the injector.

2.3.1 Convergent Nozzle theory

When analyzing compressible gas flows, it is essential to distinguish between different flow regimes depending on the ratio between the local flow velocity and the speed of sound. This ratio is known as the Mach number M, defined as:

$$M = \frac{u}{a} \tag{2.3.1}$$

where u is the local flow velocity and a is the local speed of sound.

The Mach number classifies the flow regime as follows:

- **Subsonic** ($M < 1$): flow velocity is lower than the speed of sound. Pressure disturbances can travel both upstream and downstream, so the flow is influenced by both boundary conditions.
- **Sonic** ($M = 1$): flow velocity equals the speed of sound. This is known as the critical condition, beyond which downstream pressure no longer influences the upstream flow.
- **Supersonic** ($M > 1$): flow velocity exceeds the speed of sound. Information only propagates downstream. This regime requires divergent nozzle geometries and does not apply to the current context.

The transition between the subsonic and sonic regimes is governed by the ratio between downstream pressure p_d and upstream (stagnation) pressure p_0. For a given gas, there exists a critical pressure ratio below which the flow reaches sonic velocity at the nozzle hole. When this happens the downstream pressure has no longer influences in the incoming flow, and the massflow through the orifice becomes consta;t, this effect is known as choking. The threshold between subsonic and sonic conditions is given by the critical pressure ratio ($\gamma = 1.4$):

$$\frac{p_{\text{crit}}}{p_0} = \left(\frac{2}{\gamma+1}\right)^{\frac{\gamma}{\gamma-1}} \approx 0.528 \quad \text{for hydrogen,} \tag{2.3.2}$$

which implies that for a rail pressure $p_0 = 300$ bar, choked flow only occurs if the in-cylinder pressure p_d remains below approximately 158 bar.

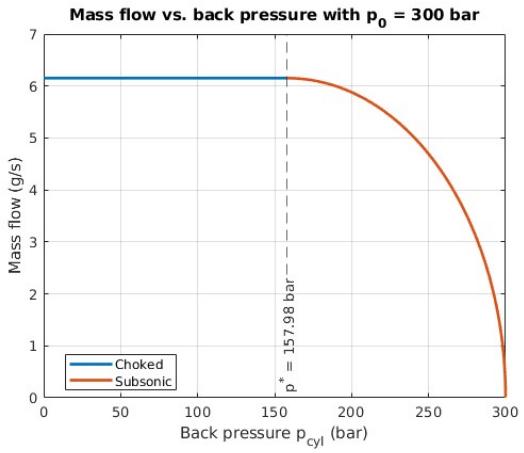

Figure 2.22: Mass flow behavior as a function of in-cylinder pressure for a rail pressure of 300 bar

In the case of Scania's HPDI operating conditions illustrated earlier, injection takes place while the in-cylinder pressure varies between 190 and 260 bar, therefore the critical ratio is not satisfied. As a result, according to the theory for convergent nozzles, the flow remains in the subsonic regime throughout the injection event.

Isentropic Flow Through a Convergent Nozzle: Subsonic Regime

In the subsonic regime, both the pressure and density at the nozzle exit depend on the Mach number and are governed by the isentropic relations:

$$\frac{p}{p_0} = \left(1 + \frac{\gamma - 1}{2} M^2\right)^{-\frac{\gamma}{\gamma - 1}}, \tag{2.3.3}$$

$$\frac{\rho}{\rho_0} = \left(1 + \frac{\gamma - 1}{2} M^2\right)^{-\frac{1}{\gamma - 1}} \tag{2.3.4}$$

$$\frac{T}{T_0} = \left(1 + \frac{\gamma - 1}{2} M^2\right)^{-1} \tag{2.3.5}$$

The corresponding mass flow rate per unit area is given by:

$$\frac{\dot{m}}{A} = \rho_0 \sqrt{\gamma R T_0} \cdot M \left(1 + \frac{\gamma - 1}{2} M^2\right)^{-\frac{\gamma + 1}{2(\gamma - 1)}} \tag{2.3.6}$$

This expression shows how the mass flow rate depends non-linearly on the downstream conditions. As the in-cylinder pressure rises during compression, the pressure ratio decreases, and so does the Mach number and corresponding mass flow rate.

Isentropic Flow Through a Convergent Nozzle: Sonic Regime (Choked Massflow)

If the in-cylinder pressure drops below the critical threshold defined in Eq. (2.3.2), the flow reaches sonic conditions at the nozzle throat. This is known as *choked flow*. In this regime, the mass flow rate becomes independent of downstream conditions, since pressure waves can no longer travel upstream to influence the flow.

Under choked conditions, the flow velocity at the throat reaches $M = 1$, and the mass flow rate per unit area reaches its maximum theoretical value. This is given by:

$$\left(\frac{\dot{m}}{A}\right)_{\text{max}} = \rho_0 \sqrt{\gamma R T_0} \left(\frac{2}{\gamma + 1}\right)^{\frac{\gamma + 1}{2(\gamma - 1)}} \tag{2.3.7}$$

This expression depends solely on upstream conditions: the total density ρ_0, temperature T_0, and specific gas properties γ and R. Since downstream pressure no longer affects the flow once it is choked, this regime provides a highly predictable and stable injection behavior with constant rates when the needle is open.

In practical terms, for hydrogen injected at 300 bar, choked flow would only occur if the in-cylinder pressure remains below approximately 157 bar. This condition might be satisfied during early injection, particularly when the piston is still rising in the compression stroke. However, it is no longer valid near Top Dead Center (TDC), where combustion chamber pressures often exceed 200 bar. This explains why certain injection profiles used in previous simulations which were carried out with the injection curves provided experimentally by Westport, exhibit a flat-top shape. All experiments that were provided to Scania with a rail pressure of approximately 300 bar have a downstream pressure equal to or lower than 140 bar.

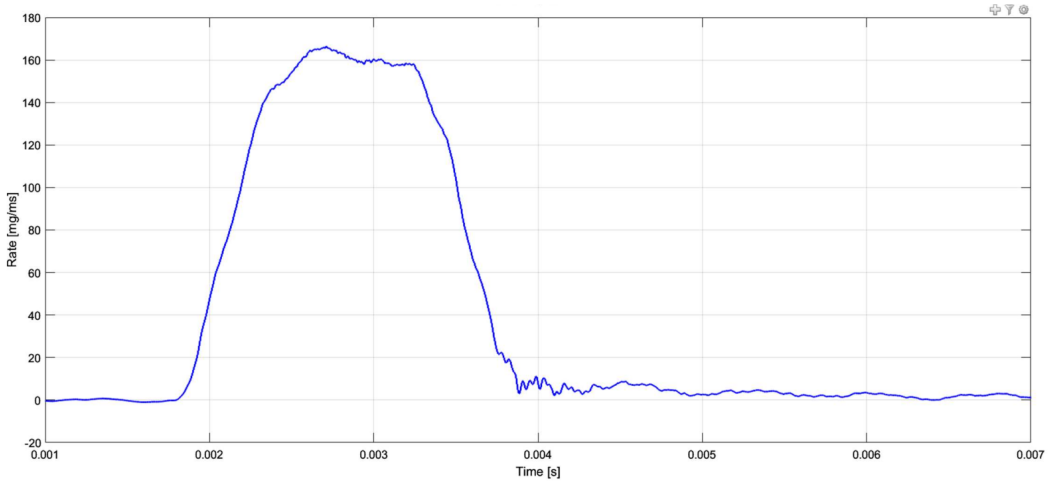

Figure 2.23: Injection curve given by Westport Fuel Systems for methane injections with a rail pressure of 300 bar and a constant back pressure of 140 bar.

Application of Convergent Nozzle Theory to Previous CFD Work

Figures 2.24 and 2.25 present the results of previous CFD studies performed at Scania with AVL FIRE, in which the full sector geometry, including an injector, was explicitly modeled. These simulations allow a direct comparison between cases with and without diesel pilot injection, and provide valuable insights into how the instantaneous in-cylinder pressure influences the hydrogen mass flow rate.

The misfire case (black curves in both figures), corresponding to hydrogen injection without a diesel pilot, exhibits a nearly flat-top mass flow rate throughout the injection event. This behavior is consistent with the prediction of choked flow described in Section 2.3.7, where the nozzle flow reaches sonic velocity and becomes independent of downstream conditions. In this case, the in-cylinder pressure remains only slightly above 160 bar, which is close to the critical pressure threshold derived in Eq. 2.3.2. Under these conditions, the flow can remain close to choked during most of the injection period, yielding a constant injection rate profile.

In contrast, the cases that include diesel combustion show a markedly different behavior. As seen in Figure 2.24, the hydrogen mass flow rate develops a pronounced dip in the middle portion of the injection event, deviating significantly from the flat-top profile. Simultaneously, the in-cylinder pressure rises sharply due to combustion, as illustrated in Figure 2.25, reaching values up to 290 bar for a rail pressure of 300 bar and even exceeding 300 bar for a rail pressure of 350 bar. Under these conditions, the pressure ratio across the nozzle no longer satisfies the critical condition, and the flow remains in the subsonic regime. As explained in Eq. 2.3.6, the mass flow rate then becomes highly sensitive to downstream pressure, decreasing as the in-cylinder pressure increases.

These results highlight that both flat-top and pressure-dependent injection profiles can be fully explained within the framework of compressible flow through convergent nozzles. The apparent discrepancy between the misfire and combustion cases does not imply inconsistencies in the simulations, but rather reflects the different operating regimes of the nozzle. When the in-cylinder pressure is sufficiently low, the flow chokes and the mass flow rate is constant. Conversely, when combustion elevates the in-cylinder pressure above the critical threshold, the mass flow rate decreases dynamically as a function of the instantaneous pressure ratio.

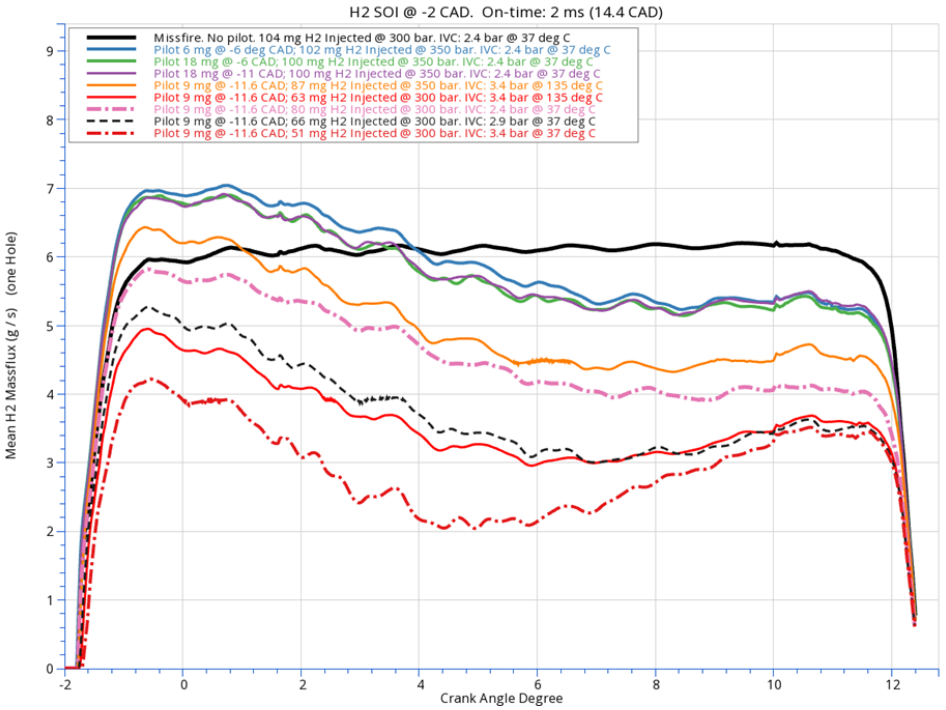

Figure 2.24: AVL Fire simulations: massflow results

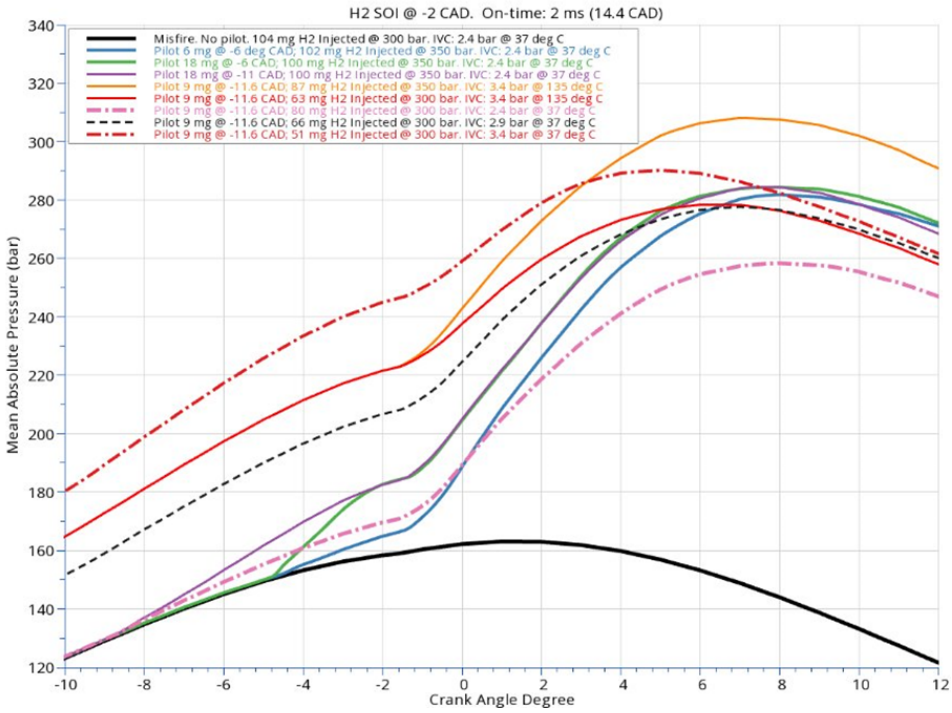

Figure 2.25: AVL Fire simulations: pressure results

2.3.2 Comparison between Convergent Nozzle Theory and 3 of the Previous Cases

To validate the theoretical framework described above, the isentropic flow equations were applied to three of the cases obtained from the AVL FIRE simulations reviewed previously. This includes the injector geometry, rail temperature (293K for case 2 and 393K for cases 1 and 3), a rail pressure of $p_0 = 300$ bar, and the instantaneous in-cylinder pressure for each case, shown in Figure 2.26.

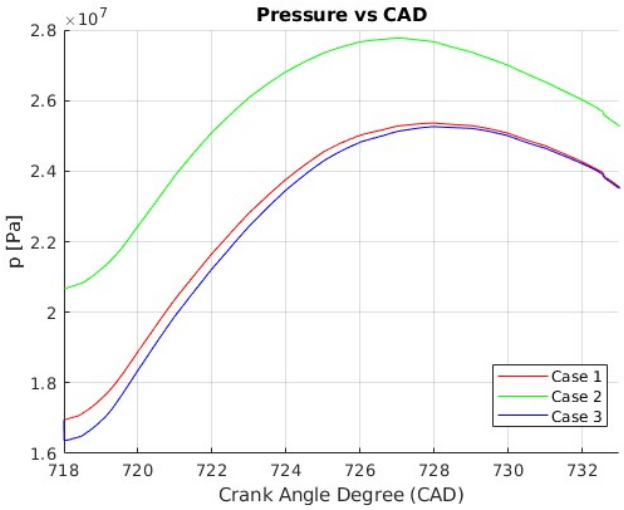

Figure 2.26: Instantaneous in-cylinder pressure traces for the three test cases.

The theoretical mass flow rate was computed using the isentropic relations previously explained. Figures 2.27 to 2.29 show the results of this comparison. The dashed lines represent the theoretical mass flow rate predicted by the isentropic model, while the solid lines correspond to the simulation results.

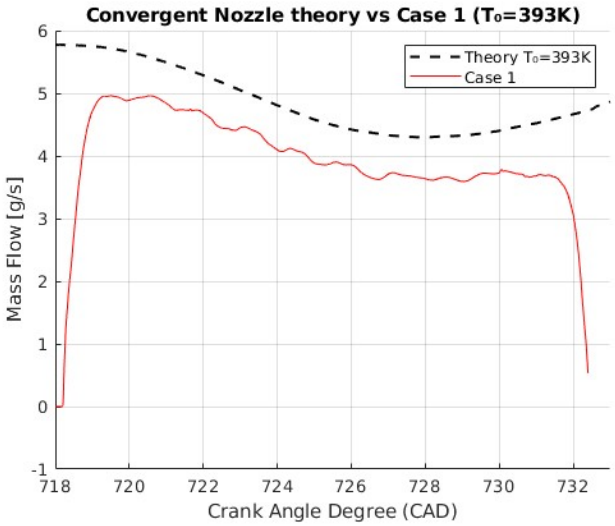

Figure 2.27: Case 1 ($T_0 = 393$ K). Comparison between the nozzle theory and CFD results (solid).

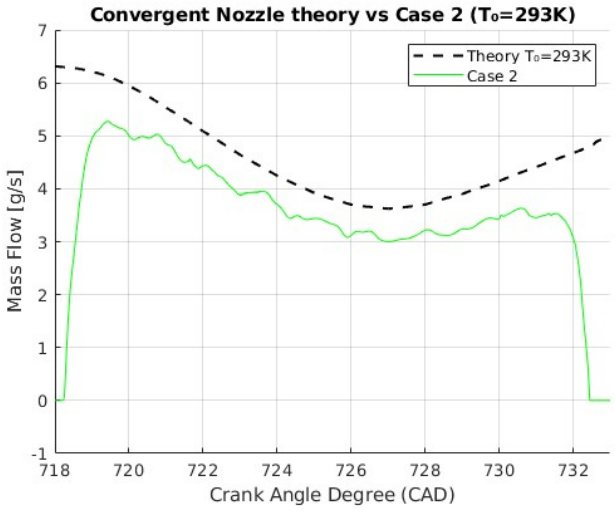

Figure 2.28: Case 2 ($T_0 = 293$ K). Comparison between the nozzle theory and CFD results (solid).

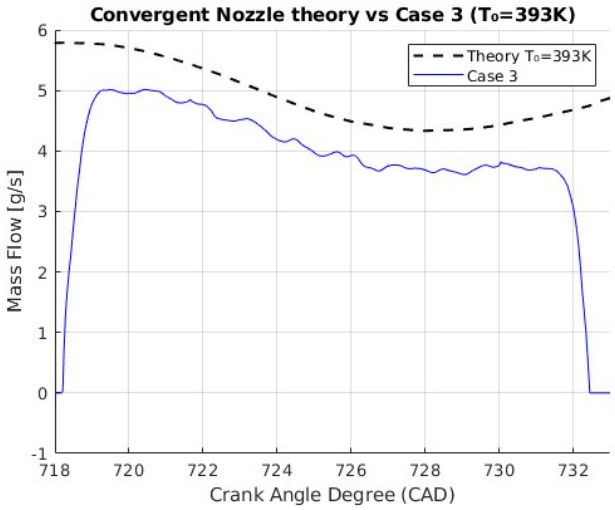

Figure 2.29: Case 3 ($T_0 = 393$ K). Comparison between the nozzle theory and CFD results (solid).

Upon examining the results, it becomes evident that the theoretical and simulated mass flow curves follow a similar trend throughout the injection event. Both profiles exhibit the same general shape. However, they appear to be slightly offset in magnitude, running approximately in parallel without intersecting.

This observation suggests that the difference between the isentropic model and the CFD simulations may be attributed to a global scaling factor. To investigate this hypothesis, we computed the local discharge coefficient C_d as the ratio between the simulated and theoretical mass flow rate at each crank angle:

$$C_d(\theta) = \frac{\dot{m}_{\text{sim}}(\theta)}{\dot{m}_{\text{theory}}(\theta)} \tag{2.3.8}$$

The resulting evolution of C_d is shown in Figure 2.30. All three cases show consistent trends: after the initial needle opening transient, C_d stabilizes in the range of approximately 0.85-0.88 during the main injection phase, before dropping again as the needle closes. Despite small oscillations and slight

variations between cases, the discharge coefficient remains remarkably consistent across the different operating points.

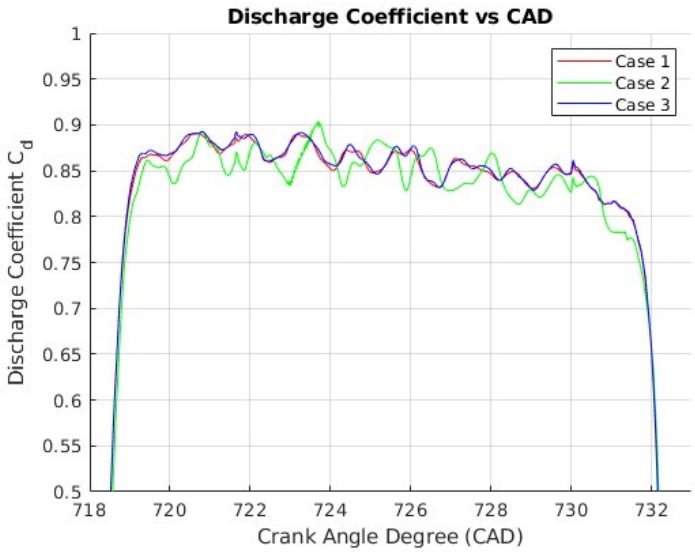

Figure 2.30: Computed discharge coefficient C_d from AVL results and the isentropic model, for the three test cases.

These results confirm that the isentropic flow model provides a reliable first-principles foundation for predicting hydrogen mass flow through the injector. Moreover, the relatively stable range of C_d suggests that a single average value could potentially be used in injection models, significantly simplifying calibration efforts without sacrificing physical realism.

2.3.3 Convergent-Divergent Nozzle theory

In the previous chapter, the injection process was modeled under the assumption that the hydrogen injector behaves as a purely convergent nozzle, where the narrowest section of the flow path corresponds to the outlet orifices. Under this assumption, the behavior of the injection follows the theory of isentropic compressible flow through convergent nozzles: the mass flow rate varies with the pressure ratio p_{cyl}/p_0, unless the flow becomes choked.

According to the convergent nozzle theory, this would result in a pressure-dependent mass flow rate and a curved injection profile as it was shown in Figure 2.22. However, if the minimum area is not at the nozzle exit, but rather somewhere upstream within the injector body, the internal geometry of the injector would resemble a convergent-divergent (CD) nozzle, where the flow first contracts to a throat and then expands toward the outlet.

Figure 2.31 illustrates the classical behavior of compressible flow through a convergent-divergent nozzle. In this configuration, the flow first accelerates through the converging section toward the throat, which is the location of minimum cross-sectional area. If the pressure ratio between the in-cylinder pressure and the rail pressure is high, the behavior is the same as in a Convergent nozzle. This means that the flow remains subsonic throughout the entire nozzle, and the mass flow rate increases with decreasing back pressure.

As the downstream pressure continues to drop, the velocity at the throat increases. When the Mach number at the throat reaches $M = 1$, the flow becomes choked. At this point, the mass flow rate reaches a maximum and becomes independent of the downstream pressure. Further reductions in back pressure no longer increase the mass flow, but they do affect how the flow behaves beyond the throat, in the divergent section.

The transitions in flow behavior are marked by a set of distinct pressure ratios known as the critical point of a convergent-divergent nozzle. These points determine the conditions under which the flow

transitions between different regimes. They are defined as follows:

- **First critical point (choking):** This occurs when the pressure ratio at the throat drops below the critical value defined by Eq. (2.3.2). At this point, the Mach number at the throat reaches $M = 1$ and the nozzle becomes choked. The flow rate is maximized and no longer depends on the downstream pressure. However, the flow remains subsonic in the divergent section. This is the regime of particular interest in this study.
- **Second critical point:** As the downstream pressure continues to decrease beyond the choking condition, the flow accelerates to supersonic speeds in the divergent section. However, due to the pressure mismatch between the ambient pressure and the pressure in the nozzle, a normal or oblique shock forms inside or near the nozzle exit, bringing the flow back to subsonic. This second critical point marks the pressure ratio needed to obtain a shock wave at the nozzle exit.
- **Third critical point (adapted nozzle):** This corresponds to the ideal supersonic condition where the exit pressure of the nozzle exactly matches the ambient pressure, allowing for a fully isentropic expansion to supersonic flow throughout the divergent section with no shock waves. This maximizes efficiency and thrust, but is rarely achieved in practice due to its precise pressure requirement, pressure ratios above this point result in an overexpansion while those below produce an underexpasion.

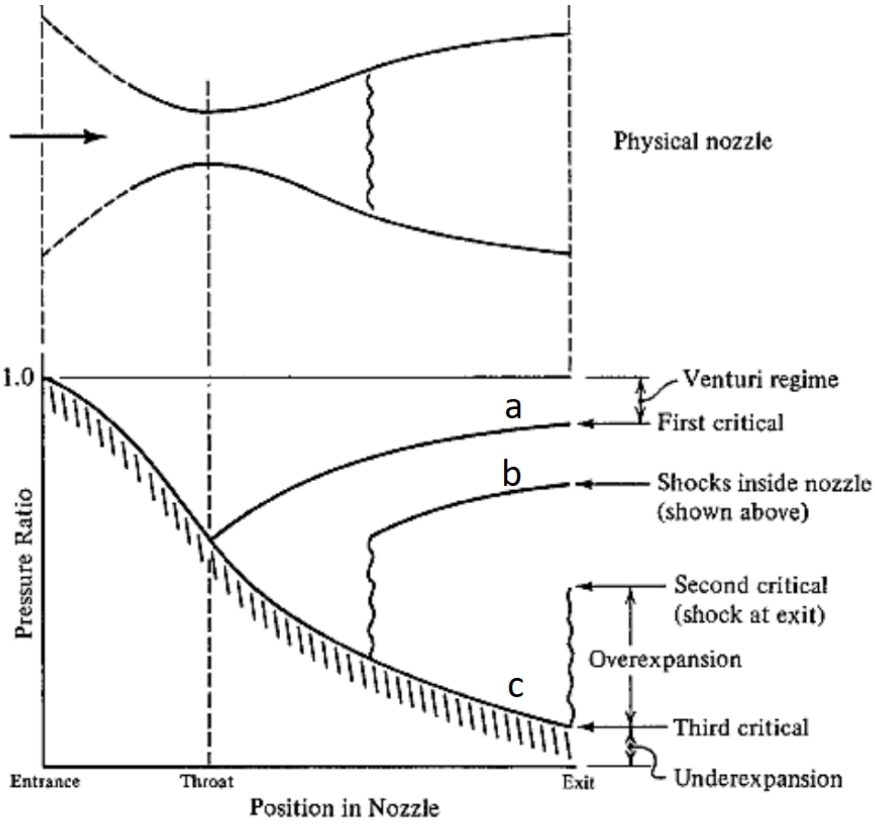

Figure 2.31: Schematic of convergent-divergent nozzle flow regimes. In our case, the throat may lie within the injector, upstream of the outlet holes. []

It is important to note that, unlike in purely convergent nozzles where the critical pressure ratio is fixed (e.g., $p_{cyl}/p_0 \approx 0.528$ for hydrogen), in convergent-divergent nozzles the pressure ratios at which each critical point occurs depend on the nozzle geometry, specifically, the ratio of throat area to exit area (A_{throat}/A_{exit}). For a given pressure ratio p_{cyl}/p_0, the nozzle can be choked if there is a critical value A^*/A_{exit} that ensures that the critical conditions are met in the nozzle. The ratio A^*/A_{exit} as a function of p_{cyl}/p_0 can be derived from the Mach number using the following equation:

$$\frac{A^*}{A_{\text{exit}}} = M\left[\frac{2}{\gamma+1}\left(1+\frac{\gamma-1}{2}M^2\right)\right]^{-\frac{\gamma+1}{2(\gamma-1)}}. \tag{2.3.9}$$

Where M is the Mach number at the exit of the nozzle and can be obtained directly from p_{cyl}/p_0 through isentropic theory.

$$\frac{p}{p_0} = \left(1+\frac{\gamma-1}{2}M^2\right)^{-\frac{\gamma}{\gamma-1}}, \tag{2.3.10}$$

In this study, we hypothesize that the injector operates between the first and second critical points: the flow is choked at an internal throat (with $M_{throat} = 1$), therefore the massflow remains independent of the in-cylinder pressure, but the exit flow remains subsonic. This condition allows the use of constant mass flow rates in injection profiles, even when the in-cylinder pressure is well above the critical threshold derived in convergent nozzle theory.

2.3.4 Application of Convergent-Divergent Theory to the Injector Conditions

In this section, the isentropic theory of compressible flow in convergent–divergent (CD) nozzles is applied to the specific case of the hydrogen injector considered in the first case of the study. The objective is to assess whether, under the pressure conditions observed experimentally, the injector could operate in a regime where choking occurs within a CD nozzle configuration, thereby sustaining a constant mass flow rate.

For this example case the choking conditions for a maximum in-cylinder pressure during injection of $p_{cyl} = 255$ bar and a rail pressure of $p_0 = 302.5$ bar will be derived. The outlet geometry consists of nine holes of diameter 0.676 mm, giving a total outlet area of:

$$A_{exit} = 9 \cdot \frac{\pi}{4} \cdot (0.676\ \text{mm})^2 \approx 3.229\ \text{mm}^2. \tag{2.3.11}$$

From the isentropic relation between pressure and Mach number, we solve for the exit Mach number corresponding to the pressure ratio $p_{cyl}/p_0 \approx 0.843$, and find:

$$M_{exit} \approx 0.498. \tag{2.3.12}$$

Using this, the area ratio A_{exit}/A^* is computed via:

$$\frac{A_{exit}}{A^*} = \frac{1}{M}\left(\frac{2}{\gamma+1}\left(1+\frac{\gamma-1}{2}M^2\right)\right)^{\frac{\gamma+1}{2(\gamma-1)}}. \tag{2.3.13}$$

Substituting, we find:

$$A^* \approx \frac{A_{exit}}{1.343} \approx 2.404\ \text{mm}^2. \tag{2.3.14}$$

Finally, the corresponding choked mass flow rate is computed using the full expression:

$$\dot{m} = A^* \cdot P_0 \cdot \sqrt{\frac{\gamma}{RT_0}} \cdot \left(\frac{2}{\gamma+1}\right)^{\frac{\gamma+1}{2(\gamma-1)}}. \tag{2.3.15}$$

Which gives:

$$\dot{m} \approx 39.26\ \text{g/s}. \tag{2.3.16}$$

$$\dot{m} \approx 4.36 \text{ g/s per hole.} \tag{2.3.17}$$

These results show that, with a throat area of $A_t = 2.404\,\mathrm{mm}^2$, the flow chokes and the mass flow rate plateaus at $\dot{m} = 39.26\,\mathrm{g/s}$ for pressures below $255\,\mathrm{bar}$. Reducing the throat area would extend the pressure range over which choking is sustained, but at a lower choked $\dot{m}$. Conversely, increasing the throat area raises the choked mass-flow rate while reducing the critical pressure ratio, meaning it reduces pressure range for choking.

2.4 Cases Analyzed

In order to validate and assess the different modeling approaches, three different cases are considered in this work. These cases are based on the two experimental datasets introduced previously, and an additional variation where there will be no diesel pilot to trigger the hydrogen ignition.

Chapter 3: Case 1 A75 – Reference experiment in previous work

The first experimental case corresponds to the main reference dataset. This set was used previously in the research made by Liu [41], Traecy [92] and Antonacci [12] to validate CFD models developed in converge. Therefore, most of the modeling work will be carried out in this case. Initially, the injector will be modeled using the convergent nozzle theory applied to two different mass flow curves. Subsequently, the convergent–divergent nozzle approach will also be applied and compared. Additionally, this case will also be used to evaluate the effect of modifications to the combustion model and timestep, in order to evaluate their effect on the simulation results. The last feature that will be evaluated using this case will be the effect of varying the size of the diesel pilot in the performance of the engine.

Chapter 2: Case 5 560HP – Second experimental dataset

The second case corresponds to the additional experimental dataset described earlier. The same methodology will be applied: both the convergent and convergent–divergent nozzle theories will be used to model the injector. However, no modifications will be introduced to the combustion model. This case will provide a means to assess the robustness and generality of the methodology when applied to a different operating condition.

Chapter 3: Hydrogen-only Case

Finally, a purely hydrogen-fueled case will be investigated, where the diesel pilot injection is removed. This configuration allows for the evaluation of the injection and combustion models in the absence of diesel ignition assistance, providing further insights into the applicability of the proposed methodology to future zero-carbon scenarios.

Chapter 3

Results and Discussion: Case 1 A75

3.1 Convergent Nozzle theory applied to case 1 A75

Following the analysis presented in the previous chapters, new mass flow injection curves were derived from isentropic nozzle theory using the experimental pressure curve. Unlike the flat-top profile used in the baseline case, the new curves reflect the theoretical influence of in-cylinder pressure on the instantaneous mass flow rate. The objective is to evaluate whether this physically-based injection profile improves agreement with experimental and simulated pressure traces. The same simulation setup as in the baseline case was retained to ensure a fair comparison, with the only change introduced being the injection profile.

3.1.1 First Injection Profile: Short Injection curve derived from Experimental Data

Figure 3.1 shows the first new injection curve used in this simulation. The injection timing was derived from the data collected from the first set of experiments which was presented in Table 2.2. The opening and closing stages were adjusted to deliver a total injected mass of 71 mg, with the only constraint being that both stages follow the same slope, which is a limitation that will be discussed in the following sections. Compared to the original flat-top profile, it exhibits a slight drop in the central part of the injection, consistent with what is predicted when the flow transitions into the subsonic regime as in-cylinder pressure increases.

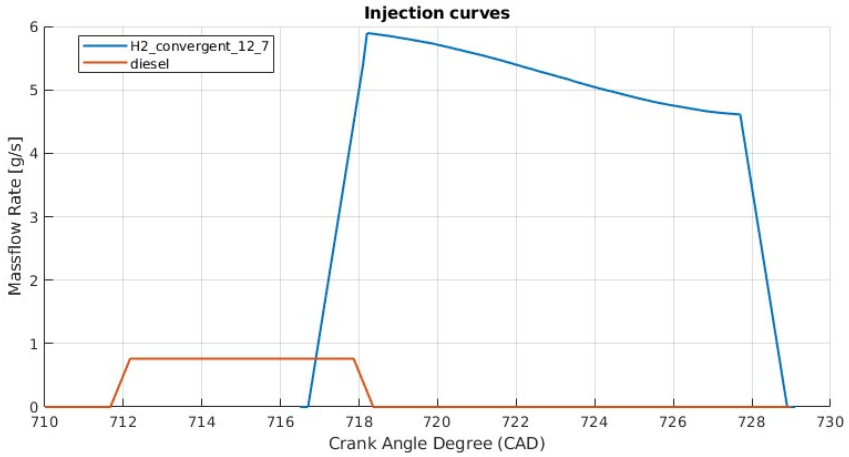

Figure 3.1: Injection profile based on isentropic flow theory used in the new simulation.

To assess the impact of this new injection curve, the resulting in-cylinder pressure trace from the new simulation was compared with both the previous flat-top injection case and the experimental pressure trace. As shown in Figure 3.2, the simulation using the convergent nozzle injection profile shows a clear improvement in capturing the experimental pressure trend.

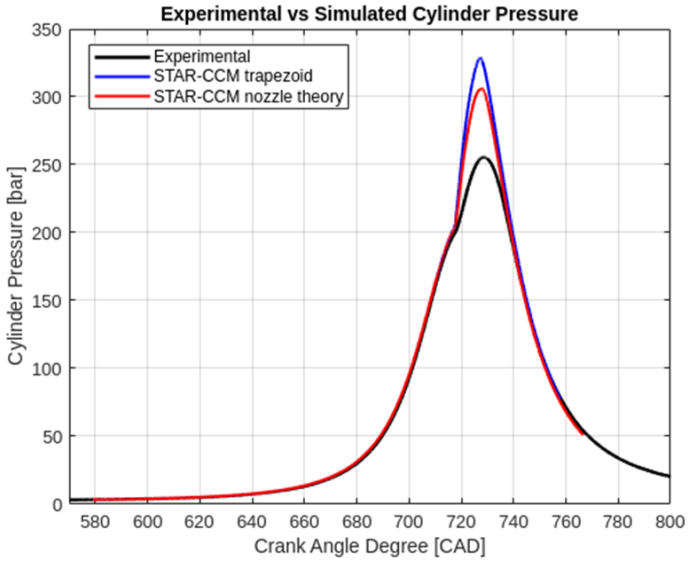

Figure 3.2: Comparison of in-cylinder pressure: baseline simulation (flat-top injection), convergent nozzle theory simulation, and experimental data.

Despite this improvement, the match is still not entirely satisfactory. A notable discrepancy remains in the peak of the pressure trace, suggesting that the actual injected mass per second may be lower than predicted. This leads to the hypothesis that the injector hydraulic dynamics may not be as easy to correlate with the electric signals measured in the experiment as it was initially assumed. The following chapter will explore an alternative injection that considers longer injection durations in order to evaluate their effect on the agreement with the experimental results.

3.1.2 Second Injection Profile: Alternative Long Injection Curve Based on Previous Work

Building on the results discussed in the previous section, it appears that the mismatch in the peak pressure may be linked to an underestimation of the effective injection duration. To investigate this further, the injection strategy employed in the earlier CFD work of Antonacci [12] was taken as a reference. Since his study was conducted using the same experimental campaign as the present thesis, it provides a particularly relevant benchmark for comparison.

In that work, although the nominal injection duration derived from the electrical command was 10.7 CAD, the injection duration implemented in the CFD model was significantly longer, 19.2 CAD, measured from the start of needle opening to full closure. This extended duration may appear inconsistent with the experiment at first glance; however, it was necessary in order to construct a flat-top injection profile that matched the target total injected mass of 71 mg. In practice, matching this mass with a trapezoidal profile required either slowing down the opening and closing transitions or reducing the plateau flow rate and extending the injection time.

Based on this observation, a new simulation was performed using the same total duration of 19.2 CAD, but instead of a flat-top profile, the injection curve was generated using the isentropic flow model. Figure 3.3 shows the resulting mass flow rate curve, which preserves the theoretical shape in the central region and features smooth ramps at the beginning and end, extending the total injection period.

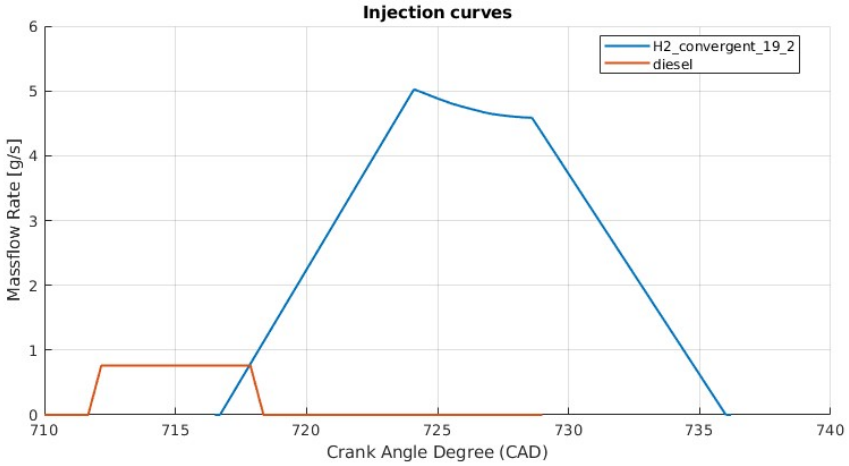

Figure 3.3: Injection profile based on the isentropic flow model with a total duration of 19.2 CAD.

The resulting in-cylinder pressure trace is compared in Figure 3.4 against the previous simulation and the experimental data. As seen in the plots, the use of a longer injection duration leads to a substantial improvement in the predicted pressure magnitude. In particular, the new trace is much closer in shape and peak value to the experimental result. Although a slight phase shift remains, visible in the zoomed view in Figure 3.4b, the overall agreement is significantly better.

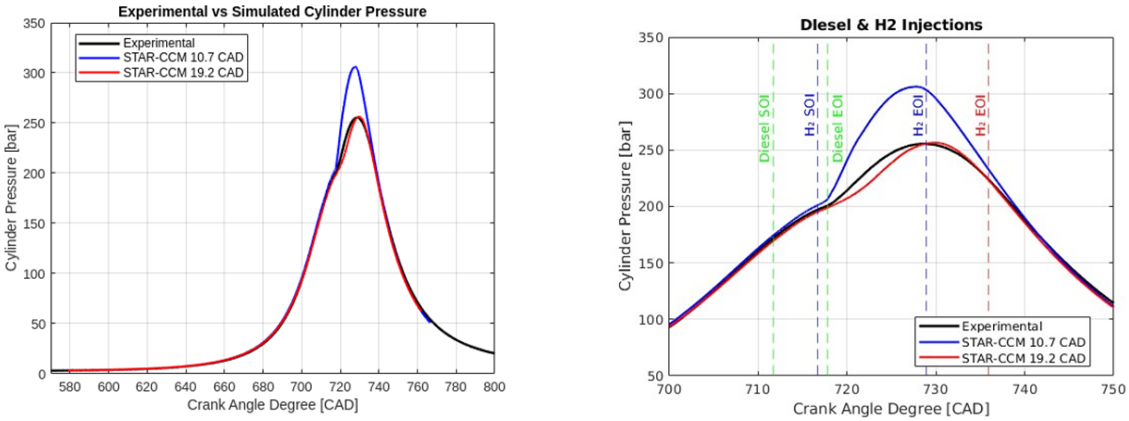

(a) Full-cycle comparison of in-cylinder pressure.

(b) Detail view around peak pressure.

Figure 3.4: Comparison of in-cylinder pressure using long-duration injection (19.2 CAD), original simulation (10.7 CAD), and experimental result.

These results provide encouraging evidence that the actual effective injection duration, including the hydraulic opening and closing phases, may be longer than the nominal electrical duration assumed in the baseline case. This supports the hypothesis that the injector's hydraulic response is not perfectly synchronized with the electrical command used in the experimental measurements.

To investigate this further, the next section will examine the apparent heat release rate (aHRR) profiles. The goal is to gain additional insight into the real injection dynamics.

3.1.3 Heat Release Curves as an Indicator of Injection Dynamics

In the previous section, a longer injection duration was tested using the isentropic flow model, and the results showed a significant improvement in matching the experimental in-cylinder pressure trace. However, although the pressure profile became much more similar to the experimental one, some discrepancies still remained, particularly visible in the timing of the peak pressure.

To better understand these differences and investigate what might still be missing from the injection modeling, now the attention is turned into the apparent heat release rate (aHRR) curves. The goal is to assess whether the combustion response can offer additional insight into the true dynamics of the injection process.

To further investigate the differences between simulation and experiment, this subsection begins by examining the apparent heat release rate (aHRR) curves from the last two CFD simulations. These correspond to the short-duration and long-duration injection cases using the isentropic mass flow profiles. Figures 3.5 and 3.6 show the aHRR as a function of crank angle for each case.

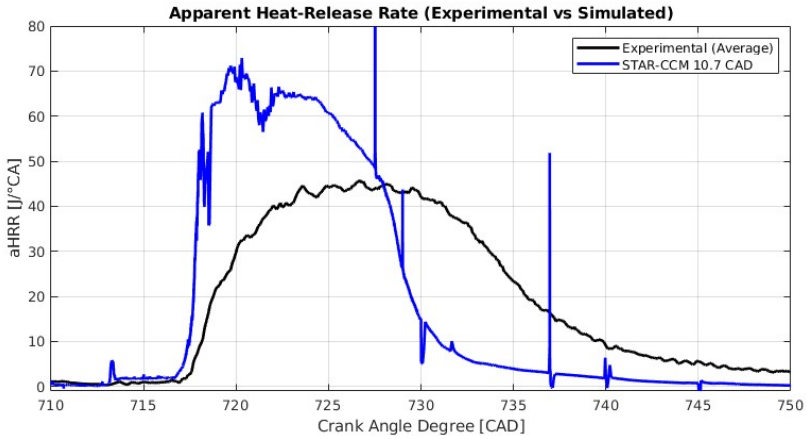

Figure 3.5: Apparent heat release rate (aHRR) for the short-duration injection case.

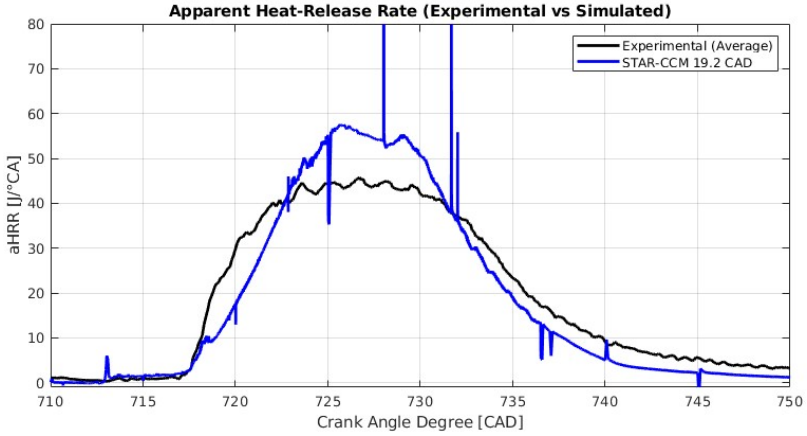

Figure 3.6: Apparent heat release rate (aHRR) for the long-duration injection case.

Although neither of the simulated cases appears to reproduce the experimental aHRR trends, as shown in Figures 3.5 and 3.6, what truly stands out is not the discrepancy itself but the apparent correlation between the injection profile and the simulated aHRR. Upon closer inspection, a visual similarity between the shape of the aHRR and the previously used injection curves was noted. To explore this further, the aHRR and the hydrogen mass flow rate were plotted together for each case. Figures 3.7 and 3.8 illustrate this comparison, where the aHRR is plotted on the left axis and the instantaneous injection

rate on the right. The similarity in shape is striking: the aHRR appears to follow the mass flow rate profile almost directly, with only a minimal delay.

Figure 3.7: Comparison between aHRR (right axis) and injection profile (left axis) for the short-duration case.

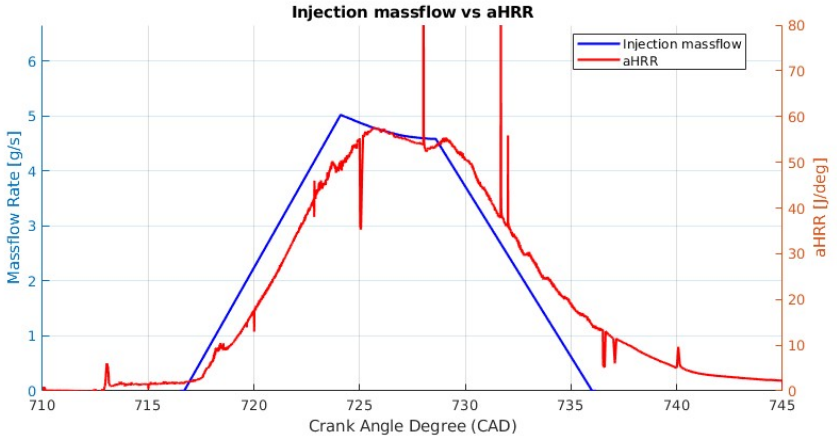

Figure 3.8: Comparison between aHRR (right axis) and injection profile (left axis) for the long-duration case.

This correlation strongly suggests that the injected hydrogen undergoes combustion almost immediately upon entering the combustion chamber. The apparent Heat Release Rate (aHRR) can be interpreted as a filtered and slightly delayed representation of the hydrogen mass flow rate, with only a minor phase shift of approximately $1{-}1.5\ \mathrm{CAD}$ between the injection event and the onset of combustion. The two quantities are related through a proportionality factor that has been plotted in Figures 3.9 and 3.10, which has an average value of about $11.5\ \frac{\mathrm{J{\cdot}s}}{\mathrm{g{\cdot}CAD}}$, corresponding to an average specific energy release of $83\ \frac{\mathrm{MJ}}{\mathrm{kg}}$. This value is approximately 30% lower than the theoretical energy density of hydrogen ($120\ \frac{\mathrm{MJ}}{\mathrm{kg}}$), likely due to heat losses and incomplete energy conversion within the combustion chamber, which eventually takes place later in the combustion process.

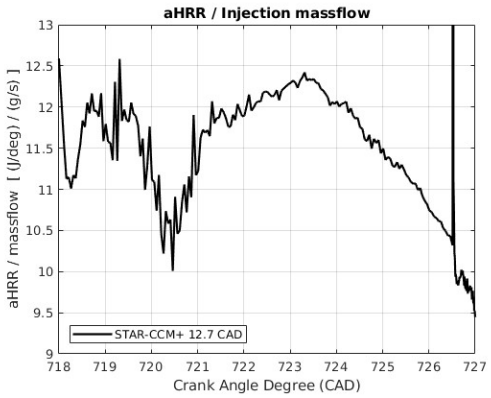

(a) Short duration case.

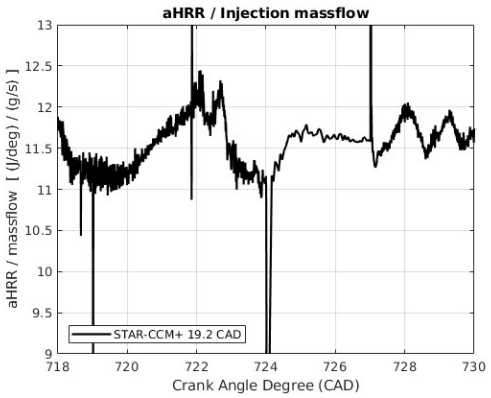

(b) Long duration case.

Figure 3.9: Apparent heat Release Rate divided by the injection massflow (J s/g CAD).

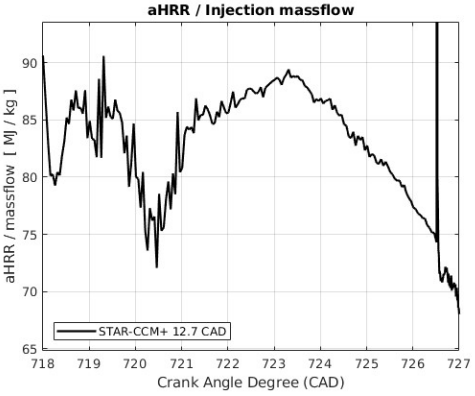

(a) Short duration case.

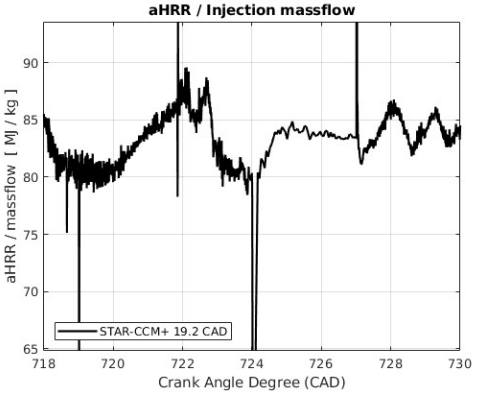

(b) Long duration case.

Figure 3.10: Apparent heat Release Rate divided by the injection massflow (MJ/kg).

Interestingly, this strong correlation between the aHRR and the injection profile is consistent with previous findings obtained in CONVERGE simulations by Antonacci, who also observed that the shape of the heat release curve closely followed the injection dynamics. However, the degree of similarity in CONVERGE appeared to be somewhat less pronounced than in the present cases from Star-CCM+, as can be seen in Figure 3.11. This reinforces the interpretation that the heat release shape can indeed serve as a reliable indicator of the underlying injection process.

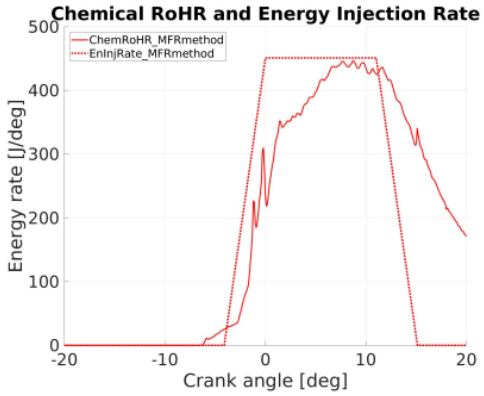

(a) MFR method injection.

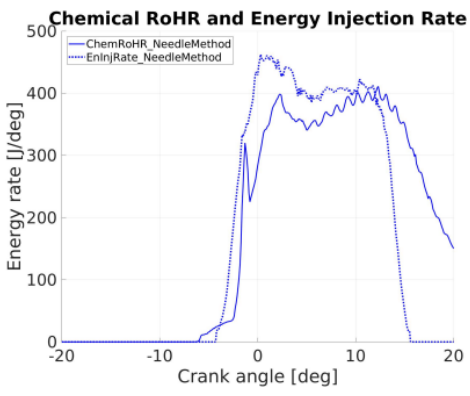

(b) Needle motion method injection.

Figure 3.11: Chemical RoHR and energy injection rate for different injection curves from Antonacci [12].

3.1.4 Deriving Injection Profile from the Experimental aHRR

Building on the observations done in the previous subsection, the experimental aHRR trace can now be used to derive the shape of the actual injection obtained in the test. Since the simulated heat release curves were shown to closely reflect the form of the injection profiles, examining the experimental aHRR may provide valuable information about how fuel was actually injected. Figure 3.12 shows the experimental aHRR curve plotted over crank angle degrees.

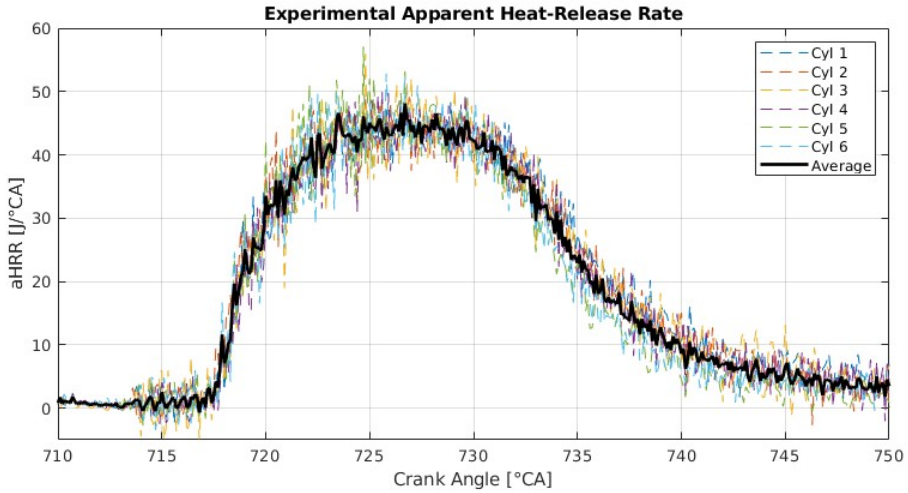

Figure 3.12: Experimental apparent heat release rate (aHRR).

To facilitate comparison, Figure 3.13 overlays the experimental curve with the aHRR traces from the two previous CFD simulations, the short-duration and long-duration injection cases.

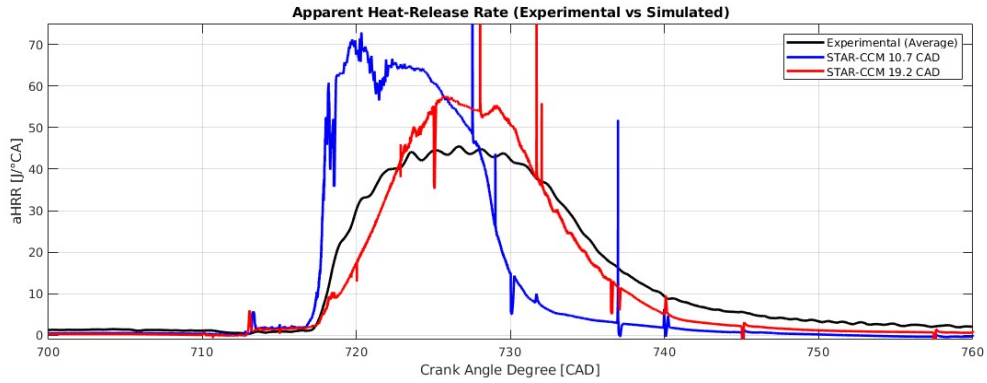

Figure 3.13: Comparison of aHRR profiles: experimental vs. previous CFD simulations.

From this comparison, four key discrepancies emerge that cannot be reconciled within the framework of the Convergent Nozzle Theory:

1. **Peak magnitude of aHRR.** The experimental aHRR exhibits a substantially lower peak, around 45 J/CAD, whereas the simulated cases reach approximately 60–70 J/CAD. If hydrogen were to combust immediately upon injection, such a difference strongly suggests that the actual injected fuel mass was lower than the values predicted using the convergent nozzle assumption.
2. **Shape of the injection phase.** The experimental trace departs notably from the simulated ones. While the convergent-nozzle-based simulations produce a sloped profile during the main injection phase, the experimental curve displays a flatter region, more consistent with a nearly constant mass flow rate. This indicates that the real injection process cannot be accurately described by

the pressure-driven reduction imposed by the convergent nozzle model, but instead it is limited somehow in the injector.

3. **Injection duration.** The duration of the experimental aHRR matches more closely the long-duration case (approximately 20 CAD) rather than the nominal 10.7 CAD commanded electrically. This mismatch points to injector dynamics, such as hydraulic delays and extended needle motion.
4. **Opening and closing slopes.** A closer look at the rising and falling edges of the experimental curve reveals additional insight. The rising slope lies between the short- and long-duration simulation cases, whereas the decay slope closely resembles that of the long-duration injection. This suggests that the injector needle opens at an intermediate speed but closes more slowly, which is physically consistent with hydraulic resistance as the closing stages occur when there is higher in-cylinder pressures.

Taken together, these differences indicate that the Convergent Nozzle Theory alone cannot reproduce the experimental injection and combustion behavior. For this reason, the following section introduces a data-driven approach to construct a more realistic injection curve, directly derived by the experimental aHRR trace.

3.2 Convergent–Divergent Nozzle theory applied to Case 1 A75

Based on the insights obtained from the experimental aHRR curve, a new injection profile was constructed and implemented in a CFD simulation. The objective was to evaluate whether a flat-top mass flow profile with a duration and flow rate derived from the experimental aHRR curves could reproduce the experimentally observed combustion and pressure characteristics.

The curve used in this simulation is shown in Figure 3.15. It consists of a central flat segment delivering approximately 3.7 g/s, obtained from dividing the experimental aHRR by 11.5, which as it was shown in the last section, represents the approximated conversion factor obtained from the correlation between injection rates and measured heat release in the previous cases. The injection event spans a total duration of 20 CAD. The rising edge of the injection curve, corresponding to the opening of the injector, was designed to be relatively sharp, occurring within 3 CAD (417 μs), whereas the closing phase was made more gradual with a closing time of 7 CAD (972 μs). This asymmetric shape of the curve, which had not been explored before, was designed following the reasoning discussed earlier: due to the hydraulic nature of the injector and the higher in-cylinder pressure near the end of the event, it is reasonable to expect that the needle closes more slowly than it opens. Interestingly, the opening and closing times obtained from this analysis were later found to be in close agreement with the values reported by CESPIRA for their internal injector simulations, which specify opening durations of 0.4-0.6 ms and closing durations of 0.7-1.0 ms.

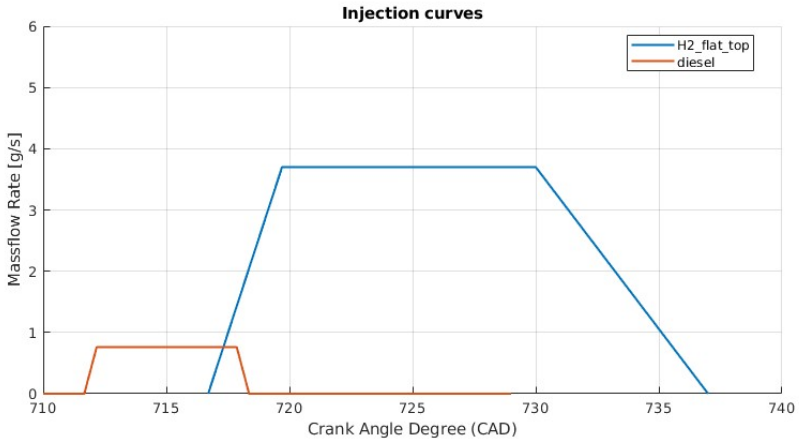

Figure 3.14: Injection profile obtained using convergent-divergent nozzle theory: flat-top of 3.7 mg/CAD over 20 CAD, with fast opening (3 CAD) and slower closing (7 CAD).

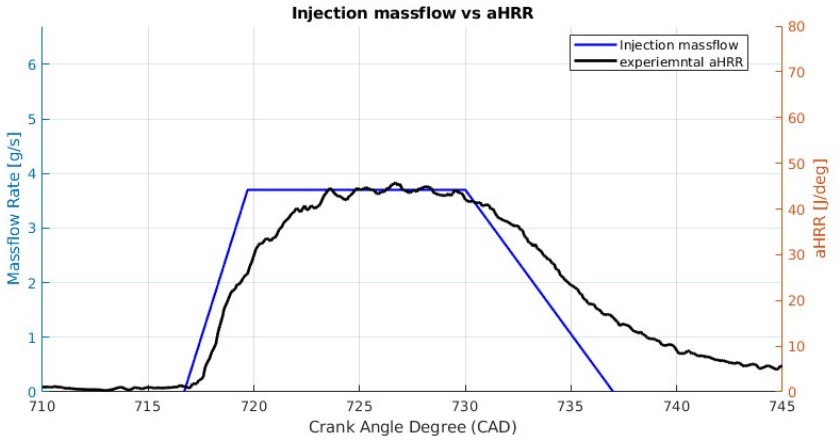

Figure 3.15: Injection profile obtained using convergent-divergent nozzle theory vs. aHRR obtained from the experiemnte (filtered).

The resulting pressure trace and heat release curve obtained from the simulation are presented in Figures 3.16 and 3.17, compared against the experimental data. It can be seen that the agreement between the simulated and experimental curves has improved significantly compared to previous cases. In the aHRR profile, both the rising and falling edges of the curve are well captured by the simulation, suggesting that the transient behavior of the injection has been accurately modeled. Although the overall shape and timing are well aligned, the main remaining discrepancy lies near the top of the aHRR curve, where the simulation slightly underestimates the peak values. This could indicate that the amount of energy released during combustion is still underestimated by the combustion model or that the fuel injected is higher than expected. To confirm which of these hypothesis is correct, in the coming section the combustion model will be changed.

Similarly, the pressure traces show excellent agreement throughout most of the cycle, including the compression and expansion phases. As expected, the underprediction of peak aHRR translates into a slightly lower peak pressure in the simulation. However, the general profile is very close to the experimental result, indicating that the current injection strategy and combustion model are heading in the right direction.

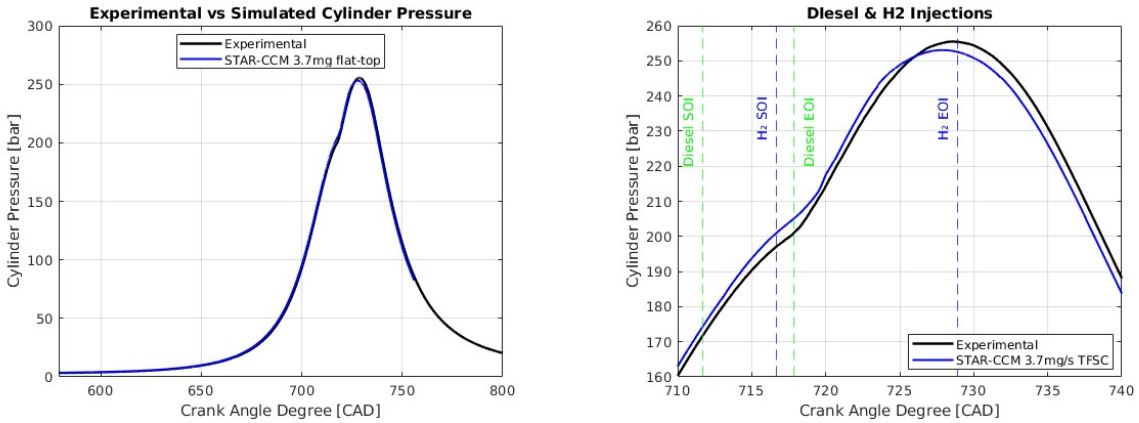

(a) 579 to 800 CAD.

(b) 710 to 740 CAD.

Figure 3.16: Comparison of pressure curve obtained for a top flat injection with the experimental result.

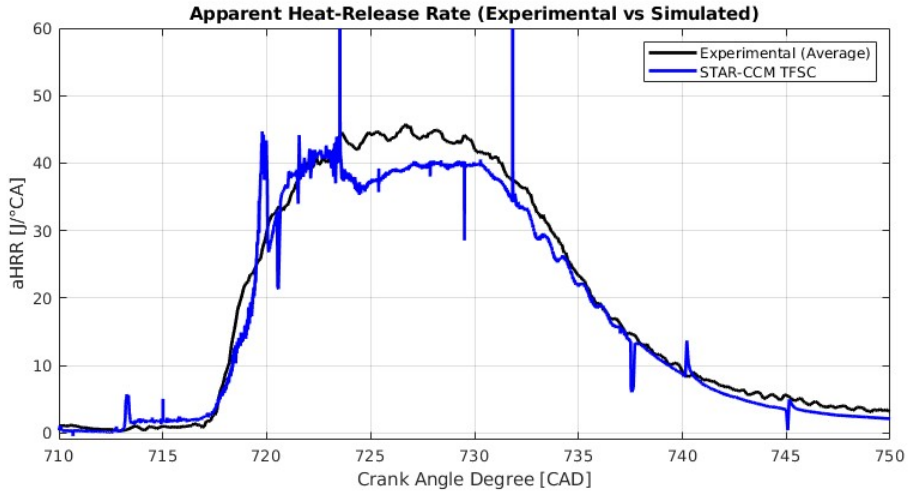

Figure 3.17: Comparison of aHRR curve obtained for a top flat injection with the experimental result.

3.2.1 Convergent Nozzle Rationale for the Flat-Top Injection

To explain the flat-top mass-flow profile introduced above, we use convergent nozzle theory to show that the observed plateau is consistent with choked flow through an effective throat. The analysis assumes a rail pressure of $p_0 = 302.5$ bar and a rail temperature of $T_0 = 350$ K.

Assuming the injector delivers approximately 3.7 g/s per hole, with nine holes in total, the total mass flow rate is:

$$\dot{m}_{\text{total}} = 3.7 \times 9 = 33.3 \text{ g/s}. \tag{3.2.1}$$

Using this value, the required throat area for choked flow is:

$$A^* = \frac{\dot{m}}{p_0 \cdot \sqrt{\frac{\gamma}{RT_0}} \cdot \left(\frac{2}{\gamma+1}\right)^{\frac{\gamma+1}{2(\gamma-1)}}} \approx 2.042 \text{ mm}^2. \tag{3.2.2}$$

With $A_{\text{exit}} = 3.229$ mm^2, the area ratio is:

$$\frac{A_{\text{exit}}}{A^*} \approx 1.582. \tag{3.2.3}$$

From this area ratio, a numerical solution gives the exit Mach number:

$$M_{\text{exit}} \approx 0.402, \tag{3.2.4}$$

and the backpressure required to sustain choking at this flow is:

$$\frac{p_{\text{cyl}}}{p_0} = \left(1 + \frac{\gamma - 1}{2} M^2\right)^{-\frac{\gamma}{\gamma-1}} \approx 0.8939, \tag{3.2.5}$$

which yields:

$$p_{\text{cyl}} \approx 270.4 \text{ bar}. \tag{3.2.6}$$

Because this value exceeds the in-cylinder pressures observed during the injection event, the flow remains choked over the whole range. Consequently, an effective throat area of about 2 mm^2 naturally yields a constant mass flow rate, providing a mechanistic explanation for the flat-top segment observed in the injection profile.

3.3 Modifications to the Modeling Configuration

Although the introduction of the flat-top injection profile has significantly improved the agreement between simulation and experimental data, subtle discrepancies remain in both the in-cylinder pressure trace and the apparent heat release rate. This suggests that further refinements are needed on the combustion side of the model.

In this section, several modifications to the combustion modeling are investigated. First, the TFSC (Turbulent Flame Speed Closure) approach is replaced by the LFC (Laminar Flamelet Closure) model in order to evaluate the sensitivity of the results to the combustion formulation. Second, the turbulent Schmidt number is reduced from its default value of 0.9 to 0.5, which is expected to increase the mixing of the hydrogen. Finally, the influence of exhaust gas recirculation (EGR) is tested by increasing the EGR rate from 0% to 5%. These modifications aim to assess the robustness of the CFD framework and to identify which modeling assumptions are most critical for accurately capturing hydrogen-diesel combustion under the studied conditions.

3.3.1 Comparison Between TFSC and LFC Combustion Models

The flat-top injection profile introduced previously reproduces the experimental trends with good accuracy: both the in-cylinder pressure and the aHRR curves show realistic timing, correct transient behavior during opening and closing, and an injected hydrogen mass close to the expected 71 mg. Nevertheless, a discrepancy remains in the peak of the aHRR curve, where the simulation underestimates the experimental result. Since both the transient ramps and the integrated mass have already been matched, there is limited room for further adjustments to the injection profile without compromising these agreements.

For this reason, the focus is shifted from injection dynamics to the combustion modeling itself. Up to this point, the TFSC model has been employed. While efficient, this approach relies on pre-computed flame speed tables, which may limit its ability to capture the detailed combustion physics under hydrogen–diesel dual-fuel conditions. As an alternative, the LFC model was tested, in which the flame speed is computed dynamically as a function of the local thermochemical state. Additionally, TFSC is a model that has been designed to perform well in turbulent scenarios while LFC does not introduce turbulence in the resolution of the transport equation which can make it more accurate if the levels of premixing are not very high.

Figures 3.18 and 3.19 compare the results of both combustion models against the experimental measurements. The TFSC results are shown in blue, while the LFC case is shown in red.

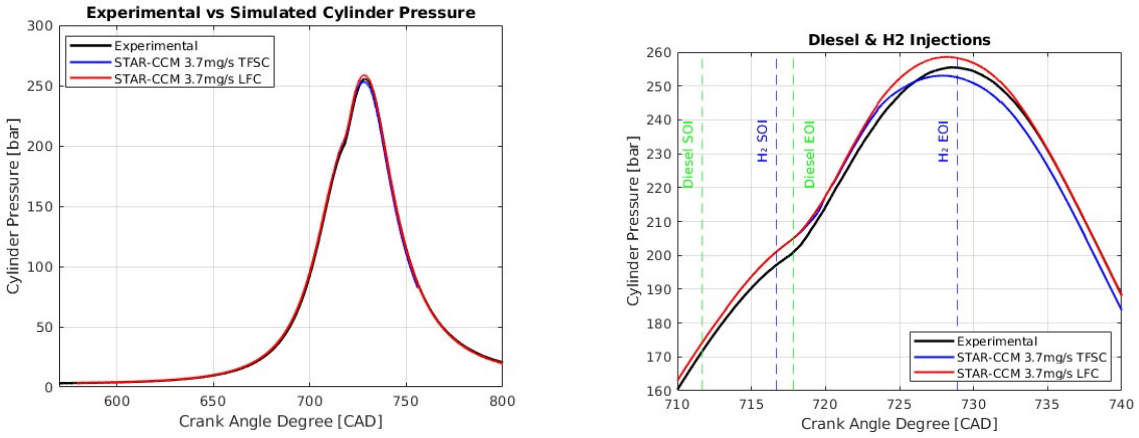

(a) 579 to 800 CAD.

(b) 710 to 740 CAD.

Figure 3.18: Comparison of simulated and experimental pressure traces using TFSC and LFC combustion models.

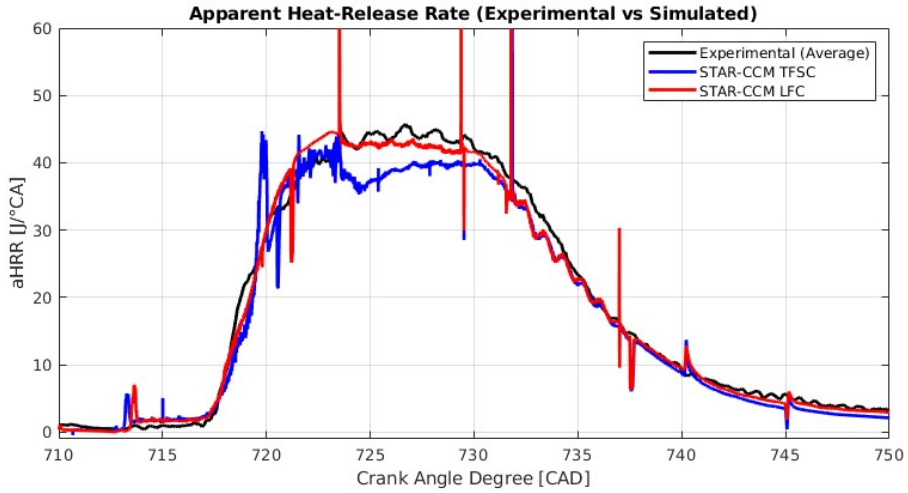

Figure 3.19: Comparison of aHRR curves obtained with TFSC and LFC combustion models.

The results indicate that switching to the LFC model produces a more pronounced and stable peak in the aHRR curve, bringing the simulation closer to the experimental measurement. This improvement also translates into a slightly higher peak cylinder pressure, thereby reducing the remaining discrepancy. The general shape and phasing of both curves remain consistent with the previous results.

Figure 3.20 shows the aHRR divided by the massflow rate in MJ/kg for both TFSC and LFC, it can be observed that the LFC converts more fuel into energy in the main stages of combustion. These figures suggest that the TFSC model may estimate a high energy release during the early stages, when there is higher mixing, but underestimate it during the main injection, where the flame is more diffusive, probably due to its reliance on tabulated laminar flame speeds and the derived turbulent flame speed approximation. By contrast, the LFC model provides a more adaptive description of the combustion process under the present conditions. For this reason, the LFC model will be adopted as the baseline approach in the subsequent analyses.

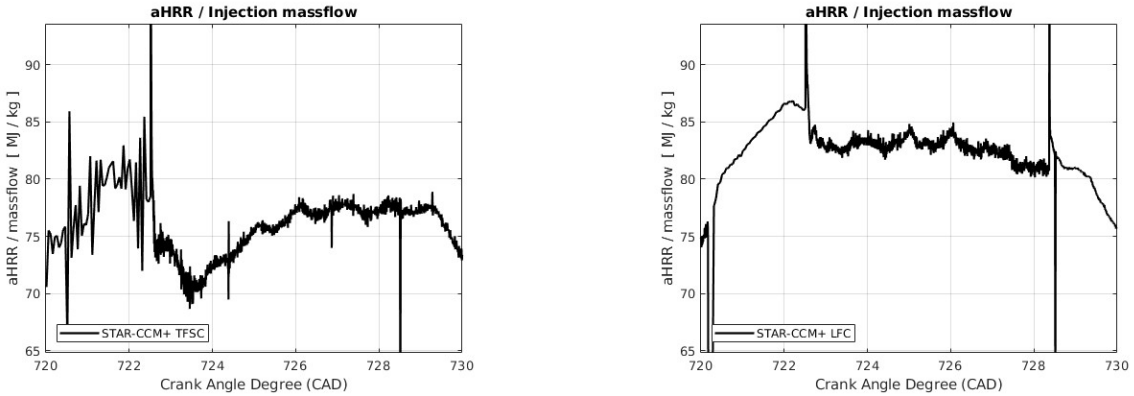

(a) TFSC. **(b)** LFC.

Figure 3.20: Apparent Heat Release Rate divided by the injection massflow (MJ/kg).

In summary, the combination of the flat-top injection profile with the LFC combustion model yields simulation results that closely match both the experimental in-cylinder pressure and aHRR curves. While minor discrepancies remain, they are sufficiently small to conclude that the essential injection dynamics and combustion behavior of this case have been successfully captured.

3.3.2 Turbulent Schmidt Number Variation

The turbulent Schmidt number (Sc_t) controls the relative efficiency of turbulent mixing of scalar quantities compared to the transport of momentum. Lower values enhance turbulent diffusivity and promote faster homogenization of the fuel–air mixture, while higher values suppress scalar mixing and maintain steeper concentration gradients.

In most combustion simulations, values in the range of 0.7-0.9 are typically used, corresponding to slightly slower scalar mixing relative to momentum transfer. To evaluate the influence of turbulent mixing intensity on the combustion behavior, two simulations were performed with $Sc_t = 0.9$ (the default value in STAR-CCM+) and $Sc_t = 0.5$, following the range recommended in literature for mixing-dominated flows such as hydrogen injection.

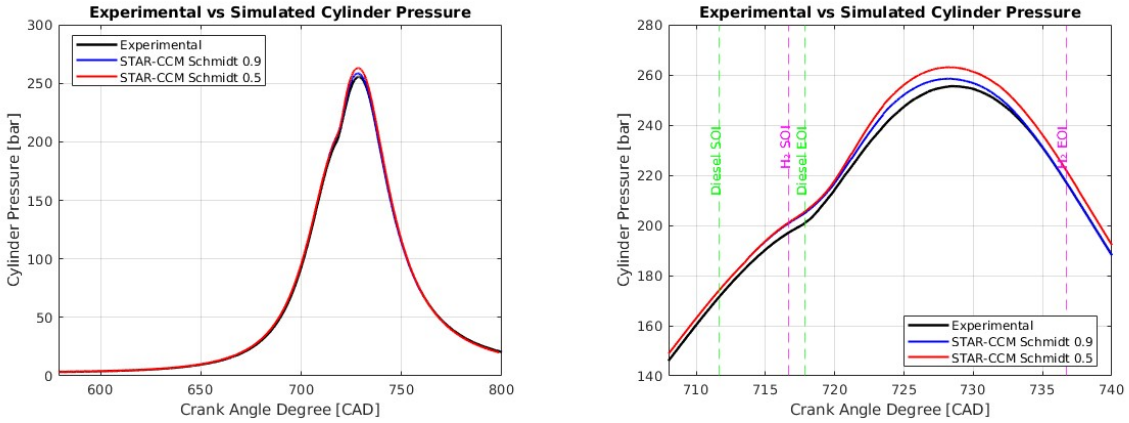

(a) 570 CAD to 800 CAD.

(b) 708 CAD to 740 CAD.

Figure 3.21: Comparison of simulated and experimental pressure traces with different turbulent Schmidt numbers: 0.5 vs. 0.9.

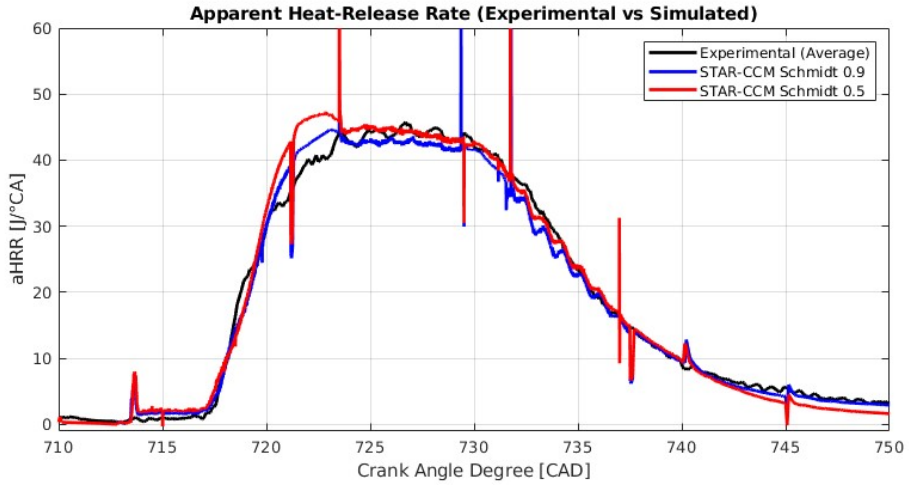

Figure 3.22: Comparison of aHRR curves obtained with different turbulent Schmidt numbers: 0.9 vs. 0.5.

The results show that varying Sc_t produces only minor differences in the pressure trace, indicating that the overall combustion phasing is largely unaffected. However, a noticeable effect appears in the aHRR at the beginning of the injection event. The case with the lower $Sc_t = 0.5$ exhibits a slightly higher initial aHRR, suggesting that the enhanced turbulent mixing leads to a more homogeneous hydrogen–air mixture prior to ignition, which releases more energy during the early combustion phase.

Beyond this initial stage, both cases converge to similar trends, with $Sc_t = 0.9$ still providing an excellent overall match to the experimental pressure and aHRR profiles. The observed sensitivity therefore

aligns with the expected physical behavior, lower Sc_t increases mixing efficiency, but given the already accurate agreement obtained with the default value, $Sc_t = 0.9$ was retained as the reference for subsequent analyses.

3.3.3 EGR Content: 0% vs. 5%

Finally, the gas composition was modified by introducing 5% of mass Exhaust Gas Recirculation (EGR), as a way to test the sensitivity of hydrogen combustion to the air composition. EGR was implemented by adjusting the composition of the intake gas to include a small fraction of inert combustion products, mainly CO2 and H2O, instead of assuming pure air (O2 + N2).

These species have significantly higher specific heat capacities compared to nitrogen or oxygen, which effectively reduces the ratio of specific heats $\gamma = \frac{c_p}{c_v}$ of the mixture. A lower γ leads to a lower pressure increase for a given temperature rise, and reduces the adiabatic flame temperature resulting from the same amount of heat release. This not only weakens the thermal driving force of combustion but also slows down chemical kinetics, contributing to delayed ignition and lower peak pressure. Figures 3.23 and 3.24 present the results obtained for 0% and 5% EGR.

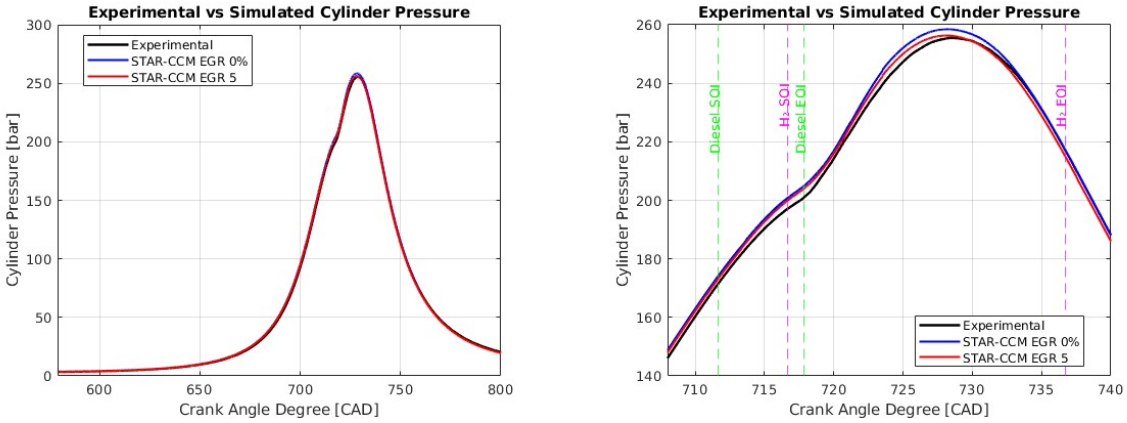

(a) 570 CAD to 800 CAD.

(b) 710 CAD to 718 CAD.

Figure 3.23: Comparison of simulated and experimental pressure traces with different EGR: 0% vs. 5%.

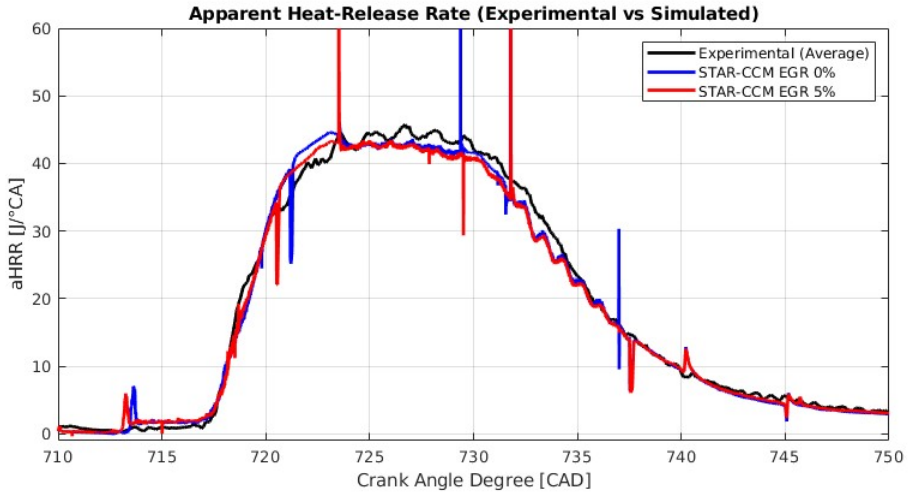

Figure 3.24: Comparison of aHRR curves obtained with different EGR: 0% vs. 5%.

The results confirm the expected effect of EGR on hydrogen combustion. The introduction of 5% EGR leads to a noticeable reduction of the initial aHRR peak, while the rest of the combustion curve remains very similar but slightly lower compared to the case without EGR. This behavior is consistent with the thermodynamic and kinetic effects described earlier, as the presence of CO2 and H2O moderates the temperature rise and slows the chemical reactions. However, the magnitude of this effect is relatively small, and given that the experimental operating conditions considered in this study include only about 1.5–2% EGR, it is unlikely that EGR plays a major role in explaining the discrepancies between simulation and experiment.

3.3.4 Conclusions on Modeling Modifications

The analyses performed in this section highlight the relative influence of different modeling assumptions on the prediction of hydrogen–diesel dual-fuel combustion. The comparison between TFSC and LFC clearly showed that the LFC model provides a more accurate representation of the combustion process, especially in reproducing the peak of the aHRR curve, and will therefore be adopted as the baseline approach in subsequent analyses.

The variation of the turbulent Schmidt number from 0.9 to 0.5 demonstrated that hydrogen's high diffusivity does affect the early stages of combustion, with a higher initial aHRR observed at lower Sc_t. This behavior is consistent with enhanced mixing and a larger premixed contribution, although the overall impact on the global combustion process remains modest.

Finally, the sensitivity study on EGR confirmed the expected moderating effect of products such as CO2 and H2O, reducing the initial heat release peak and slightly lowering the pressure rise. Nevertheless, since the experimental cases considered here involve only 1.5–2% EGR, this effect is too small to explain possible discrepancies between simulation and experiment.

Overall, these investigations suggest that the choice of combustion model (TFSC vs. LFC) has the largest impact on simulation accuracy, while adjustments to Sc_t and moderate levels of EGR play secondary roles. This underlines the importance of properly capturing the flame dynamics and local thermochemical state in order to model hydrogen combustion with sufficient fidelity.

To consolidate these findings, Table 3.1 summarizes the physical and numerical models that will be employed in the subsequent case studies. These settings reflect the conclusions drawn here, adopting the LFC approach for flame propagation, retaining the default turbulent transport coefficients, and neglecting EGR effects due to their minor influence under the investigated operating conditions.

Table 3.1: Summary of physical models adopted for subsequent simulations.

Model Type	Model or Setting
Turbulence Model	RNG k–ε
Combustion Model	Complex Chemistry
Flame Speed Model	Laminar Flame Concept (LFC)
Reaction Mechanism	Gustavsson n-heptane mechanism
Diesel Atomization Model	Huh Atomization
Diesel Spray Breakup Model	Reitz–Diwakar model
Equation of State	Redlich–Kwong real gas model
Molecular Diffusivity	Kinetic Theory
Thermal Conductivity	Mathur–Saxena
Turbulent Schmidt Number (Sc_t)	0.9 (default)
Turbulent Prandtl Number (Pr_t)	0.9 (default)
Exhaust Gas Recirculation (EGR)	0.0%

3.4 Numerical Sensitivity to Time Step: Case 1 (A75)

During the analysis of Case 1, noticeable spikes were observed in the apparent heat release rate (aHRR) curves. Based on their characteristics, it was hypothesized that the nature of these spikes was numerical rather than physical, as they coincided with changes in the time step size and with the automatic remeshing events performed by the solver. To confirm this assumption, a new simulation was carried out using a constant time step strategy, allowing a direct comparison against the adaptive time refinement approach.

In the adaptive configuration, the time step was reduced during the needle opening and closing phases of the injection, while larger values were used during the fully open phase. By contrast, in the constant configuration, a fixed small time step was applied throughout the entire injection event. Figure 3.25 illustrates the two strategies.

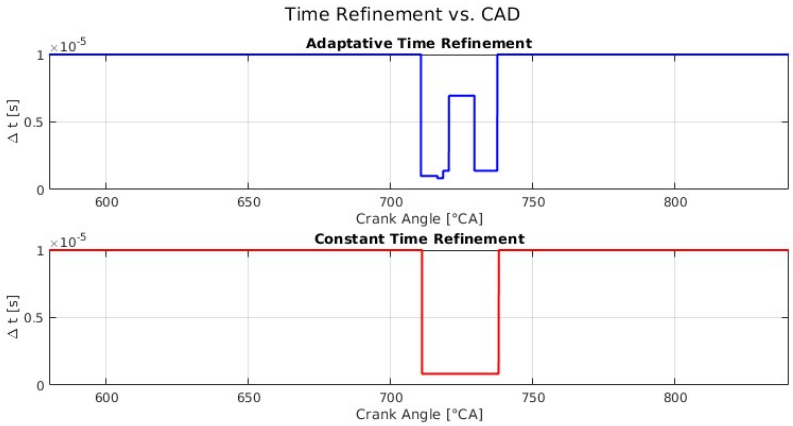

Figure 3.25: Comparison of adaptive and constant time step strategies.

The impact of the time step strategy on the calculated aHRR is shown in Figures 3.26, 3.27 and 3.28. The results confirm that the spikes in the aHRR are numerical artifacts introduced by variations in the time step, rather than physical phenomena. Enforcing a constant time step significantly reduces these artificial oscillations. Nevertheless, some deviations remain in regions where automatic re-meshing occurs, which indicates that such spikes cannot be fully avoided but should be interpreted as numerical effects.

Furthermore, it was observed that the change in the time-step strategy also appears to influence the small peak associated with the diesel pilot combustion. In the constant time step simulation, this peak is slightly shifted compared to the adaptive case, suggesting a numerical sensitivity in the early stages of diesel ignition. In contrast, the main hydrogen combustion event remains unaffected, confirming that the global combustion process is robust regardless of the chosen time-step strategy.

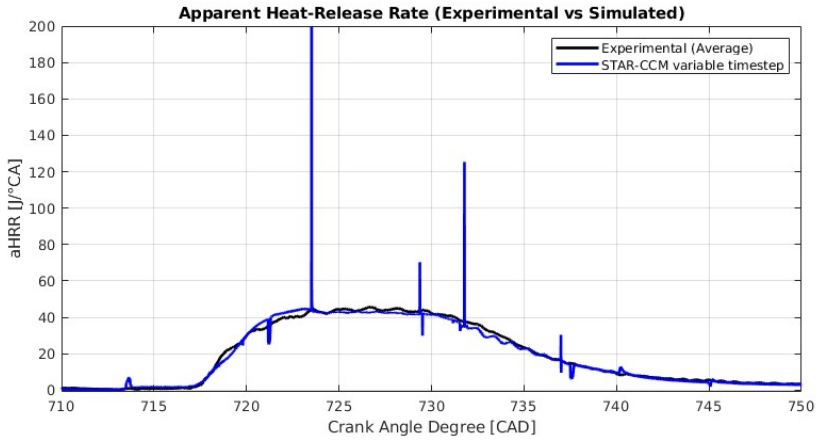

Figure 3.26: aHRR obtained with adaptive time step in Case 1 (A75).

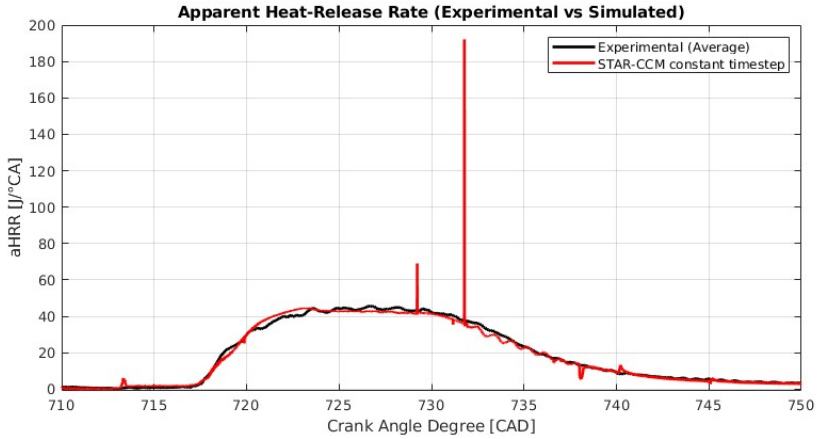

Figure 3.27: aHRR obtained with constant time step in Case 1 (A75).

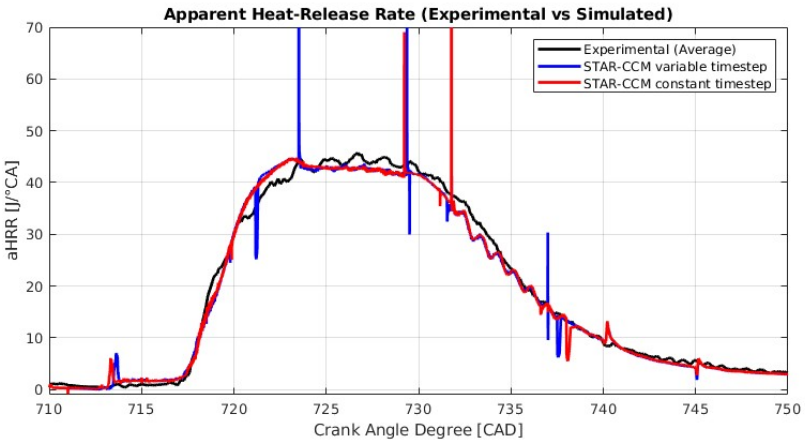

Figure 3.28: aHRR obtained with both time steps in Case 1 (A75).

3.5 Sensitivity to the Diesel Pilot Injection

As a final step in the analysis of Case 1, an additional simulation was carried out to further examine the influence of the diesel pilot on the combustion process. In this configuration, the total amount of injected diesel was reduced to 50% of the baseline case. This reduction was implemented by removing the initial portion of the diesel injection event while maintaining the same instantaneous mass-flow profile. Consequently, the overall injection duration was shortened by roughly half, although the reduction in timing is not exactly proportional to the fuel quantity decrease.

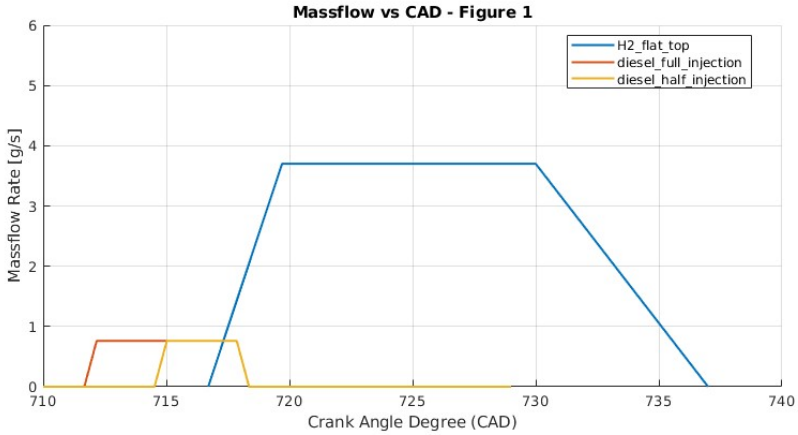

Figure 3.29: Injection curves 50% and original cases.

Figures 3.30 and 3.31 compare the cylinder pressure and aHRR traces between the best match of Case 1 and the 50% diesel case. The results show that the impact on the pressure evolution is minor, with both cases exhibiting almost identical trends throughout the cycle. However, the effect becomes more apparent in the aHRR. In the reduced-diesel case, a strong initial peak is observed at the onset of hydrogen combustion, which can be attributed to an increased degree of premixing of hydrogen prior to ignition. After this initial stage, the aHRR curve converges toward the baseline behavior, leading to a comparable overall combustion profile. A possible explanation can be that, as the diesel and hydrogen injectors have a 20-degree offset, the size of the diesel flame is smaller and therefore gives hydrogen more time to premix before the flame reaches the hydrogen and burns it.

These observations indicate that the amount of diesel pilot not only influences ignition stability but also affects the extent of premixing and the subsequent shape of the aHRR. While the global pressure development remains largely unchanged, the heat release dynamics become more sensitive, especially during the early phase of hydrogen combustion.

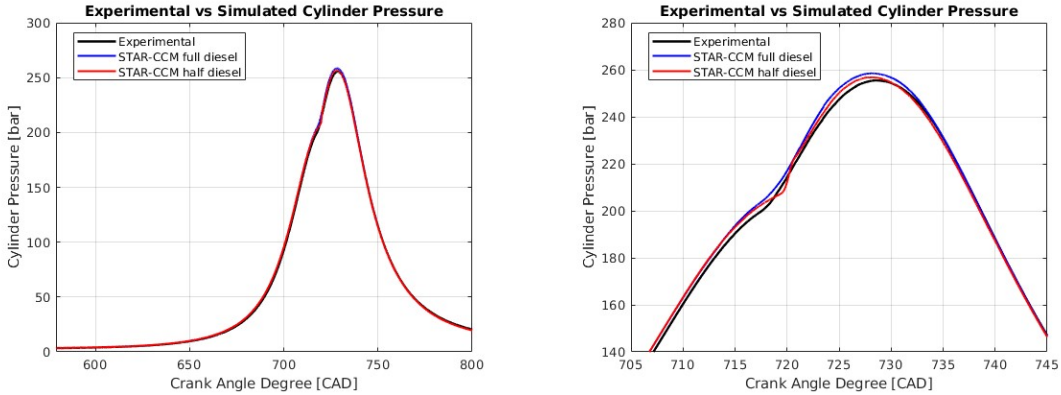

(a) 579 CAD to 800 CAD.

(b) 705 CAD to 745 CAD.

Figure 3.30: Comparison of pressure traces with different diesel pilot sizes.

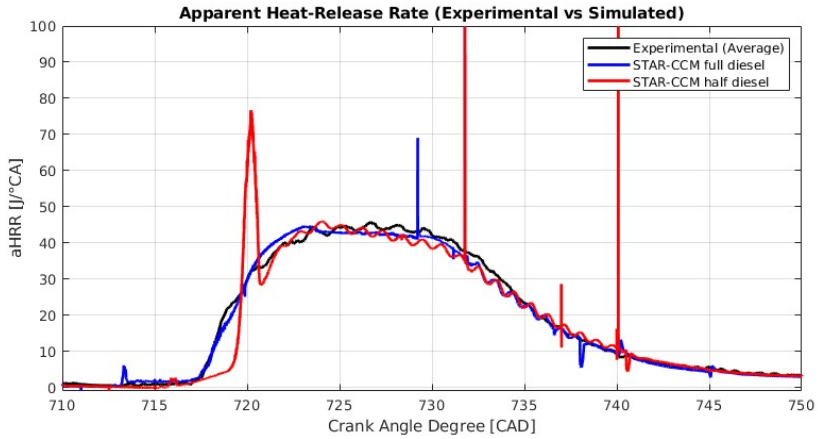

Figure 3.31: Comparison of aHRR traces with different diesel pilot sizes.

3.5.1 Effect of reducing the Diesel on the premixing and start of combustion

To further investigate the differences in ignition behavior between the original and the 50% diesel cases, Figures 3.32 to 3.35 visualize the spatial distribution of the hydrogen jet and diesel flame as well as temperature during the early phase of hydrogen combustion.

The first set of figures (3.32 to 3.34) shows planar cuts through the hydrogen injector, where the temperature is superimposed with contours of H2 and OH mole fractions. The H2 concentration illustrates the H2 jet, while the OH radical serves as a reliable indicator of the flame front, as it is a short-lived intermediate species formed at high temperatures in both diesel and hydrogen combustion. Therefore, regions with elevated OH concentration correspond to zones where active combustion is occurring.

In Figure 3.32 at 718.3 CAD, the original case shows the first signs of ignition, with localized regions of high OH concentration marking the onset of combustion. In contrast, the 50% diesel case exhibits no visible OH at this stage, indicating that hydrogen has not yet ignited. By 719.6 CAD, the first traces of OH appear in the 50% diesel case, signaling the beginning of the ignition process, while the flame in the original case is already more developed and expanding throughout the combustion chamber. Finally, at 720.6 CAD, the flame in the original case is fully established, whereas in the 50% diesel case it is still in the process of forming. This behavior confirms that the reduced diesel quantity delays hydrogen ignition, allowing a longer premixing period before combustion starts. Consequently, the ignition event in the 50% diesel case occurs more abruptly and is consistent with the sharp peak observed in the apparent heat release rate.

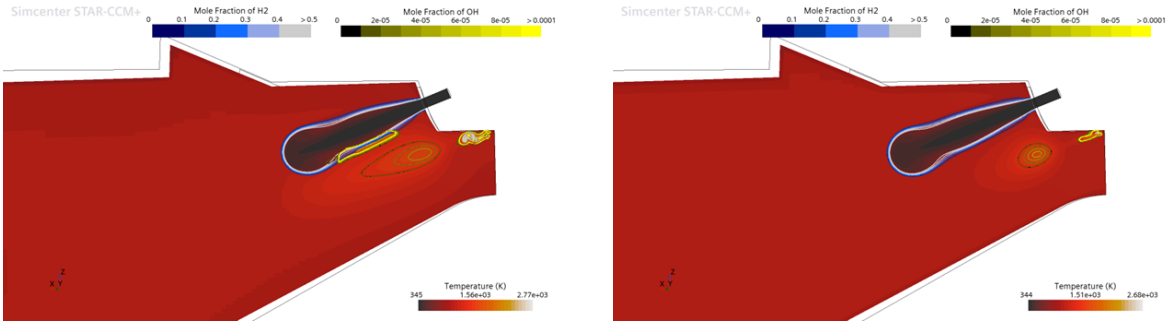

(a) Original Case 1 (A75). **(b)** 50% diesel case.

Figure 3.32: Temperature and isosurfaces of H2 and OH mole fractions at 718.3 CAD.

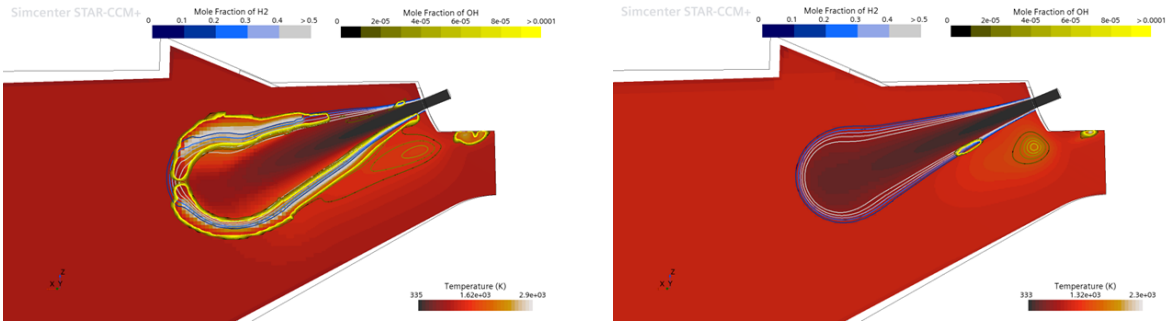

(a) Original Case 1 (A75). **(b)** 50% diesel case.

Figure 3.33: Temperature and isosurfaces of H2 and OH mole fractions at 719.6 CAD.

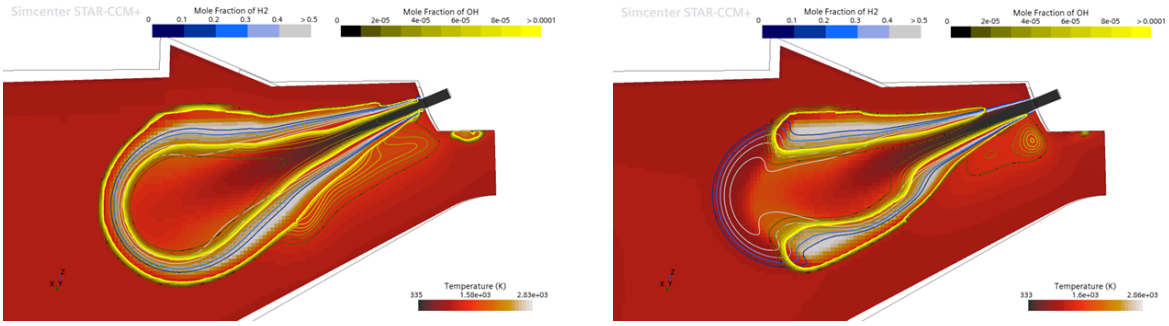

(a) Original Case 1 (A75). **(b)** 50% diesel case.

Figure 3.34: Temperature and isosurfaces of H2 and OH mole fractions at 720.6 CAD.

Figure 3.35 provides three-dimensional representations of the flame development at the onset of combustion for both operating conditions. Specifically, Figure 3.35a corresponds to the original case at 718.3 CAD, and Figure 3.35b to the 50% diesel case at 719.6 CAD, which represent the respective ignition moments for each case. The isosurfaces correspond to 0.1 H_2 and 4×10^{-4} OH mole fractions, both colored by temperature. These visualizations highlight that, in both cases, the OH distribution reveals no direct contact between the diesel flame front and the hydrogen jet. This suggests that hydrogen ignition is not triggered by direct flame propagation from the diesel pilot, but rather by secondary effects induced by the pilot combustion. Two possible mechanisms are considered: (i) the diffusion of reactive radicals generated in the diesel flame into the hydrogen-rich region, and (ii) the increase in local temperature caused by the nearby diesel combustion, which promotes the autoignition of hydrogen.

For completeness, the full sequence of 3D visualizations at 718.3, 719.6, and 720.6 CAD for both diesel fractions is included in the Appendix. These additional figures illustrate the progressive flame development and confirm that the same ignition patterns shown in the 2D figures are consistently observed.

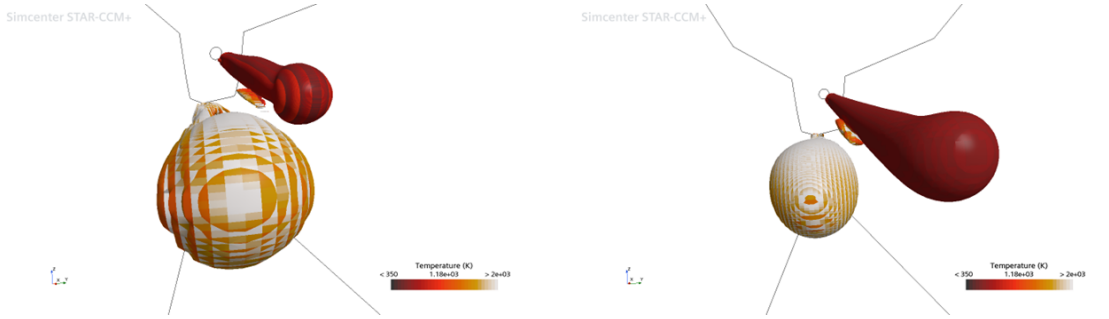

(a) Original Case 1 (A75) (718.3 CAD). **(b)** 50% diesel case (719.6 CAD).

Figure 3.35: Three-dimensional visualization of isosurfaces of 0.1 H2 and 4×10^{-4} OH, colored by temperature, at the start of ignition for both cases.

3.5.2 Analysis of Hydrogen Ignition Mechanisms

To gain deeper insight into the physical and chemical processes responsible for hydrogen ignition, this subsection examines the evolution of key thermochemical quantities during the moments leading up to the onset of combustion. The analysis focuses on the original case, since the same ignition mechanism is observed for the 50% diesel condition. For completeness, the corresponding visualizations for the 50% diesel case are included in the Appendix, together with comparative plots illustrating the evolution of temperature, OH, HO_2, and H_2O_2 concentrations around the ignition timing.

Figures 3.36–3.39 compare two instants: 718.0 CAD, corresponding to 0.2 CAD before the onset of ignition, and 718.2 CAD, the moment when OH first appears inside the hydrogen jet, marking the start of combustion. For all species fields except temperature, the background represents the chemical heat release rate, enabling a direct correlation between radical formation and exothermic activity.

The temperature contours in Figure 3.36 show that the region below the hydrogen jet, toward the diesel flame, is already significantly hotter than the rest of the chamber, with local temperatures of over 1300 K compared to roughly 1100 K elsewhere. This elevated thermal field originates from the nearby diesel combustion and provides the conditions necessary for hydrogen oxidation to begin. At this stage, small concentrations of OH are observed only near the diesel flame, not within the hydrogen jet itself, indicating that hydrogen has not yet ignited.

The OH distribution in Figure 3.37 further confirms this behavior. The first panel (718.0 CAD) shows that OH is confined to the vicinity of the diesel flame, while in the hydrogen region only traces of OH have been transported from the flame front. These traces slightly overlap with areas of localized chemical heat release, but their intensity is too low to account for the energy release observed there. In the second panel (718.2 CAD), as ignition begins, OH suddenly appears within the hydrogen jet, but without being linked to the high concentrations of the diesel flame, marking the transition from pre-ignition reactions to full combustion.

The source of the initial heat release can be explained by the formation of intermediate radicals. As shown in Figures 3.38 and 3.39, both HO_2 and H_2O_2 accumulate in the lower part of the hydrogen jet before OH appears. Among these, HO_2 dominates and is the first product of hydrogen oxidation at elevated temperature, forming through reactions between H_2 and O_2. The spatial correlation between these radicals and the heat-release zones demonstrates that hydrogen oxidation is already active there, even though OH levels remain negligible. Moreover, the concentrations of HO_2 and H_2O_2 are very low within the diesel flame itself and only appear at its origin, far from the hydrogen region, confirming that these intermediates are not transported from the diesel combustion zone.

This evidence indicates that the ignition of hydrogen is initiated by thermal autoignition in the hot region below the jet, where the local temperature increase accelerates the low-temperature oxidation pathway and leads to the formation of HO_2 and H_2O_2. Once these radicals are present, the small amount of OH that diffuses from the diesel flame may enhance or accelerate the final transition to ignition, but it is not the primary trigger. The appearance of heat release and oxidation intermediates in regions

where diesel-derived OH has not yet arrived clearly demonstrates that the main cause of ignition is the elevated temperature field rather than direct radical diffusion.

In summary, Figures 3.36 to 3.39 collectively show that hydrogen ignition occurs through a thermally promoted autoignition process initiated in the hot environment produced by the diesel pilot. The subsequent arrival of OH from the diesel flame may contribute to accelerating combustion, but the onset of hydrogen ignition originates independently within the heated hydrogen region.

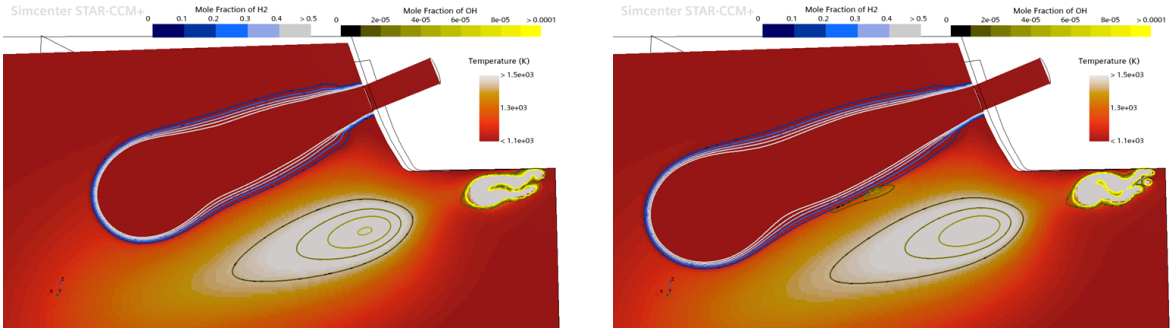

(a) 718.0 CAD - 0.2 CAD before ignition. **(b)** 718.2 CAD - start of ignition.

Figure 3.36: Contours of H2 and OH concentrations over a 2D temperature plot for the original Case 1 (A75).

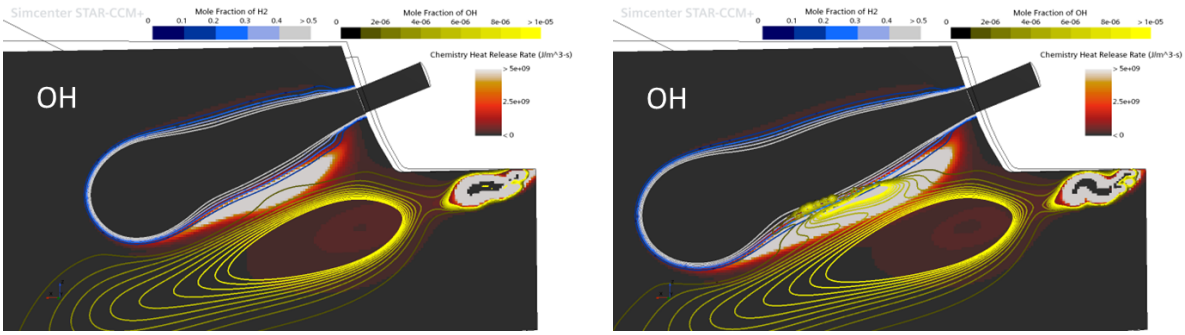

(a) 718.0 CAD - 0.2 CAD before ignition. **(b)** 718.2 CAD - start of ignition.

Figure 3.37: Contours of H2 and OH concentrations over a 2D chemical heat release plot for the original Case 1 (A75).

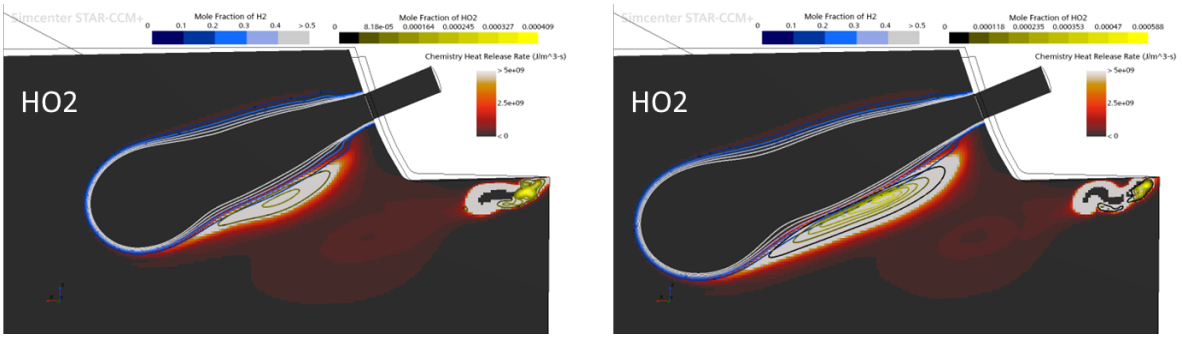

(a) 718.0 CAD - 0.2 CAD before ignition. **(b)** 718.2 CAD - start of ignition.

Figure 3.38: Contours of H2 and HO2 concentrations over a 2D chemical heat release plot for the original Case 1 (A75).

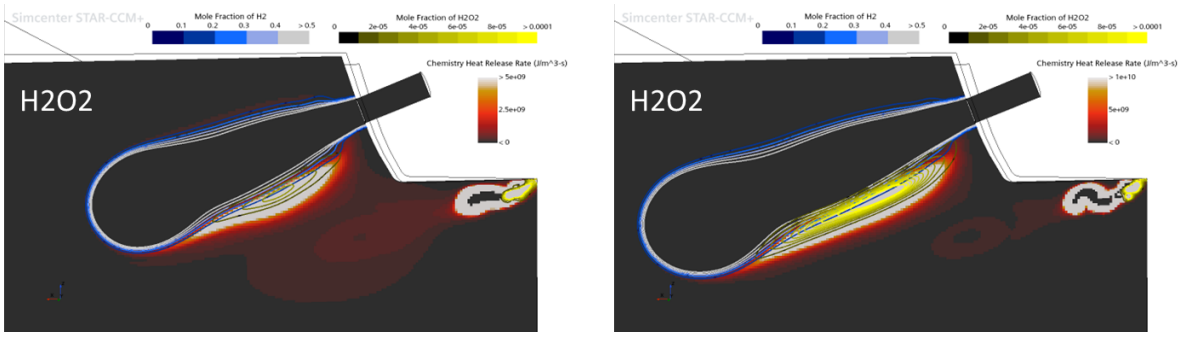

(a) 718.0 CAD - 0.2 CAD before ignition.

(b) 718.2 CAD - start of ignition.

Figure 3.39: Contours of H2 and H2O2 concentrations over a 2D chemical heat release plot for the original Case 1 (A75).

3.6 Discussion — Case 1 (A75)

Case 1 (A75) provides a clear insight into both the injection behavior and the fundamental ignition process in dual-fuel hydrogen operation. Two aspects dominate the discussion: (i) the physical mechanism controlling the hydrogen mass flow through the injector and (ii) the way this injection behavior shapes ignition and early combustion.

Evaluation of nozzle-flow theories. Two alternative injection models were investigated: convergent nozzle theory and the convergent–divergent nozzle theory. The comparison revealed that the pressure-driven, curved mass–flow profile predicted by the convergent nozzle theory could not reproduce the experimental heat-release trace. The simulated aHRR was too high and did not follow the same trend as the experiemental aHRR, yielding an overall energy release and pressure evolution inconsistent with measurements. Conversely, the flat-top injection inspired by the convergent–divergent approach produced a better agreement with both the magnitude and phasing of the measured aHRR and cylinder pressure.

Interpretation of the limiting mechanism. The improved agreement obtained with the flat-top injection profile suggests that the hydrogen flow undergoes an effective restriction that limits the mass flow rate. A straightforward interpretation is that choking could occur at an internal throat of the injector. For the measured peak rate of 3.7 g/s, the maximum cylinder pressure that would still allow choked flow is approximately 270 bar, which is indeed satisfied under the present operating conditions. However, there is no conclusive evidence that choking is the actual cause of the restriction. Other aerodynamic phenomena, such as boundary-layer separation or internal recirculation within the nozzle, could equally well reduce the effective flow area and produce the observed limitation. To distinguish between these possibilities, an additional case with lower in-cylinder pressure is analyzed in the next chapter.

Quantitative correlation with combustion. A clear proportionality was observed between the hydrogen injection rate and the apparent heat-release rate (aHRR), with the aHRR following the injection profile almost directly and only a short delay of about 1–1.5 CAD. This indicates that combustion occurs nearly instantaneously after injection, confirming that the process is largely injection-controlled. The ratio between aHRR and mass-flow rate remains approximately constant, around 11.5 J s/(g CAD), equivalent to a specific energy release of roughly 83 MJ/kg of hydrogen—about 27% lower than its theoretical lower heating value, reflecting typical thermal losses and delayed energy conversion. This strong coupling validates the use of aHRR as a reliable indicator of the underlying injection dynamics.

Ignition and flame development. The ignition of hydrogen in the dual-fuel configuration does not result from direct contact between the diesel and hydrogen flames, but rather from the thermal and chemical environment created by the diesel pilot. The heat released during pilot combustion elevates the local temperature around the hydrogen jet, initiating the formation of intermediate radicals such

as HO_2 and H_2O_2. These species gradually accumulate until their decomposition triggers autoignition within the hydrogen region. Although some radicals originating from the diesel flame may contribute to accelerating this process, the evidence indicates that the primary ignition mechanism is thermally promoted autoignition of hydrogen, followed by rapid flame growth once critical conditions are reached.

Premixing and flame characteristics. A noticeable premixed phase is only observed in the 50% diesel case, where the reduced pilot quantity delays ignition and allows limited hydrogen–air mixing before combustion starts. This short premixed stage produces the sharp initial spike in the apparent heat-release rate. In contrast, the original case ignites almost immediately, leaving virtually no time for premixing. After ignition, combustion in both cases rapidly transitions to a diffusion-controlled regime, with a predominantly laminar flame structure sustained by the high diffusivity and fast reaction kinetics of hydrogen.

Sensitivity and robustness. Parametric variations confirm that the global combustion sequence is robust. Lowering the turbulent Schmidt number (0.9 to 0.5) enhances mixing and slightly increases early aHRR, while adding 5% EGR weakens the initial spike. Switching from TFSC to LFC yields a more stable and physically consistent aHRR shape, confirming that the dynamic flame-speed formulation better captures the dual-fuel regime. Numerical tests also confirmed that artificial spikes in aHRR were tied to time-step or remeshing artifacts and do not affect the overall solution.

Chapter 4

Results and Discussion: Case 5 560HP

4.1 Differences Between Experimental Cases

As it was introduced before, the two selected experimental datasets correspond to operation at approximately 75% load, but they differ in injection strategies and boundary conditions. As a result, both cases achieve comparable torque and power output, yet they follow distinct combustion pathways. This makes them particularly suitable for a side-by-side analysis: while they can be considered equivalent in terms of overall engine performance, their injection timing and fuel distribution introduce relevant differences in combustion development.

Table 2.2 already summarized the main operating parameters of the two cases. To complement this, Figures 4.1 and 4.2 directly compare the experimental pressure traces and apparent heat release rate (aHRR). In both plots, the curves from the two datasets are superimposed to highlight their divergence.

The pressure comparison reveals that, despite the same load condition, combustion phasing is shifted as a direct consequence of the different injection timings. Similarly, the aHRR curves indicate that not only the total amount of fuel but also its temporal distribution vary between the cases. These observations emphasize that the two datasets should not be regarded as repetitions of a single operating point. Instead, they represent complementary conditions at the same load level, providing a broader experimental basis for CFD validation and offering valuable insight into how injection strategy influences the combustion process.

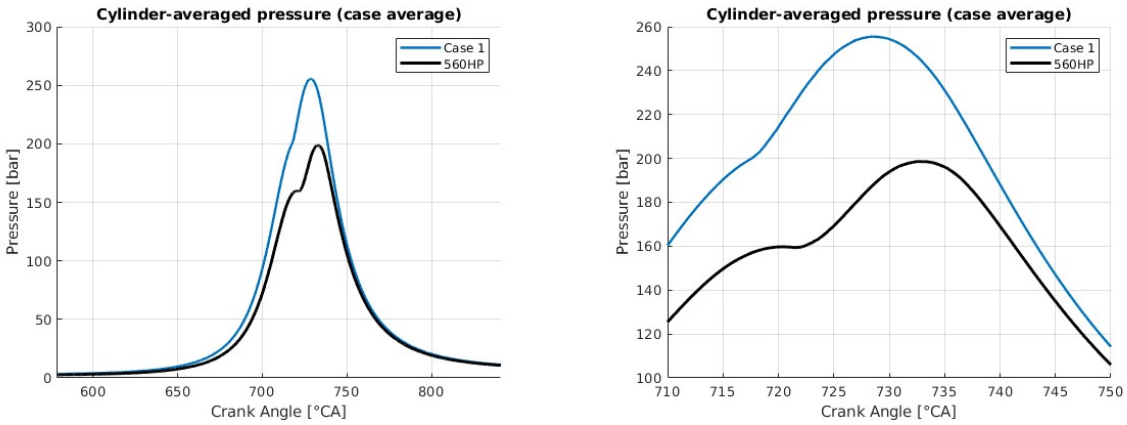

(a) 579 CAD to 841 CAD.

(b) 710 CAD to 750 CAD.

Figure 4.1: Comparison of in-cylinder pressure between the two 75% load cases.

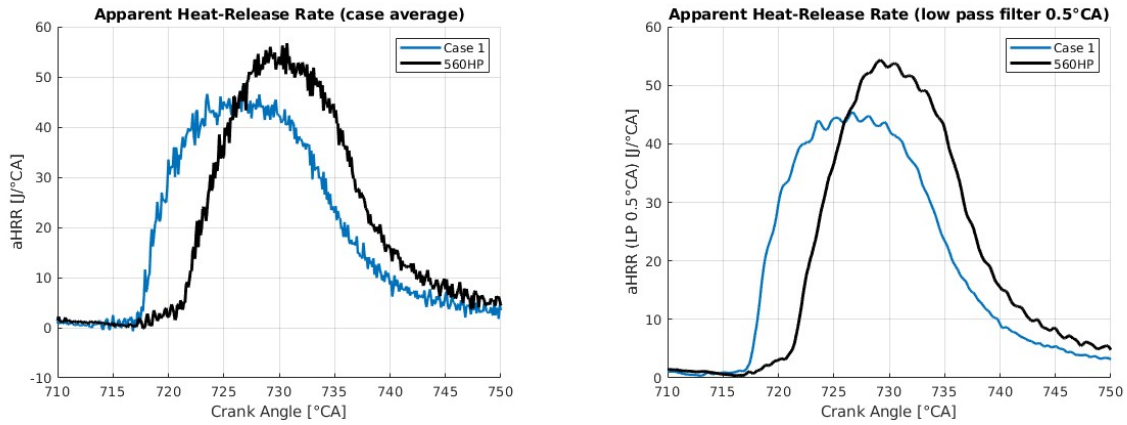

(a) Unfiltered signal.

(b) Filtered signal.

Figure 4.2: Comparison of aHRR between the two 75% load cases.

4.2 Convergent Nozzle Theory Applied to Case 5 (560HP)

In the previous analysis (Case 1, A75 dataset), the injection mass flow was derived using both isentropic convergent and convergent-divergent nozzle theories, based on the experimentally measured rail pressure and the instantaneous in-cylinder pressure. The same methodology is now applied to Case 5 from the 560HP dataset. In this section the results of applying convergent nozzle theory are presented.

In this section several discharge coefficients (C_d) have been tested with the aim of finding out which aligns more closely with the experimental results. Specifically, values of $C_d = 0.85$, 0.80, and 0.75 are considered. For each assumed coefficient, a theoretical injection mass flow curve is obtained. Figure 4.3 shows the resulting injection curves for the three discharge coefficients. As expected, a reduction in the discharge coefficient leads to a lower peak mass flow rate and a slightly delayed injection profile. Another relevant observation is that compared to the injection curves obtained using convergent nozzle theory in Case 1 A75, this case has a much horizontal upper boundary, this is because the cylinder pressure is considerably lower and therefore the flow is closer to the critical conditions in the nozzle, making it less sensible to pressure changes.

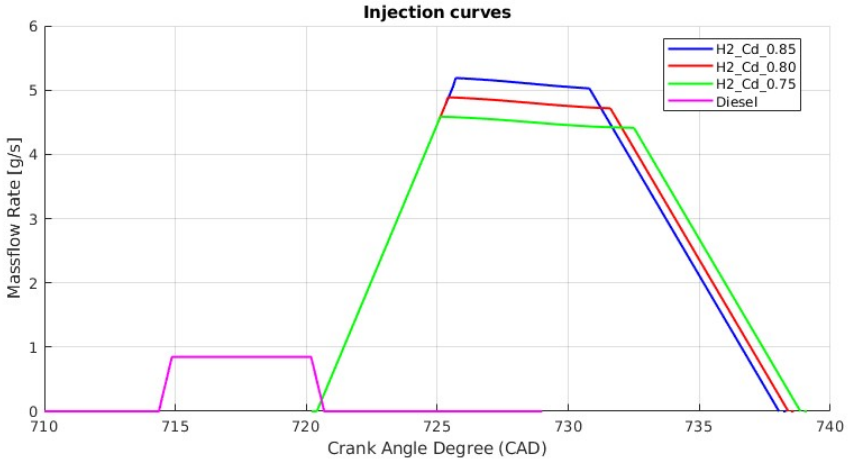

Figure 4.3: Comparison of theoretical injection mass flow curves for Case 5 (560HP) at different discharge coefficients.

The impact of these injection profiles on the combustion process is illustrated in Figures 4.4 and 4.5, where the corresponding in-cylinder pressure traces and apparent heat release rates (aHRR) are presented. These results highlight the sensitivity of the pressure evolution and combustion phasing to the assumed discharge coefficient.

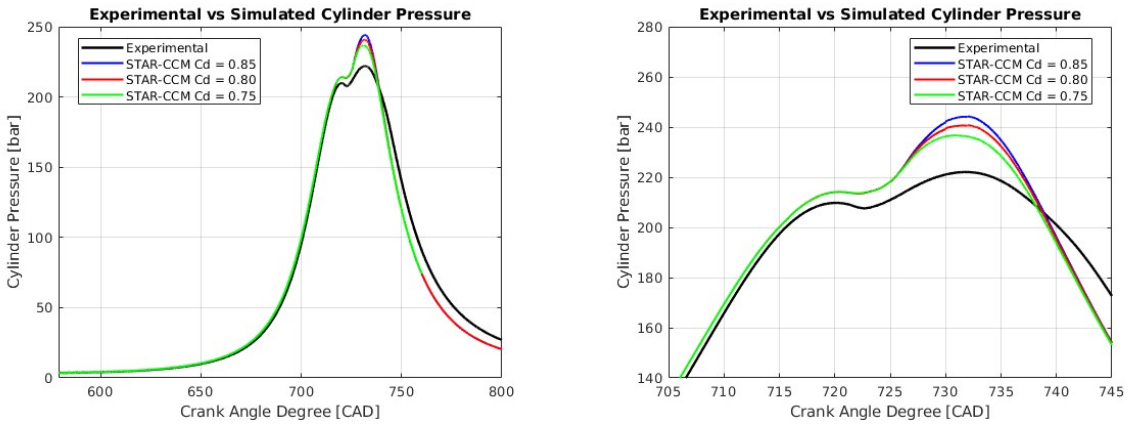

(a) 579 CAD to 841 CAD.

(b) 705 CAD to 745 CAD.

Figure 4.4: Comparison of in-cylinder pressure between the three injection curves (Cd 0.85, 0.80 & 0.75).

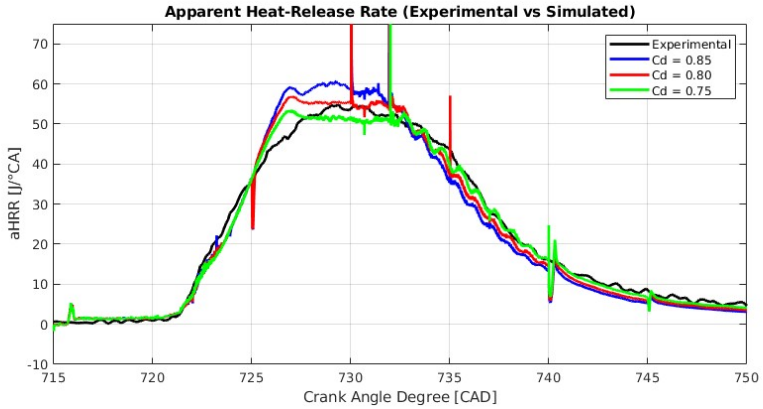

Figure 4.5: Comparison of aHRR between the three injection curves (Cd 0.85, 0.80 & 0.75).

Unlike in Case 1 (A75), where the convergent-nozzle formulation largely failed to reproduce the injected mass and combustion evolution, Case 5 (560HP) shows a considerably closer agreement. With a discharge coefficient around $C_d = 0.80$, the predicted aHRR can be regarded as physically plausible. The main deviation in the aHRR seems to be that it shows a very sharp and almost trapezoidal rise, while the experimental trace has a more rounded onset. This discrepancy could be attributed either to limitations of the combustion model, which might be burning the hydrogen faster than it should, or to injector dynamics that are not fully captured, since the real needle lift and closure process do not produce perfectly abrupt edges. In any case, the difference is not as fundamental as in Case 1, and the convergent-nozzle prediction could not be discarded if this was the only case taken into consideration. The in-cylinder pressure traces show a slightly higher peak in the simulations, which can be explained by the larger fraction of fuel burned early in the cycle; however, the pressure evolution is less informative than the heat-release shape, where the main mismatch becomes evident.

4.3 Convergent–Divergent Nozzle Theory Applied to Case 5 (560HP)

In addition to the analysis performed with different discharge coefficients, two alternative flat-top injection curves were evaluated for Case 5 (560HP). The objective is to investigate how plausible would be to obtain the injection using the the convergent-divergent theory that has previously been used in Case 1 (A75). These injections provide further insight into the sensitivity of the model and serve as exploratory scenarios for improving the agreement between theory and experiment.

4.3.1 Case 1 (A75) Injection Curve Applied to Case 5 (560HP)

In this initial approach, the theoretical injection curve obtained for Case 1 (A75) is directly applied to Case 5 (560HP). The reasoning behind transferring the curve without modifications is that, if the flow is constrained by a physical limitation in the injector, specifically, if choking occurs, the mass flow rate will remain constant across all cases operating under the same rail pressure conditions. Since the rail pressures in these two cases (302.5 bar vs. 299 bar) are practically equivalent, and the cylinder pressure is considerably lower, the same injection curve can be assumed to hold.

Figure 4.6 shows the adapted injection curve compared with the original Case 5 profile. The corresponding in-cylinder pressure and aHRR traces are presented in Figures 4.7 and 4.8. The results show strong deviations from the experimental results meaning that the injection curve that successfully matched the results in Case 1 (A75) unfortunately is not the injection curve that was used in Case 5 (560HP). This discards the idea that a physical throat inside the injector is responsible for the choking if the flow in Case 1 (A75).

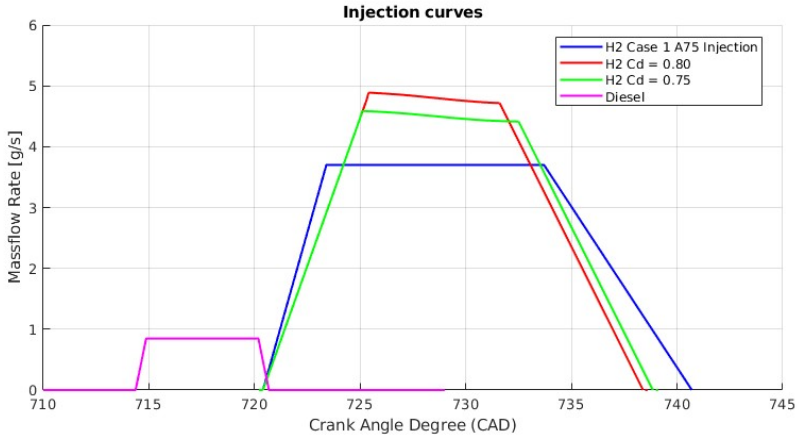

Figure 4.6: Injection curve from Case 1 (A75) applied to Case 5 (560HP).

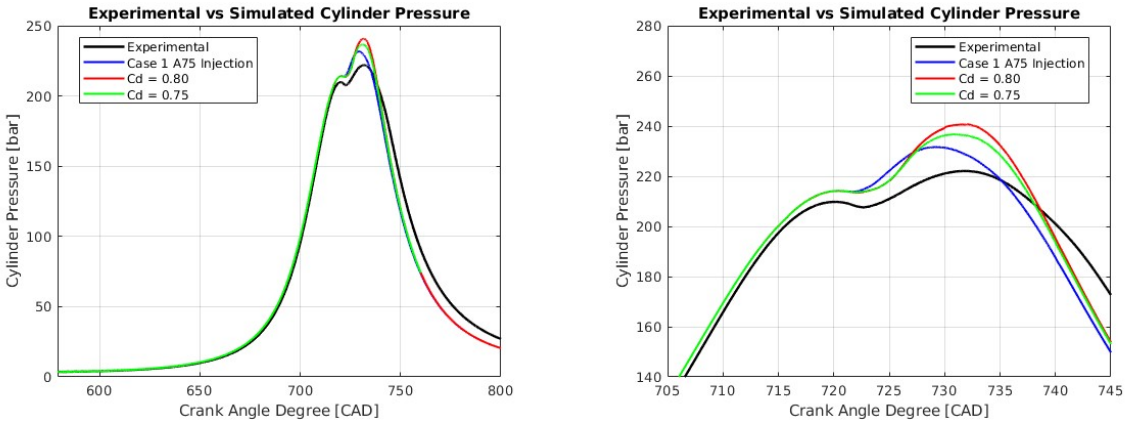

(a) 579 CAD to 841 CAD.

(b) 705 CAD to 745 CAD.

Figure 4.7: Comparison of in-cylinder pressure between the injection from the Case 1 (A75) and the injections obtained with convergent nozzle.

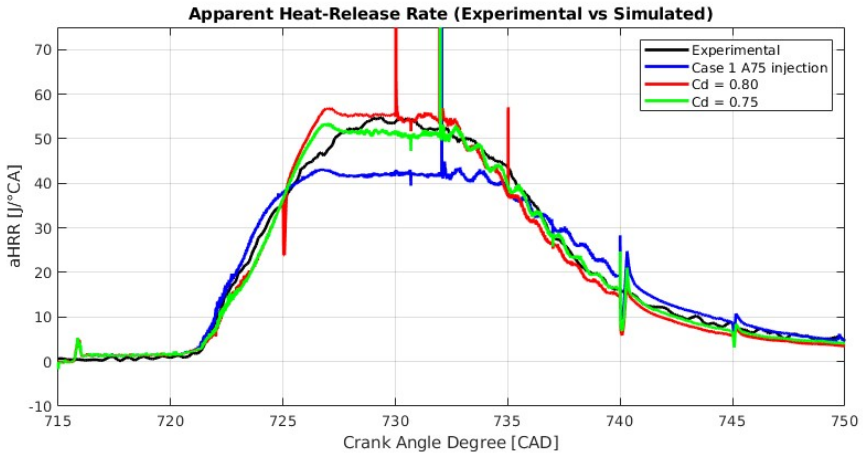

Figure 4.8: Comparison of aHRR between the injection from the Case 1 (A75) and the injections obtained with convergent nozzle.

4.3.2 New Flat-Top Injection Curve

In the previous section, it was demonstrated that the injection limitation is unlikely to be a fundamental physical constraint, since otherwise the mass flow rate would remain identical across cases with comparable rail pressures. Nevertheless, other mechanisms could still account for the observed behavior, for instance, a reduced effective flow area caused by boundary-layer growth, recirculation, or some form of variable geometry. However, according to Cespira, a variable geometry is considered unlikely.

A second approach consists of constructing a new flat-top injection curve specifically for Case 5 (560HP), following the same procedure previously applied to Case 1 (A75). The resulting injection profile is presented in Figure 4.9, while the corresponding in-cylinder pressure and apparent heat release rate (aHRR) are shown in Figures 4.10 and 4.11. The results show that the flat-top injection produces a similar behavior to that obtained with the convergent nozzle theory. In particular, the aHRR exhibits an initial overestimation at the onset of combustion, but this feature is already present in the other cases and the overall differences between the three profiles are minimal.

The comparison of results therefore indicates that the flat-top curve yields outcomes broadly consistent with those obtained using the convergent nozzle theory. This similarity arises because the relatively low in-cylinder pressures in this case flatten the injection profile, making it closely resemble the constructed flat-top curve, as also illustrated in Figure 4.9. Consequently, only from the analysis in Case 5 (560HP) no clear conclusion can be drawn regarding the superiority of either approach, since both produce comparable and acceptable results.

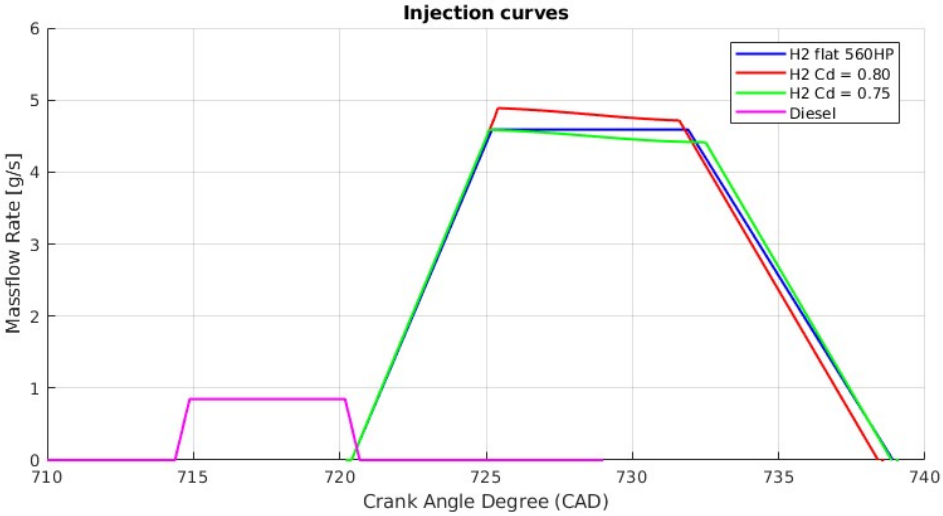

Figure 4.9: Proposed flat-top injection curve for Case 5 (560HP) compared with the experimental profile.

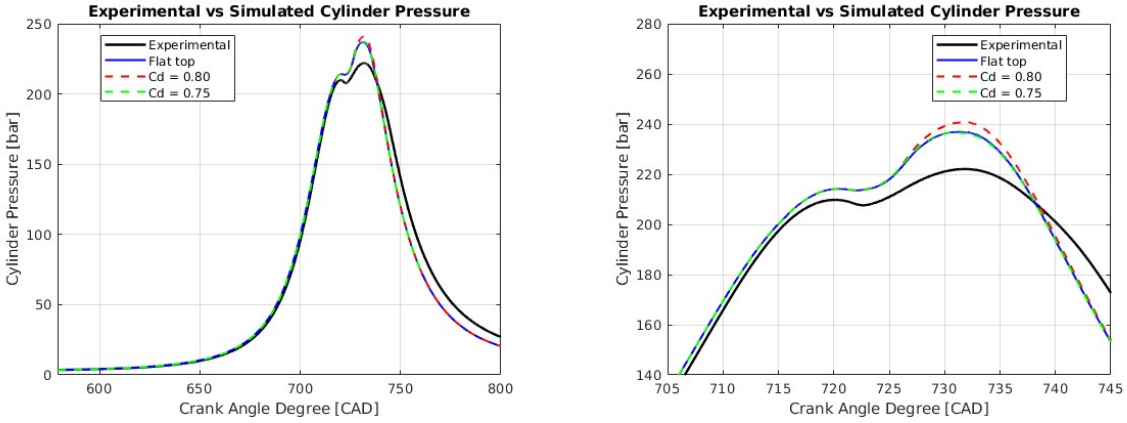

(a) 579 CAD to 841 CAD.

(b) 705 CAD to 745 CAD.

Figure 4.10: Comparison of in-cylinder pressure between the new ”Flat-Top injection” and the injections obtained with convergent nozzle.

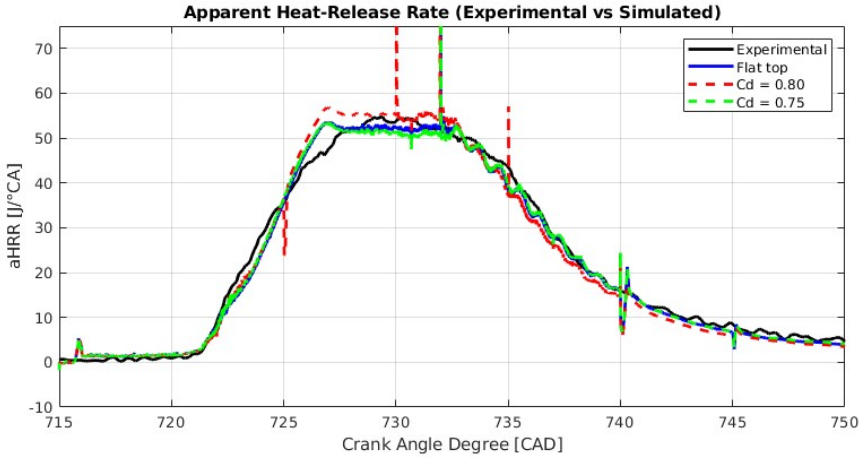

Figure 4.11: Comparison of aHRR between the new ”Flat-Top injection” and the injections obtained with convergent nozzle.

4.4 Discussion — Case 5 (560HP)

Case 5 explores the same injection model under a different pressure regime, offering a complementary validation of the proposed flow-limitation mechanism and its effect on combustion. The lower in-cylinder pressure during injection provides a useful contrast to Case 1.

Comparison of nozzle theories. At this operating point, the convergent and convergent–divergent models both produce almost identical near–flat-top mass–flow profiles. The lower backpressure brings the injector closer to critical conditions, naturally flattening the curve without the need to invoke choking. Based solely on this case, the convergent nozzle theory could not be conclusively ruled out, as its predictions are not in strong disagreement with the measurements. However, when these results are considered together with the findings from Case 1, and given that the match achieved here is still imperfect, and certainly not superior to that obtained with the flat-top profile, the convergent nozzle approach can be reasonably discarded as a valid explanation of the injector behavior.

Pressure-dependent limitation. The key finding from Case 5 is that, despite similar rail pressures (302.5 bar vs. 299 bar), the injected mass is substantially higher than in Case 1. If a fixed geometric restriction were controlling the flow, both cases would exhibit similar curves. The fact that the mass flow increases when cylinder pressure decreases confirms that the restriction is pressure-dependent, not geometric. This supports the interpretation that internal aerodynamic effects, such as boundary-layer separation or recirculation, limit the flow when the pressure ratio is high, but diminish as the ratio decreases. Consequently, the injector behavior resembles that of a convergent–divergent nozzle only in a phenomenological sense: the limiting mechanism is dynamic and driven by internal flow physics rather than a fixed throat.

Correlation with combustion behavior. Although the general correlation between the injection rate and the aHRR remains evident, the detailed shape of the simulated aHRR deviates from the experimental trend. The simulations predict a sharper rise and flatter plateau, whereas the experimental trace displays a smoother increase and a more rounded peak. Based on the previous analysis, it appears more reasonable to attribute this mismatch to inaccuracies in the assumed injection profile rather than to combustion modeling. A lower combustion intensity during the initial phase, as discussed in the previous chapter, would allow greater premixing and produce the kind of spike that is not observed here. If the flow limitation inside the injector originates from boundary-layer separation rather than true choking, it is plausible that the injection curve is not perfectly flat and that its shape varies with pressure. Nevertheless, the possibility remains that the combustion model itself is not fully capturing the flame development, which would also affect the validity of the previous results.

Implications for injection modeling. Case 5 therefore reinforces the main conclusions from Case 1: the convergent nozzle theory does not capture the experimental trends, while the convergent–divergent framework provides a better fit. However, the results also show that choking is not strictly required to explain the observed plateau. Instead, the findings favor a model based on a pressure-sensitive effective area linked to internal flow separation. The correlation between injection and aHRR remains valid, further supporting the practical inverse method for reconstructing injection profiles from measured heat release.

Chapter 5

Results and Discussion: Hydrogen-only Case

5.1 Autoignition Behavior of Hydrogen

The hydrogen-only case was derived from Case 1 (A75) by removing the diesel pilot injection. In this configuration, the hydrogen injector follows a flat-top injection profile that starts at 716.7 CAD. This setup was designed to provide a reference scenario for ignition in the absence of a pilot fuel and to assess whether numerical artifacts observed in the dual-fuel simulations affect the prediction of combustion onset.

Figures 5.1 and 5.2 show the in-cylinder pressure and aHRR traces for the hydrogen-only case. In the absence of a diesel pilot, combustion starts approximately 1.8 ms after the start of injection. Strictly speaking, this time interval represents the delay between the beginning of hydrogen injection and the onset of combustion, rather than the true chemical ignition delay. The latter would correspond to the period between the moment when a locally combustible hydrogen–air mixture is formed and the actual start of ignition; however, this distinction is practically negligible here, as hydrogen mixes very rapidly and the injection process makes the exact mixture-formation timing difficult to define. The observed delay is therefore considered representative of the overall ignition behavior. This value is consistent with previous findings in the literature [48] and illustrates why an auxiliary ignition source is typically required in hydrogen-fueled CI engines. During this delay, a large amount of hydrogen–air mixture accumulates, leading to a much higher degree of premixing than in normal operation. Once ignition begins, the combustion proceeds with a very fast, laminar flame that consumes the mixture almost instantaneously. As a result, the accumulated premix releases its energy in a single, abrupt event, producing a sharp aHRR peak and a steep pressure rise. This inherently unstable combustion behavior explains why an external ignition trigger, such as a diesel pilot, a spark, or a catalytic igniter, is required to initiate combustion earlier and thereby moderate the heat-release rate.

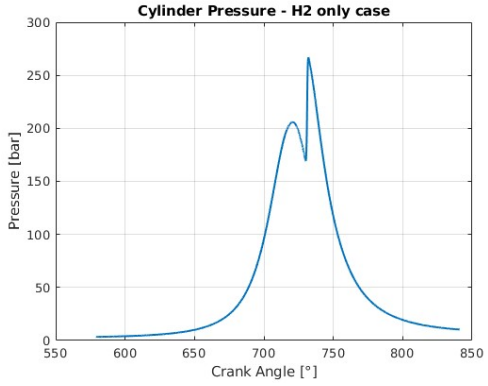

(a) 579 CAD to 841 CAD.

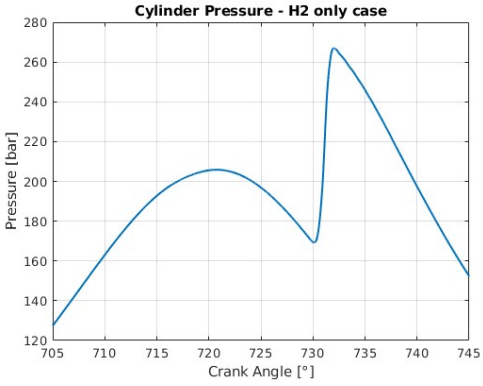

(b) 705 CAD to 745 CAD.

Figure 5.1: Hydrogen-only case in-cylinder pressure.

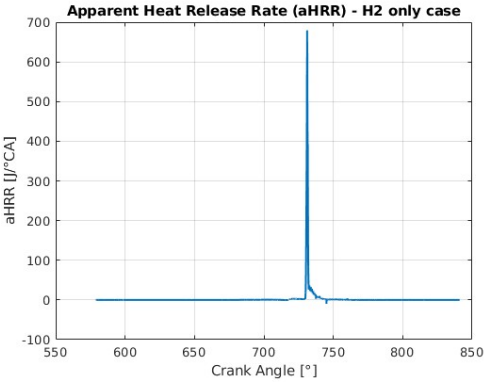

(a) 579 CAD to 841 CAD.

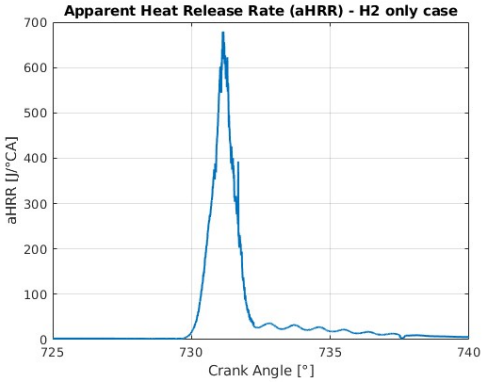

(b) 725 CAD to 740 CAD.

Figure 5.2: Hydrogen-only case apparent Heat Release Rate.

5.2 Effect of Time Step Strategy on the H2-only results

In Case 1 (A75), it was demonstrated that spurious spikes in the aHRR signal were introduced by variations in the time step, and could be minimized by enforcing a constant time step. A similar concern arises for the hydrogen-only case: since ignition delay is much longer and ignition is highly sensitive, there was a risk that numerical errors could artificially trigger or influence the autoignition process.

Figure 5.3 and Figure 5.4 compare the aHRR traces for the two time step strategies. As in the dual-fuel case, spikes are visible in the changes of time-step or mesh, for example at 732 CAD. However, in both cases the ignition delay remains unchanged, and the onset of combustion occurs at the same crank angle. Therefore, the comparison confirms that the spikes do not influence the onset of autoignition. They appear only after combustion has already started, and therefore cannot be considered a trigger for ignition.

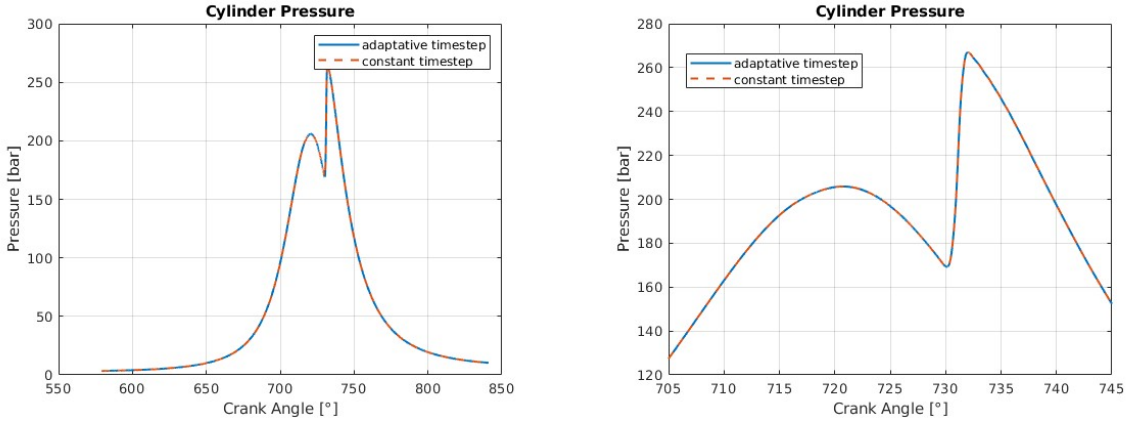

(a) 579 CAD to 841 CAD.

(b) 705 CAD to 745 CAD.

Figure 5.3: Hydrogen-only case in-cylinder pressure.

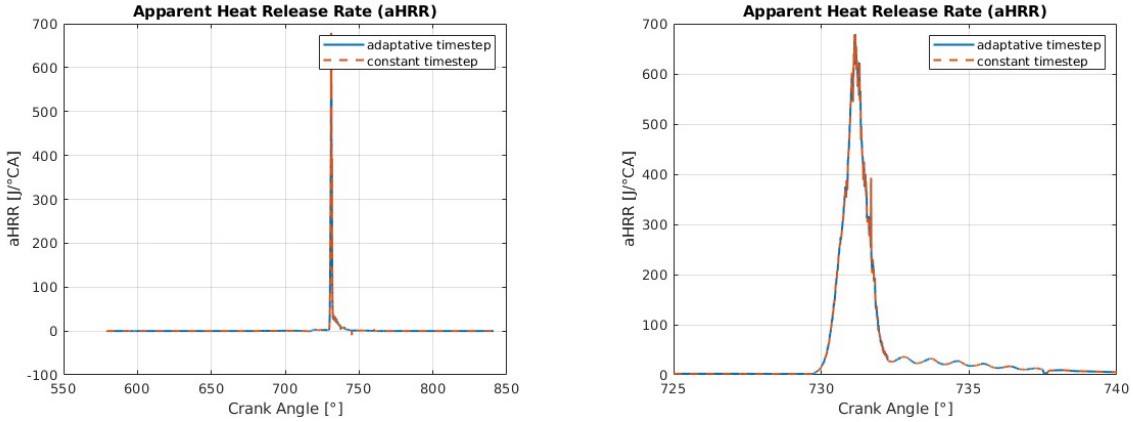

(a) 579 CAD to 841 CAD.

(b) 725 CAD to 740 CAD.

Figure 5.4: Hydrogen-only case apparent Heat Release Rate.

5.3 Discussion — Hydrogen-Only Case

The hydrogen-only configuration suppresses the diesel pilot to isolate the intrinsic chemical and physical behavior of hydrogen autoignition. This case serves as a reference both for validating the chemical mechanism and for assessing the numerical robustness of the CFD framework.

Autoignition behavior. In the absence of a pilot, hydrogen ignition is entirely self-sustained and depends on the ambient thermodynamic conditions. The simulations predict an ignition delay of approximately 1.8 ms, measured from the start of injection to the first rise in aHRR. This delay is consistent with reported data in the literature for comparable temperature and pressure ranges [48], confirming that the reaction mechanism and temperature dependence are physically realistic. The long delay allows extensive premixing, after which combustion occurs abruptly, producing a sharp aHRR spike and a rapid pressure rise.

Numerical robustness. Numerical artifacts observed in the aHRR (spikes) are confirmed to originate from the time step strategy and remeshing, as shown in Case 1. For hydrogen-only operation, these artifacts do not affect ignition delay or the physical onset of combustion. Instead, they appear only during the combustion phase and can be minimized by enforcing a constant time step.

Relevance to dual-fuel cases. Comparing this reference case with the dual-fuel configurations highlights the diesel pilot's essential role. Without it, ignition is delayed and combustion occurs explosively once autoignition conditions are reached. With the pilot, local heating promotes hydrogen autoignition earlier and distributes the heat release more gradually. The hydrogen-only results therefore support the interpretation that dual-fuel ignition is thermally promoted rather than radical-driven, and they confirm that the underlying chemistry in the model produces physically reasonable ignition delays and flame initiation.

Chapter 6

Conclusions, Limitations and Future Work

6.1 Conclusions

6.1.1 Thesis objectives and motivation

This thesis addressed the challenges of modeling hydrogen direct injection in a dual-fuel compression ignition engine with a small diesel pilot. The main objective was to develop a CFD model capable of reproducing the experimentally observed in-cylinder pressure and apparent heat-release rate (aHRR) traces, thereby enabling predictive simulations for engine design and optimization. The goal was to achieve a physically consistent model that could accurately describe the interaction between injection, ignition, and combustion processes in hydrogen–diesel dual-fuel operation.

Throughout this work, it became evident that the combustion response is predominantly governed by the injected hydrogen mass flow. Hydrogen combusts almost immediately after injection, leaving little time for premixed combustion. Consequently, the shape and dynamics of the injection profile emerged as the most critical factors to capture. However, because the experimental injection curves were not available, the injected mass flow had to be inferred from theoretical, numerical, and indirect experimental information. The complex dependence of mass flow on in-cylinder pressure, rail pressure, and internal nozzle geometry motivated the application of simplified nozzle-flow theories to reconstruct physically consistent injection curves.

6.1.2 Injection Modeling

The first set of analyses focused on understanding the mechanism controlling hydrogen flow through the injector. Two simplified approaches were evaluated: the Convergent Nozzle Theory and the Convergent-Divergent Nozzle Theory.

In Case 1 (A75), the purely convergent model produced a curved, pressure-dependent mass-flow profile that failed to reproduce the experimental pressure and aHRR trends. The predicted injection rate decreased with increasing backpressure, contrary to the nearly constant rate observed experimentally. In contrast, the flat-top profile inspired by the convergent-divergent framework resulted in a much better agreement with the experimental data, both in terms of combustion phasing and peak pressure. This suggested that a restriction might exist inside the injector that limits the flow in a manner consistent with a convergent–divergent configuration, leading to an almost constant injection rate. However, since this observation was based on a single operating point, it could not be considered conclusive, motivating a second analysis under different operating conditions.

When analyzing Case 5 (560 HP), the lower in-cylinder pressures of Case 5 makes both the convergent nozzle theory, with a discharge coefficient of $C_d \approx 0.8$, and the flat-top injection curve derived from the aHRR produce similar injection profiles. Therefore, this case does not provide substantial additional insight beyond what was already observed in Case 1, where the purely convergent nozzle theory had been ruled out. The similarity between both approaches here simply reflects that, under these lower backpressure conditions, the flow operates closer to the critical regime where the differences between the two theoretical formulations become minimal. Given that both cases shared similar rail pressure (≈ 300 bar) and nozzle geometry, this indicated that the internal restriction could not be purely geometric, if it were, the behavior would remain consistent across cases. This result pointed toward the existence of a variable flow limitation that depends on the operating conditions rather than a fixed nozzle throat.

Such variability cannot be explained solely by Convergent-Diverngent Nozzle Theory. Instead, it is more plausible that it has an aerodynamic nature, potentially caused by transient phenomena such as boundary-layer separation within the nozzle or at the sac-nozzle transition. These effects would alter the effective flow area as pressure conditions evolve, producing an apparent limitation in mass flow even without geometric choking.

Furthermore, even when using a flat-top mass-flow assumption, the experimental profiles displayed a slightly rounded shape near the top, which could not be entirely reproduced by the simplified nozzle theories. Although this could partly arise from minor inaccuracies in the combustion model, such as small deviations in fuel–air mixing that could enhance the heat release, the rounded behavior is also consistent with a time-dependent restriction during injector opening and closing. Considering that the

combustion model reproduces most other aspects satisfactorily, a dynamically varying aerodynamic restriction appears the most physically consistent interpretation.

An important outcome of this work is the quantitative correlation identified between the hydrogen mass-flow rate and the apparent heat-release rate (aHRR). The two quantities exhibit nearly identical temporal profiles, with only a small delay of approximately 1-1.5 CAD between injection and combustion. This relationship demonstrates that hydrogen combustion is strongly injection-controlled. The ratio between aHRR and injection rate was found to remain approximately constant, with an average proportionality factor of 11.5 J s/(g CAD). This corresponds to an effective specific energy release of about 83 MJ/kg of hydrogen, approximately 31% lower than the theoretical lower heating value (120 MJ/kg). This difference reflects typical heat losses and delayed energy conversion in the combustion chamber. The correlation therefore provides a physically meaningful link between fuel delivery and energy release, allowing the aHRR to be used as a practical diagnostic for reconstructing injection curves.

Using this relationship, a semi-empirical method was developed to infer hydrogen injection profiles directly from experimental aHRR data. For Case 1, this approach yields a flat-top mass-flow rate of approximately 3.7 g/s with a duration of 20 CAD, while for Case 5 the peak reaches 4.6 g/s. The corresponding start of injection (SOI) timings, 716.7 CAD and 720.5 CAD, respectively, define a realistic operational range where the same proportionality factor can be applied to reconstruct physically consistent injection curves. The plateau duration determines the total injected mass, which can be adjusted depending on the target energy release.

Industrial validation with Cespira (formerly Westport Fuel Systems) confirmed that these injection durations and flow magnitudes are consistent with the company's internal data. Their typical injector opening and closing durations (0.4–0.6 ms and 0.7–1 ms, respectively) agree closely with the CFD-derived estimates. Cespira also reported observing nearly flat mass-flow curves under high-pressure conditions, consistent with the results obtained here. Their engineers agreed with the interpretation proposed in this thesis.

In conclusion, the analysis demonstrates that hydrogen flow through the injector is controlled by a pressure-dependent aerodynamic limitation rather than by geometric choking, and that the combustion response is strongly coupled to this injection behavior. The semi-empirical correlation of approximately 83 MJ/kg provides a physically grounded method to derive injection profiles from experimental data, extending the model's predictive capability to other operating points without the need for direct injection measurements.

6.1.3 Combustion Process

The combustion simulations clarified the physical and chemical mechanisms governing ignition and flame development in hydrogen–diesel dual-fuel operation.

The results show that hydrogen ignition does not originate from direct flame propagation from the diesel pilot into the hydrogen jet, but rather from the thermally promoted autoignition of hydrogen in the hot environment created by the pilot combustion. The diesel flame raises the local temperature around the hydrogen jet to roughly 1300 K, which is about 200 K higher than the surrounding in-cylinder gas, and accelerates the formation of radicals, mainly HO_2 and H_2O_2. These species accumulate until their decomposition triggers hydrogen ignition. The evidence clearly indicates that ignition begins within the hydrogen jet itself, and not as a consequence of direct radical diffusion from the diesel flame, although a small amount of transported OH may contribute to accelerating the final transition.

The comparison between the original case and the half-diesel case supports this interpretation. In the 100% diesel case, ignition occurs almost immediately after pilot combustion, with virtually no premixing. In contrast, reducing the pilot to 50% delays ignition, allowing limited hydrogen–air mixing before combustion starts. This short premixed phase produces a sharper aHRR spike once ignition occurs. After this initial stage, both configurations transition rapidly to a diffusion-controlled regime with a smooth, predominantly laminar flame structure. The laminar appearance is consistent with hydrogen's high diffusivity and rapid reaction kinetics, although the LFC combustion model may also accentuate this behavior.

The hydrogen-only case provided additional validation for the chemical kinetics and numerical framework. Without the diesel pilot, combustion started approximately 1.8 ms after the beginning of injection. Strictly speaking, this interval represents the delay between the start of injection and the first detectable combustion, not the true chemical ignition delay. However, given hydrogen's extremely fast mixing rate and the continuous injection process, this distinction becomes negligible. The measured delay is consistent with published data for similar conditions, in this case an ambient temperature of about 1100 K and an injected hydrogen temperature near 350 K, confirming that the reaction mechanism seems to accurately capture the temperature dependence.

During this delay, a large amount of premixed hydrogen-air mixture accumulates, which then burns almost instantaneously once ignition occurs, producing a steep pressure rise and a sharp aHRR peak. This behavior highlights the inherent instability of hydrogen autoignition under compression ignition conditions and explains why dual-fuel operation requires an auxiliary ignition source. The diesel pilot plays this stabilizing role: it raises the local temperature, shortens the ignition delay, and distributes the heat release more gradually, preventing the uncontrolled combustion observed in the hydrogen-only case.

Overall, the combustion results establish that hydrogen ignition in dual-fuel operation is governed primarily by the thermal field created by the diesel pilot, rather than by flame propagation or radical transport. The degree of premixing, and thus the initial shape of the aHRR curve, is controlled by the pilot amount and by the transient dynamics of the hydrogen injection.

6.1.4 Modeling Adjustments and Other Findings

In addition to the main findings, several secondary modeling aspects were explored to assess the robustness and sensitivity of the simulations.

Parametric variations confirmed that while turbulence and mixing parameters can influence early heat release, they do not alter the fundamental ignition mechanism. Lowering the turbulent Schmidt number from 0.9 to 0.5 improved early mixing and slightly increased the first aHRR peak, whereas adding 5% EGR reduced it. The experimental EGR levels (1.5–2%) are too small to significantly impact combustion behavior.

Regarding the combustion framework, the study showed that the Laminar Flame Concept (LFC) model in STAR-CCM + tends to burn hydrogen rapidly once it enters the chamber. This results in a heat-release curve that mirrors the injection profile almost perfectly, sometimes producing a slightly premature rise compared to the experiment. Comparison with previous work by Antonacci using CONVERGE revealed that this coupling is stronger in STAR-CCM +, suggesting that the model may overestimate the mixing at the start of injection.

6.2 Limitations

Although this work has yielded valuable insights, several limitations must be acknowledged. First, the derivation of injection profiles from aHRR, while robust and validated against previous thesis work, inherently introduces uncertainties. The heat-release analysis is based on experimental pressure traces combined with the in-cylinder volume evolution obtained from CFD, and its accuracy is limited by the resolution of the pressure signal (0.1 CAD) as well as the numerical differentiation involved. These factors may smooth out or distort rapid transients during injection and early combustion. As a result, the reconstructed mass flow profiles cannot be guaranteed to match the fidelity of direct injection measurements.

Second, the injector was modeled using simplified isentropic nozzle theories, without resolving the internal flow field of the injector itself. Effects such as boundary-layer growth, flow separation, and three-dimensional turbulence within the sac and orifices were not explicitly captured. These phenomena are likely critical to understanding why effective flow areas appear smaller than geometrical orifice areas. Previous attempts using detailed CFD injector models within Converge failed to reproduce mass flow

profiles accurately under Westport's reported conditions, limiting the availability of validated modeling approaches.

Third, the scope of the experimental dataset was restricted. Only a handful of operating conditions were available, which constrains the generalizability of the conclusions. Broader validation across different pressures, loads, and injection strategies would be required to establish universal trends. Additionally, the analysis did not include direct experimental measurements of mass flow, spray penetration, or injector needle dynamics, all of which would be valuable for model validation.

On the modeling side, STAR-CCM+'s Laminar Flamelet Combustion (LFC) model presents another limitation. Its tunability is minimal, with only a few adjustable parameters (e.g., chemical mechanisms or retardation factors). This prevented systematic testing of whether the observed discrepancies are due to the combustion model formulation, the turbulence–mixing interaction, or limitations in chemical kinetics. Similarly, higher-fidelity simulations such as Large Eddy Simulation (LES) or injector-resolved CFD were beyond the computational resources and scope of this thesis.

Furthermore, due to time constraints, it was not possible to extend the analysis to include several variations in the pilot diesel quantity or to perform detailed two- and three-dimensional visualizations of the autoignition process in the pure-diesel reference case. These studies could have provided valuable insight into ignition kernel formation and flame propagation mechanisms, and remain as interesting avenues for future investigation. Likewise, now that the conditions leading to hydrogen autoignition are better understood, exploring alternative pilot fuels or ignition strategies could yield promising results for improving controllability and reducing reliance on conventional diesel.

Finally, additional numerical limitations arise from the meshing framework in STAR-CCM+. The software does not allow fully localized remeshing, meaning that mesh refinement in the vicinity of the injector must be propagated throughout the entire domain. This reduces efficiency and limits the achievable resolution near critical regions. Moreover, since the injector is modeled as a separate part, it must interact with the cylinder boundaries in a way that cannot be perfectly eliminated. This introduces grid-induced errors, particularly in the cells surrounding the nozzle, where changes in mesh size can propagate artificial numerical effects into the flow field. These issues make it challenging to obtain a fully accurate representation of the injector–cylinder interaction without residual numerical artifacts.

Taken together, these limitations highlight that the results, while indicative and valuable, should be interpreted cautiously and seen as the basis for further exploration rather than definitive closure on the subject.

6.3 Future Work

Building on the insights and limitations identified in this thesis, several directions for future research emerge that could improve the modeling of hydrogen HPDI systems and their application in engine development.

Injector and nozzle flow modeling

A first priority is the development of high-fidelity CFD models of the injector, including the sac region and internal nozzle orifices. Such simulations would make it possible to resolve boundary-layer growth, recirculation zones, cavitation, and turbulence effects that are currently simplified in isentropic nozzle theory. Validating these models against experimental datasets provided by Cespira would clarify whether the effective flow area reductions inferred here are indeed caused by internal recirculation. Extending the analysis to a broad range of pressure ratios would also help to quantify the observed pressure dependence of injection behavior.

Combustion model assessment and alternatives

Another key avenue is the systematic evaluation of combustion modeling frameworks. The evidence presented here suggests that STAR-CCM+'s Laminar Flamelet Combustion (LFC) model may exagger-

ate the coupling between injection and heat release, particularly at the start of injection. This hypothesis should be tested by benchmarking LFC against alternative closures, such as ECFM or other turbulent flame speed formulations, in both hydrogen-diesel dual-fuel and conventional diesel cases. Parallel investigations into turbulence-mixing models and chemical kinetic mechanisms would help determine whether the fast-burning behavior originates from mixing assumptions, reaction chemistry, or the LFC formulation itself. Improving combustion fidelity is essential if CFD is to be reliably used for the design of hydrogen HPDI concepts.

Experimental validation and dataset expansion

Further experimental work could be beneficial to reduce uncertainty and validate modeling approaches. In particular, direct measurements of injection rate profiles, needle lift dynamics, spray penetration, and in-cylinder pressure under varied load and pressure conditions would provide a comprehensive dataset for calibration. Coordinated research with injector manufacturers could bridge the gap between industrial know-how and academic modeling, ensuring that reconstructed curves and CFD predictions are grounded in reality.

Alternative fuels and ignition strategies

As the understanding of hydrogen autoignition improves, future studies could explore alternative pilot fuels or even non-diesel ignition systems. Fuels with different volatility, cetane number, or chemical composition could provide enhanced controllability and reduced carbon intensity, particularly if used in combination with optimized injection strategies. This would broaden the scope of hydrogen HPDI research toward more sustainable and flexible engine concepts.

Emissions modelling

Future studies should extend the scope beyond pressure and heat release traces to include detailed emissions modeling. This would involve analyzing pollutant formation mechanisms, such as NOx, particulate matter, and unburned hydrocarbons, under dual-fuel operating conditions. The use of complex chemistry models will be particularly important for capturing the formation of slow-forming pollutants. Moreover, experimental validation of emissions data will be essential to verify and refine the CFD models. Emissions modeling is critical for assessing environmental impacts and guiding the development of cleaner hydrogen HPDI engine technologies. Such studies are highly relevant for the future advancement of this technology and the design of its exhaust systems.

Closing remarks

In summary, this thesis provides evidence of both the challenges and the potential of modeling hydrogen direct injection in dual-fuel engines. While current tools can already reproduce experimental trends under certain conditions, significant gaps remain in the accurate representation of injector flow dynamics and combustion processes. Addressing these gaps through targeted CFD development, systematic combustion benchmarking, and expanded experimental validation will be crucial for enabling predictive simulations and guiding the design of next-generation hydrogen-fueled heavy-duty engines.

Bibliography

[1] Scania AB. Electric trucks have a range of up to 400 km | scania group, . URL https://www.scania.com/group/en/home/electrification/e-mobility-hub/electric-trucks-have-a-range-of-up-to-400-km.html.

[2] Scania AB. Electric trucks - a complete solution | scania group, . URL https://www.scania.com/group/en/home/products-and-services/trucks/battery-electric-truck.html.

[3] Scania AB. Scania publishes life cycle assessment of battery electric vehicles, . URL https://www.scania.com/group/en/home/newsroom/press-releases/press-release-detail-page.html.

[4] Volvo AB. Polestar 2 LCA report, . URL https://www.polestar.com/global/news/polestar-2-lca-report/.

[5] BMW AG. Environmental-report_bmw-i4m50, . URL https://www.bmwgroup.com/en/search.html.

[6] BMW AG. Hydrogen in BMW, . URL https://www.bmwgroup-classic.com/en/history/hydrogen.html.

[7] Volkswagen AG. Green power for all ID. models on european roads: Volkswagen supports 26 solar and wind farms, . URL https://www.volkswagen-newsroom.com/en/press-releases.

[8] A. Ajanovic, M. Sayer, and R. Haas. The economics and the environmental benignity of different colors of hydrogen. 47(57):24136–24154, 2022. ISSN 03603199. doi: 10.1016/j.ijhydene.2022.02.094. URL https://doi.org/10.1016/j.ijhydene.2022.02.094.

[9] H. Aljabri, R. Menaca, N. Panthi, K. Moreno-Cabezas, F. Almatrafi, X. Liu, M. Silva, E. Cenker, A. Al-Ramadan, B. Mohan, M. Al-lehaibi, A. Amer, G. Magnotti, and H. G. Im. Assessment of combustion models in hydrogen engine simulations using optical measurements. 392:134871, 2025. ISSN 0016-2361. doi: 10.1016/j.fuel.2025.134871. URL https://doi.org/10.1016/j.fuel.2025.134871.

[10] S. C. Anenberg, J. Miller, R. Minjares, L. Du, D. K. Henze, F. Lacey, C. S. Malley, L. Emberson, V. Franco, Z. Klimont, and C. Heyes. Impacts and mitigation of excess diesel-related NOx emissions in 11 major vehicle markets. 545(7655):467–471, 2017. ISSN 1476-4687. doi: 10.1038/nature22086. URL https://doi.org/10.1038/nature22086. Publisher: Nature Publishing Group.

[11] G. Angileri. La formazione della carica in motori a combustione interna a iniezione diretta di idrogeno: confronto numerico-sperimentale, 2023. URL https://morethesis.unimore.it/theses/available/etd-11102023-103737/.

[12] D. Antonacci. Computational investigation of gas injection and combustion in hydrogen HPDI engines including in-nozzle flow, 2024. URL https://morethesis.unimore.it/theses/available/etd-03252024-181837/.

[13] R. Babayev, A. Andersson, A. S. Dalmau, H. G. Im, and B. Johansson. Computational characterization of hydrogen direct injection and nonpremixed combustion in a compression-ignition

engine. 46(35):18678–18696, 2021. ISSN 0360-3199. doi: 10.1016/j.ijhydene.2021.02.223. URL https://doi.org/10.1016/j.ijhydene.2021.02.223.

[14] B. Brunekreef and S. T. Holgate. Air pollution and health. 360(9341):1233–1242, 2002. ISSN 0140-6736, 1474-547X. doi: 10.1016/S0140-6736(02)11274-8. URL https://doi.org/10.1016/S0140-6736(02)11274-8. Publisher: Elsevier.

[15] K. Bruninx, D. Madzharov, E. Delarue, and W. D'haeseleer. Impact of the german nuclear phase-out on europe's electricity generation—a comprehensive study. 60:251–261, 2013. ISSN 0301-4215. doi: 10.1016/j.enpol.2013.05.026. URL https://doi.org/10.1016/j.enpol.2013.05.026.

[16] F. Brójo. A review on supersonic nozzle design and analysis with traditional methods, 2025. URL https://www.preprints.org/manuscript/202503.1464/v1.

[17] M. P. Burke, M. Chaos, Y. Ju, F. L. Dryer, and S. J. Klippenstein. Comprehensive h2/o2 kinetic model for high-pressure combustion. 44(7):444–474, 2012. ISSN 1097-4601. doi: 10.1002/kin.20603. URL https://doi.org/10.1002/kin.20603. _eprint: https://onlinelibrary.wiley.com/doi/pdf/10.1002/kin.20603.

[18] M. C. Cameretti, R. De Robbio, E. Mancaruso, and M. Palomba. CFD study of dual fuel combustion in a research diesel engine fueled by hydrogen, 2022. URL https://doi.org/10.3390/en15155521.

[19] Cespira. Application of westport fuel systems' HPDITM technology to a demonstration truck, 2023.

[20] Cespira. Cespira HPDI, 2025. URL https://wfsinc.com/technology/hpdi.

[21] Toyota Motor Corporation. Toyota showcases experimental hydrogen-powered GR yaris. URL https://www.toyota.ie/company/news/2021/gr-yaris-showcase.

[22] H. J. Curran. Developing detailed chemical kinetic mechanisms for fuel combustion. 37(1):57–81, 2019. ISSN 1540-7489. doi: 10.1016/j.proci.2018.06.054. URL https://doi.org/10.1016/j.proci.2018.06.054.

[23] H. Fatehi. HyZERO - HYdrogen internal combustion engine with ZERO carbon emission in heavy duty fleet, 2022. URL https://portal.research.lu.se/en/projects/hyzero-hydrogen-internal-combustion-engine-with-zero-carbon-emiss.

[24] S. Fontanesi, G. Cicalese, and Severi E. 2013-01-1107: Analysis of turbulence model effect on the characterization of the in-cylinder flow field in a HSDI diesel engine - technical paper, 2013. URL https://doi.org/10.4271/2013-01-1107.

[25] R. Fuller, P. J. Landrigan, K. Balakrishnan, G. Bathan, S. Bose-O'Reilly, M. Brauer, J. Caravanos, T. Chiles, A. Cohen, L. Corra, M. Cropper, G. Ferraro, J. Hanna, D. Hanrahan, H. Hu, D. Hunter, G. Janata, R. Kupka, B. Lanphear, M. Lichtveld, K. Martin, A. Mustapha, E. Sanchez-Triana, K. Sandilya, L. Schaefli, J. Shaw, J. Seddon, W. Suk, M. M. Téllez-Rojo, and C. Yan. Pollution and health: a progress update. 6(6):e535–e547, 2022. ISSN 2542-5196. doi: 10.1016/S2542-5196(22)00090-0. URL https://doi.org/10.1016/S2542-5196(22)00090-0. Publisher: Elsevier.

[26] National Grid Group. The hydrogen colour spectrum. URL https://www.nationalgrid.com/stories/energy-explained/hydrogen-colour-spectrum.

[27] J. Gustavsson and V. I. Golovitchev. Spray combustion simulation based on detailed chemistry approach for diesel fuel surrogate model, 2003. URL https://doi.org/10.4271/2003-01-1848. ISSN: 0148-7191, 2688-3627.

[28] Ö. L. Gülder. Correlations of laminar combustion data for alternative s.i. engine fuels, 1984. URL https://doi.org/10.4271/841000. ISSN: 0148-7191, 2688-3627.

[29] M. S. Habibullah, B. H. Din, S. Tan, and H. Zahid. Impact of climate change on biodiversity loss: global evidence. 29(1):1073–1086, 2022. ISSN 1614-7499. doi: 10.1007/s11356-021-15702-8. URL https://doi.org/10.1007/s11356-021-15702-8.

[30] S. Hickel. 05_rans - AE4202 CFD for aerospace engineers (2023/24 q1), 2023. URL https://brightspace.tudelft.nl/d2l/le/content/593417/viewContent/3225845/View.

[31] M. Hilpert, B. A. Mora, J. Ni, A. M. Rule, and K. E. Nachman. Hydrocarbon release during fuel storage and transfer at gas stations: Environmental and health effects. 2(4):412–422, 2015. ISSN 2196-5412. doi: 10.1007/s40572-015-0074-8. URL https://doi.org/10.1007/s40572-015-0074-8.

[32] T. Holler, E. Komen, and I. Kljenak. The role of CFD combustion modeling in hydrogen safety management – VII: Validation for hydrogen deflagration in large-scale hydrogen-air-steam experiment. 342:133–146, 2019. ISSN 0029-5493. doi: 10.1016/j.nucengdes.2018.11.033. URL https://doi.org/10.1016/j.nucengdes.2018.11.033.

[33] N. Iafrate, M. Matrat, and J. Zaccardi. Numerical investigations on hydrogen-enhanced combustion in ultra-lean gasoline spark-ignition engines. 22(2):375–389, 2021. ISSN 1468-0874. doi: 10.1177/1468087419870688. URL https://doi.org/10.1177/1468087419870688. Publisher: SAGE Publications.

[34] Institute for Energy Rresearch. Environmental impacts of lithium-ion batteries, 2023. URL https://www.instituteforenergyresearch.org/renewable/environmental-impacts-of-lithium-ion-batteries/.

[35] W. P Jones and B. E Launder. The prediction of laminarization with a two-equation model of turbulence. 15(2):301–314, 1972. ISSN 0017-9310. doi: 10.1016/0017-9310(72)90076-2. URL https://doi.org/10.1016/0017-9310(72)90076-2.

[36] M. Karimi, X. Wang, J. Hamilton, and M. Negnevitsky. Numerical investigation on hydrogen-diesel dual-fuel engine improvements by oxygen enrichment. 47(60):25418–25432, 2022. ISSN 0360-3199. doi: 10.1016/j.ijhydene.2022.05.271. URL https://doi.org/10.1016/j.ijhydene.2022.05.271.

[37] L. E. Klebanoff, J. W. Pratt, and C. B. LaFleur. Comparison of the safety-related physical and combustion properties of liquid hydrogen and liquid natural gas in the context of the SF-BREEZE high-speed fuel-cell ferry. 42(1):757–774, 2017. ISSN 0360-3199. doi: 10.1016/j.ijhydene.2016.11.024. URL https://doi.org/10.1016/j.ijhydene.2016.11.024.

[38] A. Kéromnès, W. K. Metcalfe, K. A. Heufer, N. Donohoe, A. K. Das, C. Sung, J. Herzler, C. Naumann, P. Griebel, O. Mathieu, M. C. Krejci, E. L. Petersen, W. J. Pitz, and H. J. Curran. An experimental and detailed chemical kinetic modeling study of hydrogen and syngas mixture oxidation at elevated pressures. 160(6):995–1011, 2013. ISSN 0010-2180. doi: 10.1016/j.combustflame.2013.01.001. URL https://doi.org/10.1016/j.combustflame.2013.01.001.

[39] T. T. Le, P. Sharma, B. J. Bora, V. D. Tran, T. H. Truong, H. C. Le, and P. Q. P. Nguyen. Fueling the future: A comprehensive review of hydrogen energy systems and their challenges. 54:791–816, 2024. ISSN 0360-3199. doi: 10.1016/j.ijhydene.2023.08.044. URL https://doi.org/10.1016/j.ijhydene.2023.08.044.

[40] G. K. Lilik, H. Zhang, J. M. Herreros, D. C. Haworth, and A. L. Boehman. Hydrogen assisted diesel combustion. 35(9):4382–4398, 2010. ISSN 0360-3199. doi: 10.1016/j.ijhydene.2010.01.105. URL https://doi.org/10.1016/j.ijhydene.2010.01.105.

[41] H. Liu. 3d CFD simulations of hydrogen engine combustion. 2023. ISSN 0282-1990. URL http://lup.lub.lu.se/student-papers/record/9125419.

[42] L. S. Martins, L. F. Guimarães, A. B. Botelho Junior, J. A. S. Tenório, and D. C. R. Espinosa. Electric car battery: An overview on global demand, recycling and future approaches towards sustainability. 295:113091, 2021. ISSN 0301-4797. doi: 10.1016/j.jenvman.2021.113091. URL https://doi.org/10.1016/j.jenvman.2021.113091.

[43] P. J. Megía, A. J. Vizcaíno, J. A. Calles, and A. Carrero. Hydrogen production technologies: From fossil fuels toward renewable sources. a mini review. 35(20):16403–16415, 2021. ISSN 0887-0624. doi: 10.1021/acs.energyfuels.1c02501. URL https://doi.org/10.1021/acs.energyfuels.1c02501. Publisher: American Chemical Society.

[44] M. Metghalchi and J. C. Keck. Burning velocities of mixtures of air with methanol, isooctane, and indolene at high pressure and temperature. 48:191–210, 1982. ISSN 0010-2180. doi: 10.1016/0010-2180(82)90127-4. URL https://doi.org/10.1016/0010-2180(82)90127-4.

[45] D. Mumford, S. Ptucha, S. Baker, S. Munshi, E. Olofsson, and A. Palmkvist. High performance hydrogen engine applications, 2023. URL https://wfsinc.com/file_library/files/wfs-wfsinc/23-04-westport-h2-hpdi-vienna-motor-symposium.pdf#:~:text=Westport%E2%80%99s%20HPDI%20fuel%20system%20can%20be%20used%20with,with%20multiple%20development%20projects%20recently%20announced%20and%20underway.

[46] S. Muppala and S. Vasudevan. RANS studies of hydrogen-enrichment premixed turbulent flames. 1080(1):012046, 2021. ISSN 1757-899X. doi: 10.1088/1757-899X/1080/1/012046. URL https://dx.doi.org/10.1088/1757-899X/1080/1/012046. Publisher: IOP Publishing.

[47] M. Muralidharan. (PDF) a technical review on performance and emissions of compressed natural gas – diesel dual fuel engine. In *ResearchGate*, 2019. URL https://www.researchgate.net/publication/336061938_A_Technical_Review_on_Performance_and_Emissions_of_Compressed_Natural_Gas_-_Diesel_Dual_Fuel_Engine.

[48] J. D. Naber and D. L. Siebers. Hydrogen combustion under diesel engine conditions. 23(5):363–371, 1998. ISSN 0360-3199. doi: 10.1016/S0360-3199(97)00083-9. URL https://doi.org/10.1016/S0360-3199(97)00083-9.

[49] NASA. Effects of climate change - NASA science, 2022. URL https://science.nasa.gov/climate-change/effects/. Section: Climate Change.

[50] N Nordin. Numerical simulations of non-steady spray combustion using a detailed chemistry approach. 1998.

[51] C. Olm, I. Zsély, R. Pálvölgyi, T. Varga, T. Nagy, H. J. Curran, and T. Turányi. Comparison of the performance of several recent hydrogen combustion mechanisms. 161(9):2219–2234, 2014. ISSN 0010-2180. doi: 10.1016/j.combustflame.2014.03.006. URL https://doi.org/10.1016/j.combustflame.2014.03.006.

[52] PAHO and WHO. Climate change and health - PAHO/WHO | pan american health organization, 2025. URL https://www.paho.org/en/topics/climate-change-and-health.

[53] European Parliament. Regulation - 2024/1257 - EN - EUR-lex. URL https://eur-lex.europa.eu/eli/reg/2024/1257/oj/eng. Doc ID: 32024R1257 Doc Title: Regulation (EU) 2024/1257 of the European Parliament and of the Council of 24 April 2024 on type-approval of motor vehicles and engines and of systems, components and separate technical units intended for such vehicles, with respect to their emissions and battery durability (Euro 7), amending Regulation (EU) 2018/858 of the European Parliament and of the Council and repealing Regulations (EC) No 715/2007 and (EC) No 595/2009 of the European Parliament and of the Council, Commission Regulation (EU) No 582/2011, Commission Regulation (EU) 2017/1151, Commission Regulation (EU) 2017/2400 and Commission Implementing Regulation (EU) 2022/1362 (Text with EEA relevance).

[54] European Parliament. Euro 7: Deal on new EU rules to reduce road transport emissions | news, 2023. URL https://www.europarl.europa.eu/news/en/press-room/20231207IPR15740/euro-7-deal-on-new-eu-rules-to-reduce-road-transport-emissions.

[55] A. Patel, S. Kong, and R. D. Reitz. Development and validation of a reduced reaction mechanism for HCCI engine simulations, 2004. URL https://doi.org/10.4271/2004-01-0558. ISSN: 0148-7191, 2688-3627.

[56] T. R. Patel. Turbulence characterization of high tumble in cylinder flow using 3d CFD simulations, 2023. URL https://etd.ohiolink.edu/acprod/odb_etd/etd/r/1501/10?clear=10&p10_accession_num=osu1682011166323006.

[57] N. Peters. The turbulent burning velocity for large-scale and small-scale turbulence. 384:107–132, 1999. ISSN 1469-7645, 0022-1120. doi: 10.1017/S0022112098004212. URL https://doi.org/10.1017/S0022112098004212.

[58] T. Poinsot and D. Veynante. (PDF) theoretical and numerical combustion, 2005. URL https://www.researchgate.net/publication/248068931_Theoretical_and_Numerical_Combustion.

[59] S. B. Pope. Turbulent flows. 12(11):2020, 2001. ISSN 0957-0233. doi: 10.1088/0957-0233/12/11/705. URL https://dx.doi.org/10.1088/0957-0233/12/11/705.

[60] S. Posch, C. Gößnitzer, M. Lang, R. Novella, H. Steiner, and A. Wimmer. Turbulent combustion modeling for internal combustion engine CFD: A review. 106:101200, 2025. ISSN 0360-1285. doi: 10.1016/j.pecs.2024.101200. URL https://doi.org/10.1016/j.pecs.2024.101200.

[61] Aglave R. (PDF) simcenter STAR-CCM+ reacting flows spotlight, 2019. URL https://doi.org/10.13140/RG.2.2.20194.68808.

[62] Y. Ra and R. D. Reitz. A reduced chemical kinetic model for IC engine combustion simulations with primary reference fuels. 155(4):713–738, 2008. ISSN 0010-2180. doi: 10.1016/j.combustflame.2008.05.002. URL https://doi.org/10.1016/j.combustflame.2008.05.002.

[63] CP Ranasinghe and W Malalasekera. Modelling combustion in spark ignition engines with special emphasis on near wall flame quenching. 23(1):20–32, 2022. ISSN 1468-0874. doi: 10.1177/1468087420972903. URL https://doi.org/10.1177/1468087420972903. Publisher: SAGE Publications.

[64] E. Ranzi, A. Frassoldati, A. Stagni, M. Pelucchi, A. Cuoci, and T. Faravelli. Reduced kinetic schemes of complex reaction systems: Fossil and biomass-derived transportation fuels. 46(9):512–542, 2014. ISSN 1097-4601. doi: 10.1002/kin.20867. URL https://doi.org/10.1002/kin.20867. _eprint: https://onlinelibrary.wiley.com/doi/pdf/10.1002/kin.20867.

[65] Frassoldati A. Stagni A. Pelucchi M. Cuoci A. Faravelli T. Ranzi, E. Detailed kinetic mechanisms - creckmodeling, 2023. URL https://www.creckmodeling.polimi.it/menu-kinetics/menu-kinetics-detailed-mechanisms/.

[66] J. A. Raub, M. Mathieu-Nolf, N. B. Hampson, and S. R. Thom. Carbon monoxide poisoning — a public health perspective. 145(1):1–14, 2000. ISSN 0300-483X. doi: 10.1016/S0300-483X(99)00217-6. URL https://doi.org/10.1016/S0300-483X(99)00217-6.

[67] World Population Review. Cobalt reserves by country 2025, . URL https://worldpopulationreview.com/country-rankings/cobalt-reserves-by-country.

[68] World Population Review. Cost of electricity by country 2025, . URL https://worldpopulationreview.com/country-rankings/cost-of-electricity-by-country.

[69] H. Ritchie. Many countries have decoupled economic growth from CO2 emissions, even if we take offshored production into account. 2021. URL https://ourworldindata.org/co2-gdp-decoupling.

[70] H. Ritchie. A number of countries have decoupled economic growth from energy use, even if we take offshored production into account. 2021. URL https://ourworldindata.org/energy-gdp-decoupling.

[71] H. Ritchie and P. Rosado. Energy mix. 2020. URL https://ourworldindata.org/energy-mix.

[72] H. Ritchie, P. Rosado, and M. Roser. Breakdown of carbon dioxide, methane and nitrous oxide emissions by sector. 2020. URL https://ourworldindata.org/emissions-by-sector.

[73] H. Ritchie, P. Rosado, and M. Roser. Greenhouse gas emissions. 2020. URL https://ourworldindata.org/greenhouse-gas-emissions.

[74] H. Ritchie, P. Rosado, and M. Roser. CO□ and greenhouse gas emissions. 2023. URL https://ourworldindata.org/co2-and-greenhouse-gas-emissions.

[75] Ritchie, H. Tracking global data on electric vehicles. 2024. URL https://ourworldindata.org/electric-car-sales.

[76] A. Ruiz, J. Meseguer, and A. Sanz. *Aerodinámica Básica*. Garceta, 2022.

[77] F. J. Salvador, S. Ruiz, J. Gimeno, and J. De la Morena. Estimation of a suitable schmidt number range in diesel sprays at high injection pressure. 50(9):1790–1798, 2011. ISSN 1290-0729. doi: 10.1016/j.ijthermalsci.2011.03.030. URL https://doi.org/10.1016/j.ijthermalsci.2011.03.030.

[78] P. Sathyaprakasan and G. Kannan. Economics of bio-hydrogen production. 6(4):352–356, 2015. ISSN 20100264. doi: 10.7763/IJESD.2015.V6.617. URL https://doi.org/10.7763/IJESD.2015.V6.617.

[79] P. Saxena and F. A. Williams. Testing a small detailed chemical-kinetic mechanism for the combustion of hydrogen and carbon monoxide. 145(1):316–323, 2006. ISSN 0010-2180. doi: 10.1016/j.combustflame.2005.10.004. URL https://doi.org/10.1016/j.combustflame.2005.10.004.

[80] R. W. Schefer and L. Ca. Flammability limits of hydrogen/air mixtures. URL https://www.osti.gov/servlets/purl/1721461#:~:text=Although%20the%20generally%20accepted%20value,downward%20and%20spherically%20propagating%20flames.

[81] F. Scrignoli, F. Vecchio, F. Legrottaglie, E. Mattarelli, and C. A. Rinaldini. Numerical investigation of dual fuel combustion on a compression ignition engine fueled with hydrogen/natural gas blends. 3(1):132–151, 2022. ISSN 2673-3994. doi: 10.3390/fuels3010009. URL https://doi.org/10.3390/fuels3010009. Number: 1 Publisher: Multidisciplinary Digital Publishing Institute.

[82] N. Shammas, L. K. Wang, and M. Sung Wang. Sources, chemistry and control of acid rain in the environment, 2020. URL https://doi.org/10.1142/9789811207136_0001.

[83] T. Shih, W. Liou, A. Shabbir, Z. Yang, and J. Zhu. A new k-□ eddy viscosity model for high reynolds number turbulent flows - ScienceDirect, 1995. URL https://doi.org/10.1016/0045-7930(94)00032-T.

[84] Siemens. Complex chemistry, . URL https://stevedocs.azurewebsites.net/GUID-5631802A-AA81-4A68-B273-D599CA5A05FD.html.

[85] Siemens. Eddy break-up, . URL https://stevedocs.azurewebsites.net/GUID-D427B894-CFEE-4C43-A850-498FF878F086.html.

[86] Siemens. Gas phase combustion—flamelet models, . URL https://stevedocs.azurewebsites.net/GUID-83013756-BBBE-4F7F-81B5-1C34D3023212.html.

[87] Siemens. Reactions—species transport, . URL https://stevedocs.azurewebsites.net/GUID-85B188AC-828D-4E83-9B23-8296FB3D44DA.html.

[88] Siemens. Turbulent flame speed closure, . URL https://stevedocs.azurewebsites.net/GUID-2D2B1FB8-42BA-4DE8-8758-D5459FC121AE.html.

[89] D. I. Stern. The role of energy in economic growth. 2011.

[90] M. Tidswell and S. Muppala. A numerical study of turbulent flame speed models for h2/CH4/air premixed combustion. 3(6), 2014.

[91] Y. Tominaga and T. Stathopoulos. Turbulent schmidt numbers for cfd analysis with various types of flowfield. atmospheric environment, 41(37), 8091–8099. 41(37):8091–8099, 2007. ISSN 1352-2310. doi: 10.1016/j.atmosenv.2007.06.054. URL https://doi.org/10.1016/j.atmosenv.2007.06.054.

[92] M. Treacy. Numerical studies of advanced combustion concepts in hydrogen and methanol compression ignition engines | lund university, 2024. URL https://www.lunduniversity.lu.se/lup/publication/62d5fdb9-ecca-4c11-8c0d-451637bb8086.

[93] M. Treacy, A. Hadadpour, X. Bai, and H. Fatehi. Performance and emissions of a novel high-pressure direct injection hydrogen dual-fuel engine. 376:132639, 2024. ISSN 0016-2361. doi: 10.1016/j.fuel.2024.132639. URL https://doi.org/10.1016/j.fuel.2024.132639.

[94] S. R. Turns. *An Introduction to Combustion*. Third edition, 1996.

[95] OAR US EPA. Regulations for greenhouse gas emissions from passenger cars and trucks, 2016. URL https://www.epa.gov/regulations-emissions-vehicles-and-engines/regulations-greenhouse-gas-emissions-passenger-cars-and.

[96] H. von Helldorff and G. J. Micklow. Chemical kinetic modeling of hydrogen-diesel co-combustion in compression ignition engines. 15(3):235–254, 2022. ISSN 1946-3952. URL https://www.jstor.org/stable/27210524. Publisher: SAE International.

[97] Weltgesundheitsorganisation and World Health Organization. *WHO global air quality guidelines: particulate matter (PM2.5 and PM10), ozone, nitrogen dioxide, sulfur dioxide and carbon monoxide*. World Health Organization, 2021. ISBN 978-92-4-003422-8. Google-Books-ID: s5pREAAAQBAJ.

[98] World Health Organisation (WHO). Air quality, energy and health - types of pollutants. URL https://www.who.int/teams/environment-climate-change-and-health/air-quality-and-health/health-impacts/types-of-pollutants.

[99] D. C. Wilcox. Reassessment of the scale-determining equation for advanced turbulence models | AIAA journal, 1988. URL https://doi.org/10.2514/3.10041.

[100] NS Energy Staff Writer. Profiling the six largest cobalt reserves in the world by country, 2021. URL https://www.nsenergybusiness.com/analysis/largest-cobalt-reserves-country/.

[101] K. Wróbel, J. Wróbel, W. Tokarz, J. Lach, K. Podsadni, and A. Czerwiński. Hydrogen internal combustion engine vehicles: A review. 15(23):8937, 2022. ISSN 1996-1073. doi: 10.3390/en15238937. URL https://doi.org/10.3390/en15238937. Number: 23 Publisher: Multidisciplinary Digital Publishing Institute.

[102] L. Xu, H. Dong, S. Liu, L. Shen, and Y. Bi. Study on the combustion mechanism of diesel/hydrogen dual fuel and the influence of pilot injection and main injection. 11(7):2122, 2023. ISSN 2227-9717. doi: 10.3390/pr11072122. URL https://doi.org/10.3390/pr11072122. Number: 7 Publisher: Multidisciplinary Digital Publishing Institute.

[103] V. Yakhot, S. A. Orszag, S. Thangam, T. B. Gatski, and C. G. Speziale. Development of turbulence models for shear flows by a double expansion technique | physics of fluids | AIP publishing, 1992. URL https://doi.org/10.1063/1.858424.

[104] V. Yakhot, S. A. Orszag, S. Thangam, T. B. Gatski, and C. G. Speziale. Development of turbulence models for shear flows by a double expansion technique. 4(7):1510–1520, 1992. ISSN 0899-8213. doi: 10.1063/1.858424. URL https://doi.org/10.1063/1.858424.

[105] T. Yao, Y. Pei, B. Zhong, S. Som, T. Lu, and K. Luo. A compact skeletal mechanism for *n*-dodecane with optimized semi-global low-temperature chemistry for diesel engine simulations. 191:339–349, 2017. ISSN 0016-2361. doi: 10.1016/j.fuel.2016.11.083. URL https://doi.org/10.1016/j.fuel.2016.11.083.

[106] H. L. Yip, A. Srna, A. C. Y. Yuen, S. Kook, R. A. Taylor, G. H. Yeoh, P. R. Medwell, and Q. N. Chan. A review of hydrogen direct injection for internal combustion engines: Towards carbon-free combustion. 9(22):4842, 2019. ISSN 2076-3417. doi: 10.3390/app9224842. URL https://doi.org/10.3390/app9224842. Number: 22 Publisher: Multidisciplinary Digital Publishing Institute.

[107] H. Zhao, J. Wang, X. Cai, H. Dai, X. Liu, G. Li, and Z. Huang. On accelerative propagation of premixed hydrogen/air laminar and turbulent expanding flames. 283:129106, 2023. ISSN 0360-5442. doi: 10.1016/j.energy.2023.129106. URL https://doi.org/10.1016/j.energy.2023.129106.

[108] H. Zhao, C. Yuan, G. Li, and F. Tian. The propagation characteristics of turbulent expanding flames of methane/hydrogen blending gas. 17(23):5997, 2024. ISSN 1996-1073. doi: 10.3390/en17235997. URL https://doi.org/10.3390/en17235997. Number: 23 Publisher: Multidisciplinary Digital Publishing Institute.

[109] V. L. Zimont. Theory of turbulent combustion of a homogeneous fuel mixture at high reynolds numbers. *Combustion, Explosion and Shock Waves*, 15:305–311, 1979.

[110] V.L. Zimont. THEORY OF TURBULENT COMBUSTION OF a HOMOGENEOUS FUEL MIXTURE AT HIGH REYNOLDS NUMBERS. 1979.

[111] V.L. Zimont and A.N. Lipatnikov. (PDF) a numerical model of premixed turbulent combustion of gases, 1995. URL https://www.researchgate.net/publication/312978033_A_numerical_model_of_premixed_turbulent_combustion_of_gases?enrichId=rgreq-0ee238b7b5caf1f567408a8dfde18797-XXX&enrichSource=Y292ZXJQYWdlOzMxMjk3ODAzMztBUzo1MjM2NjA4ODQ5NTUxMzZAMTUwMTg2MTg5Mjc3MQ%3D%3D&el=1_x_2&_esc=publicationCoverPdf.

[112] A. Züttel. Hydrogen storage methods. 91(4):157–172, 2004. ISSN 0028-1042. doi: 10.1007/s00114-004-0516-x. URL https://doi.org/10.1007/s00114-004-0516-x.

[113] M. Ó Conaire, H. J. Curran, J. M. Simmie, W. J. Pitz, and C. K. Westbrook. A comprehensive modeling study of hydrogen oxidation. 36(11):603–622. ISSN 1097-4601. doi: 10.1002/kin.20036. URL https://doi.org/10.1002/kin.20036. _eprint: https://onlinelibrary.wiley.com/doi/pdf/10.1002/kin.20036.

Appendix A

Hydrogen Combustion Figures

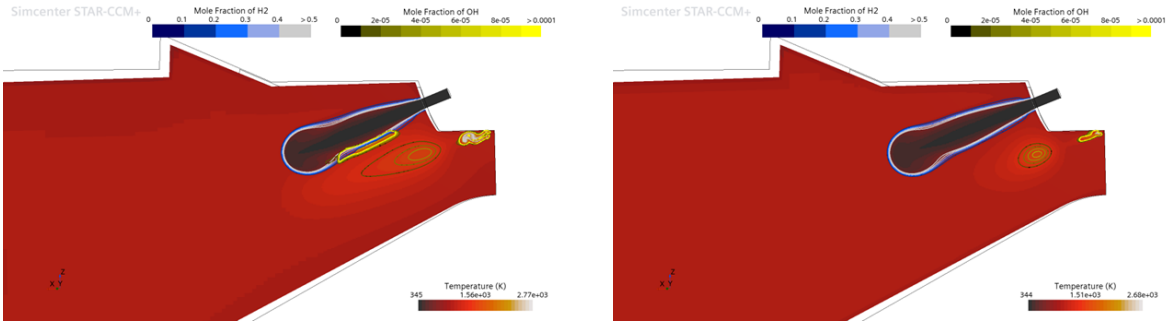

(a) Original Case 1 (A75). **(b)** Half diesel case.

Figure A.1: Temperature and isosurfaces of H2 and OH mole fractions at 718.3 CAD.

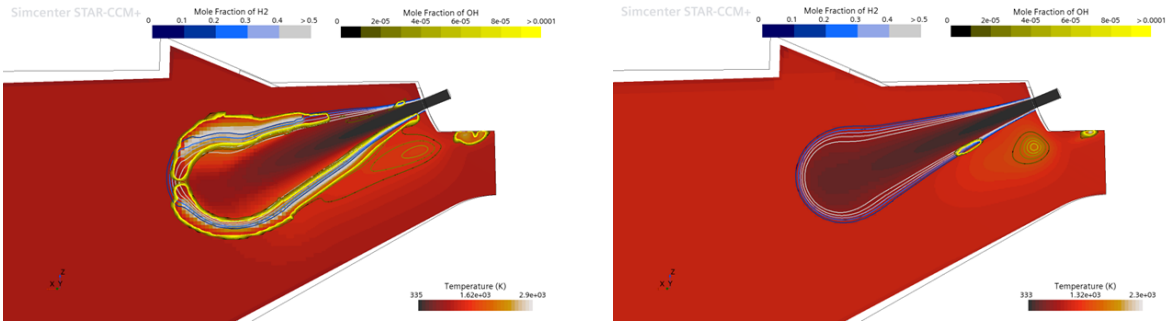

(a) Original Case 1 (A75). **(b)** Half diesel case.

Figure A.2: Temperature and isosurfaces of H2 and OH mole fractions at 719.6 CAD.

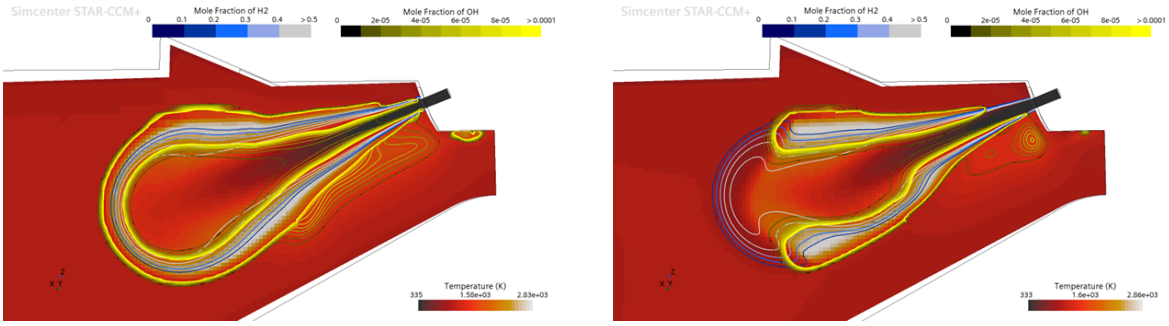

(a) Original Case 1 (A75). **(b)** Half diesel case.

Figure A.3: Temperature and isosurfaces of H2 and OH mole fractions at 720.6 CAD.

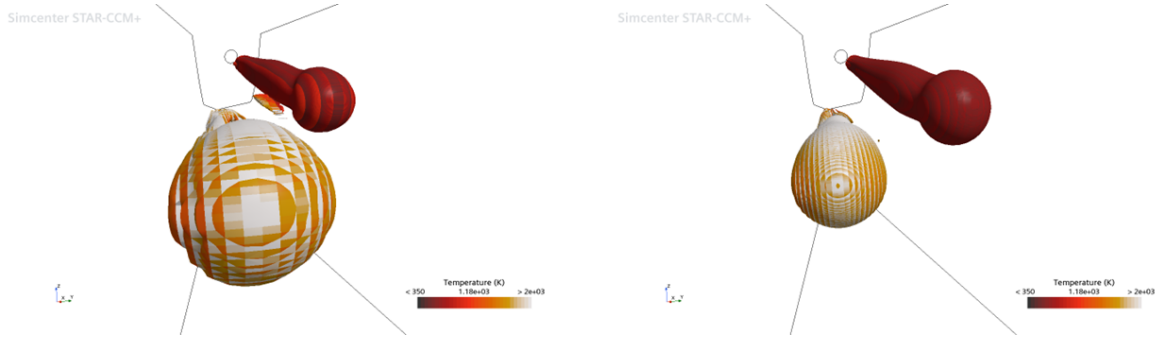

(a) Original Case 1 (A75). **(b)** Half diesel case.

Figure A.4: Three-dimensional visualization of isosurfaces of 0.1 H2 and 4×10^{-4} OH, colored by temperature, at 718.3 CAD.

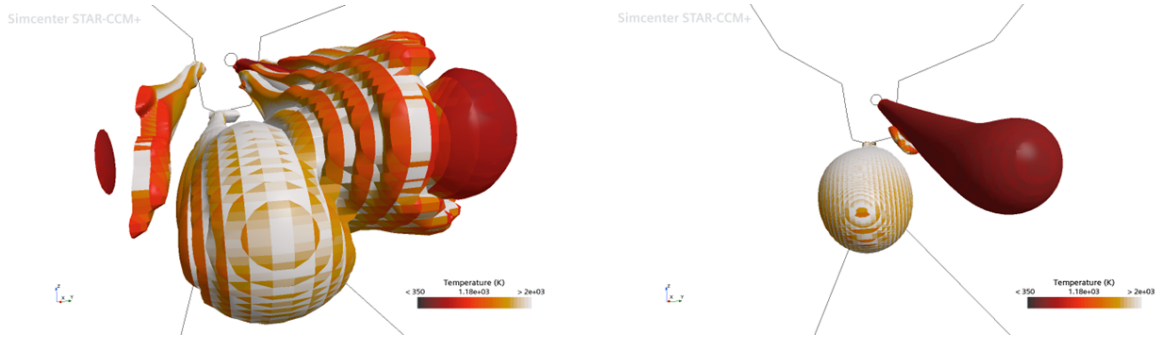

(a) Original Case 1 (A75). **(b)** Half diesel case.

Figure A.5: Three-dimensional visualization of isosurfaces of 0.1 H2 and 4×10^{-4} OH, colored by temperature, at 719.6 CAD.

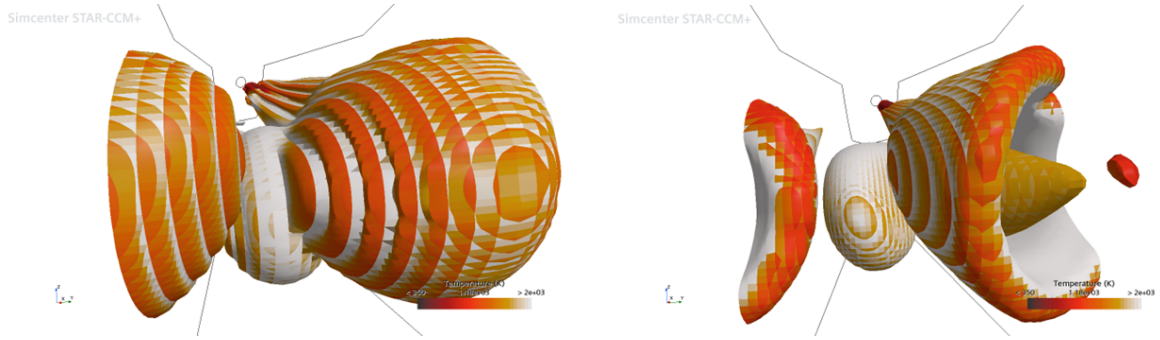

(a) Original Case 1 (A75). **(b)** Half diesel case.

Figure A.6: Three-dimensional visualization of isosurfaces of 0.1 H2 and 4×10^{-4} OH, colored by temperature, at 720.6 CAD.

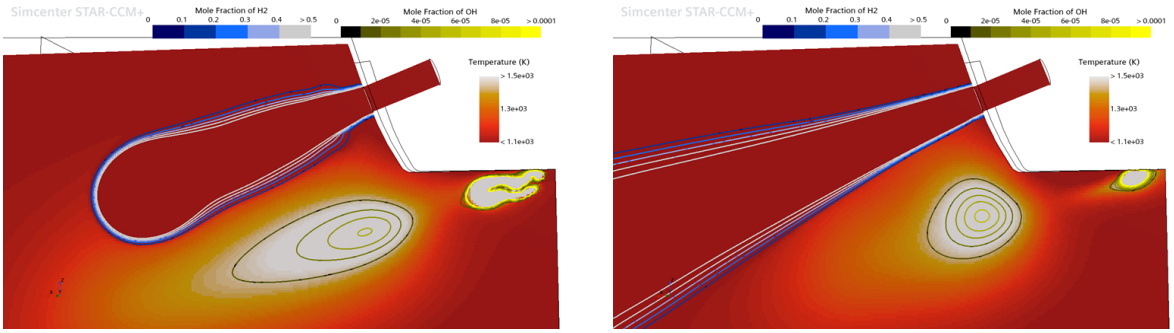

(a) Original Case 1 (A75). **(b)** Half diesel case.

Figure A.7: Contours of H2 and OH concentrations over a 2D Temperature plot - 0.2 CAD before ignition.

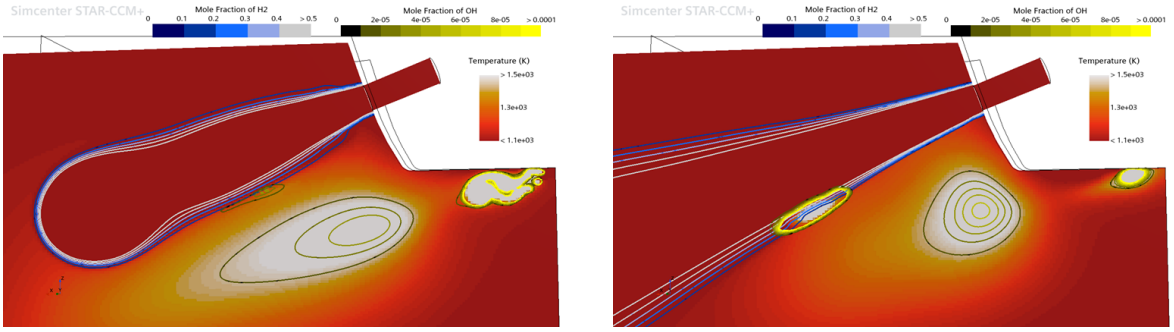

(a) Original Case 1 (A75). **(b)** Half diesel case.

Figure A.8: Contours of H2 and OH concentrations over a 2D Temperature plot - start of ignition.

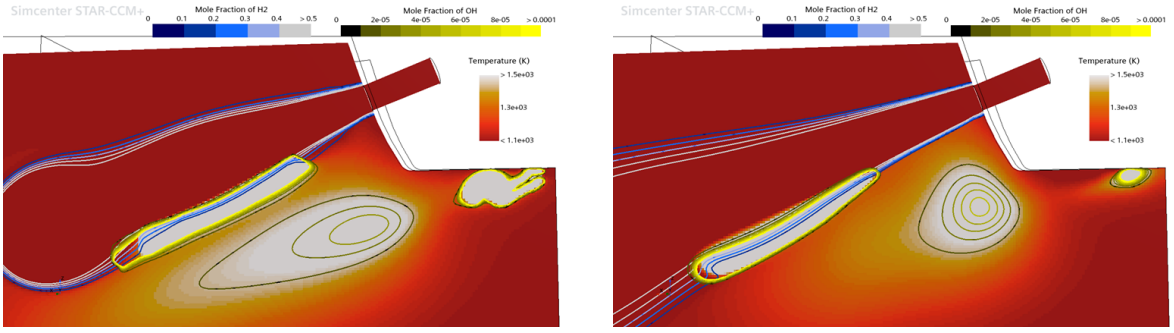

(a) Original Case 1 (A75). **(b)** Half diesel case.

Figure A.9: Contours of H2 and OH concentrations over a 2D Temperature plot - 0.2 CAD after ignition.

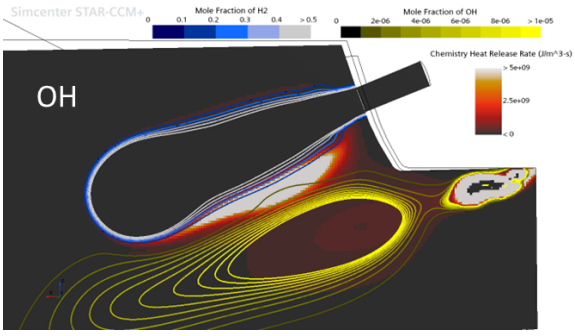

(a) Original Case 1 (A75).

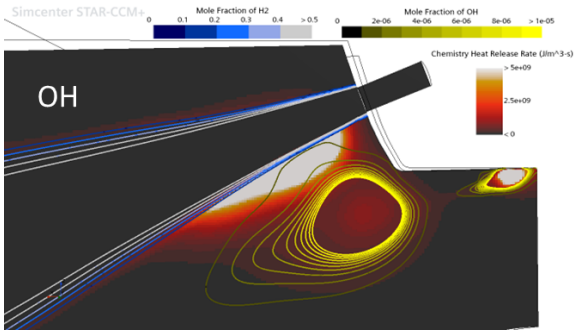

(b) Half diesel case.

Figure A.10: Contours of H2 and OH concentrations over a 2D chemical heat release plot - 0.2 CAD before ignition.

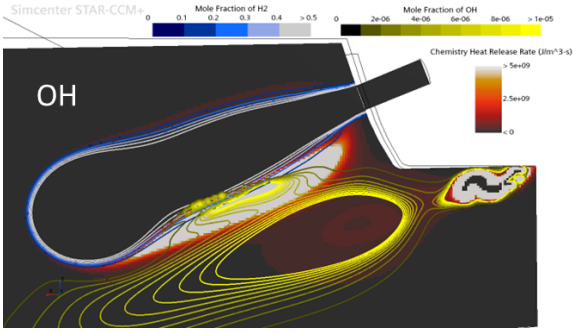

(a) Original Case 1 (A75).

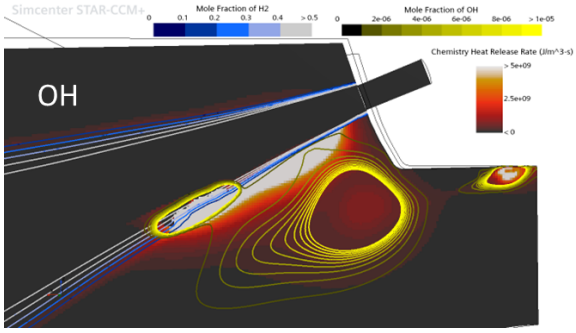

(b) Half diesel case.

Figure A.11: Contours of H2 and OH concentrations over a 2D chemical heat release plot - start of ignition.

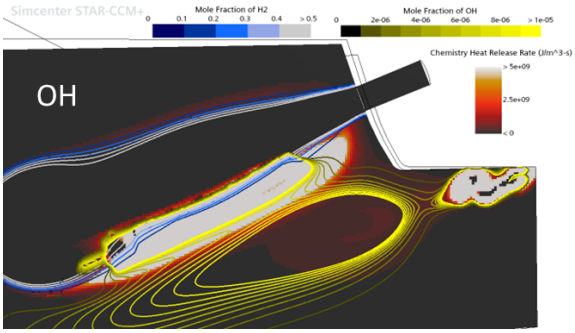

(a) Original Case 1 (A75).

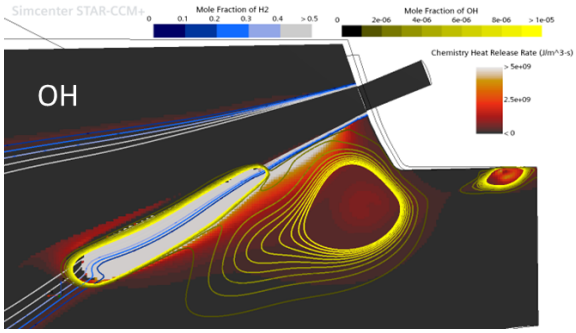

(b) Half diesel case.

Figure A.12: Contours of H2 and OH concentrations over a 2D chemical heat release plot - 0.2 CAD after ignition.

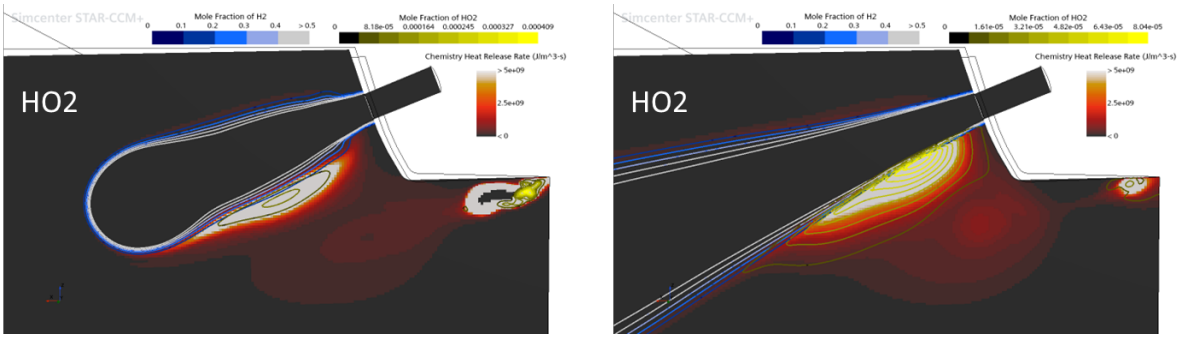

(a) Original Case 1 (A75). **(b)** Half diesel case.

Figure A.13: Contours of H2 and HO2 concentrations over a 2D chemical heat release plot - 0.2 CAD before ignition.

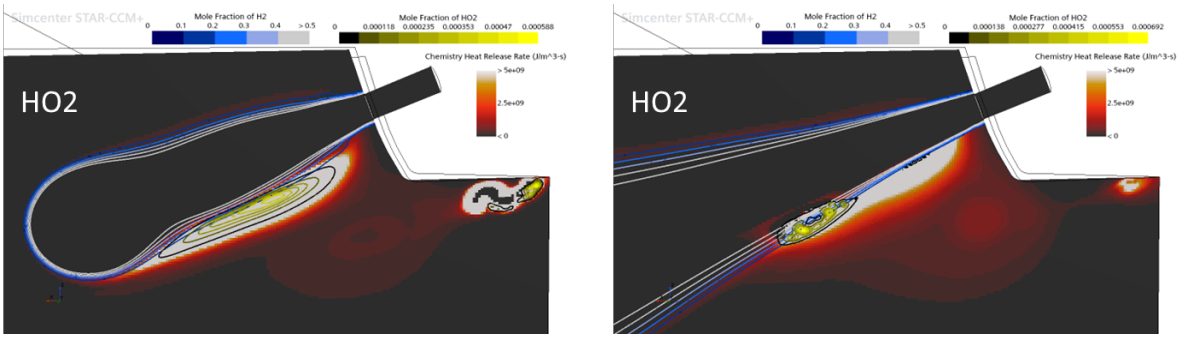

(a) Original Case 1 (A75). **(b)** Half diesel case.

Figure A.14: Contours of H2 and HO2 concentrations over a 2D chemical heat release plot - start ignition.

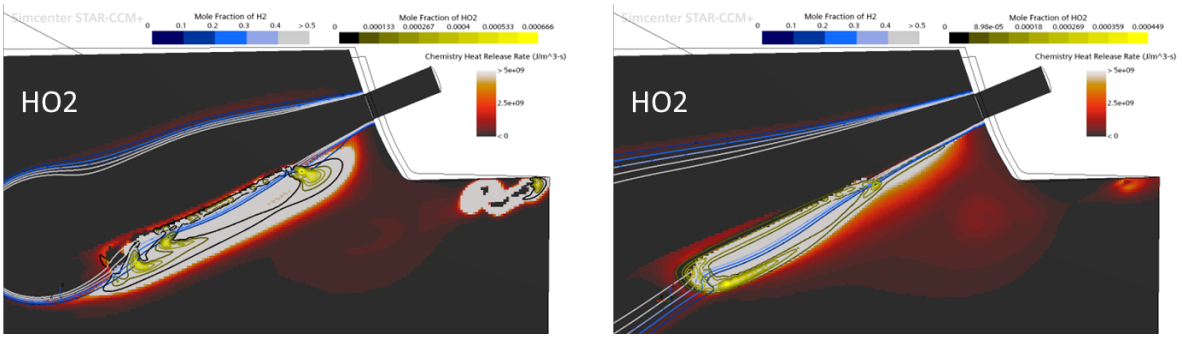

(a) Original Case 1 (A75). **(b)** Half diesel case.

Figure A.15: Contours of H2 and HO2 concentrations over a 2D chemical heat release plot - 0.2 CAD after ignition.

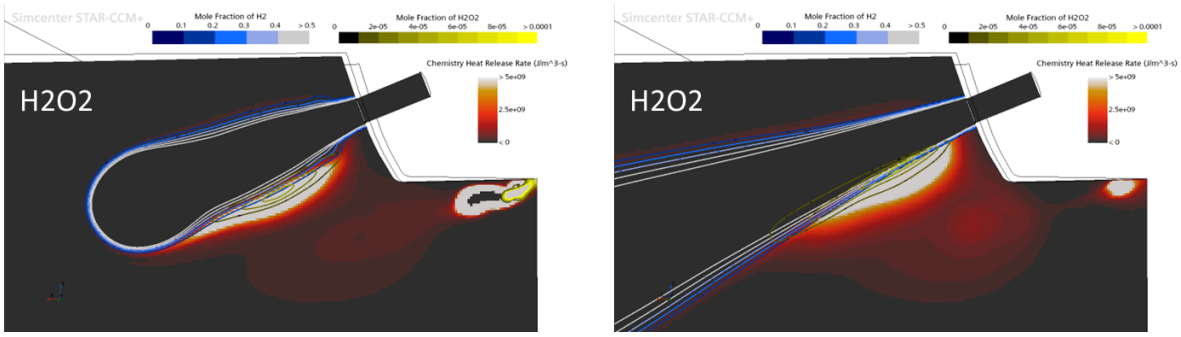

(a) Original Case 1 (A75). **(b)** Half diesel case.

Figure A.16: Contours of H2 and H2O2 concentrations over a 2D chemical heat release plot - 0.2 CAD before ignition.

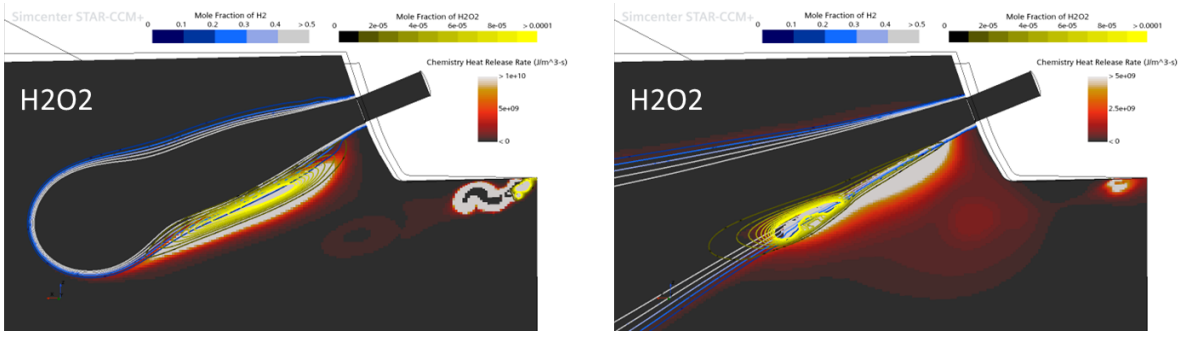

(a) Original Case 1 (A75). **(b)** Half diesel case.

Figure A.17: Contours of H2 and H2O2 concentrations over a 2D chemical heat release plot - start ignition.

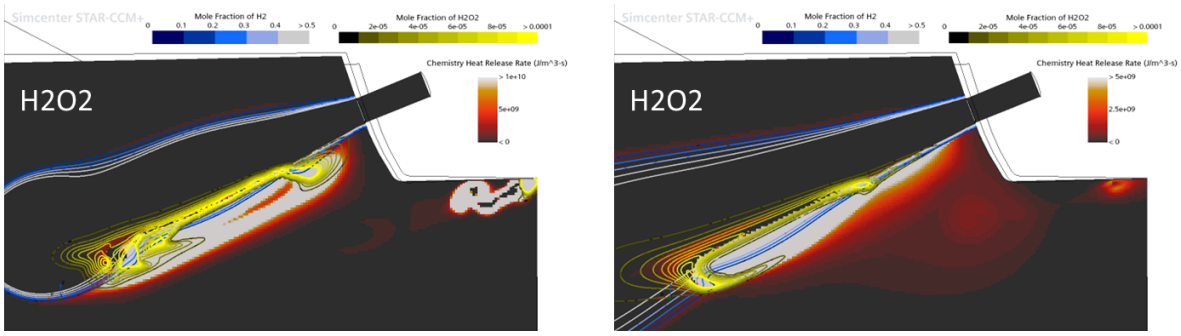

(a) Original Case 1 (A75). **(b)** Half diesel case.

Figure A.18: Contours of H2 and H2O2 concentrations over a 2D chemical heat release plot - 0.2 CAD after ignition.